CALIBRATION OF THE FLUORESCENCE OF ATOMIC NUCLEAR REACTION PRODUCTS EMBEDDED IN NOBLE GAS MEDIUM

By

Erin Elizabeth White

A DISSERTATION

Submitted to
Michigan State University
in partial fulfillment of the requirements
for the degree of

Physics — Doctor of Philosophy

2025

ABSTRACT

Background: Different nuclear processes have occurred for billions of years, resulting in the current map of the universe—its stars, planets, Earth, humans, iPhones, everything that makes up these celestial bodies. Two of these processes are the p-process, which encompasses various photodisintegration reactions, and the s-process, or slow neutron-capture process. Studying the reactions that are branching points or rate-determining steps uncovers information about the origin of the elements composing the cosmos, but to do so requires more sensitive methods of measurement.

Purpose: The Single Atom Microscope (SAM) project aims to measure rare, low-yield nuclear reactions relevant to nuclear astrophysics. Currently, there are two main reactions of interest. Studying ^{84}Kr(p, γ)^{85}Rb will yield insight about a key branching point which determines the reaction flow in the p-process affecting the creation of the p-nucleus Kr-78. This pilot study will help bridge the gap towards measuring ^{22}Ne(α, n)^{25}Mg in the future, which is a key source of neutrons in the s-process.

Methods: This novel detector technique involves capturing product atoms in a cryogenically frozen and optically transparent noble gas solid, and then counting the embedded atoms via laser-induced fluorescence and optical imaging. Due to the unique absorption and emission wavelengths of the product atoms—a shift between which results from the lattice of noble gas atoms—the emitted photons can be differentiated enabling the use of optical filters to select the wavelength range of interest and making single-atom sensitivity feasible. Rubidium atoms embedded in solid Krypton are being used for pilot measurements because they are readily laser accessible and are expected to have a high quantum efficiency which would yield a bright fluorescence signal.

Results: Calibration of the brightness of rubidium atoms in solid Krypton is the next step

in preparing the SAM technique for experiment. Measurements discussed revealed that there are numerous factors to enable fluorescence detection of the atoms in medium, including but perhaps not limited to film thickness, film deposition temperature, and film growth rate. Atomic distribution from the oven nozzle and subsequently across the film, spatial laser intensity over the film, and the solid angle factor for detection of in-medium fluorescence were investigated thoroughly. Additionally, the effect of laser power blasting, time, and post-growth temperature on the in-medium fluorescence measurements were briefly analyzed. The fluorescence cross section for Rb atoms within a thin Kr film was measured via two methods. The more reliable (LPS) method, which subtracted background counts from the data, gave a result of 1.68E-16 cm^2/atom provided the employed experimental and geometric parameters. There is a another result found with an alternate method that is in tension with the primary measurement. However, that result of 3.79E-15 cm^2/atom is within 3.77 standard deviations and the difference can reasonably be explained by unsubtracted background.

Conclusion: The prospects of single atom detection of neutral Rb in solid Kr are still very optimistic. After completing more calibration studies and analyzing more precisely what percentage of product atoms will neutralize by the time they stop within a noble gas film solid trap, the next step for the Single Atom Microscope project would be to measure a nuclear reaction cross section.

Dedicated to all who choose to overcome the obstacles life puts in their way.

ACKNOWLEDGMENTS

I will write my acknowledgments after submitting my thesis to the committee.

TABLE OF CONTENTS

LIST OF TABLES

LIST OF FIGURES

Chapter 1. Introduction

The SAM project sets out to develop a novel detector for the purpose of measuring rare, low-yield nuclear reactions. The general concept of the technique is a two-step process. First, all reaction products including the recoiling product atoms and the unreacted beam atoms are captured. This is done by collecting them in a cryogenically-frozen noble gas film. A film is a thin layer of ice, but in this case the ice is made from noble gases like Kr, Ne, Ar, or Xe. In Figure 1.1, the capture of product atoms from a reaction is illustrated by the left side of the cartoon depiction. Next, the embedded product atoms undergo laser-induced fluorescence which is detected by a Charged Couple Device (CCD) camera. Note that in the right side of Figure 1.1 which portrays the second step, the geometry of the laser is not accurate to the experiment. The geometry used was instead at an angle to ensure that any reflected rays would not saturating the CCD camera. With the carefully calibrated measurement of the brightness of these product atoms in medium, explained in Chapter 4, the number of atoms in the film can be "counted". This number is the information needed to measure the cross section of the reaction.

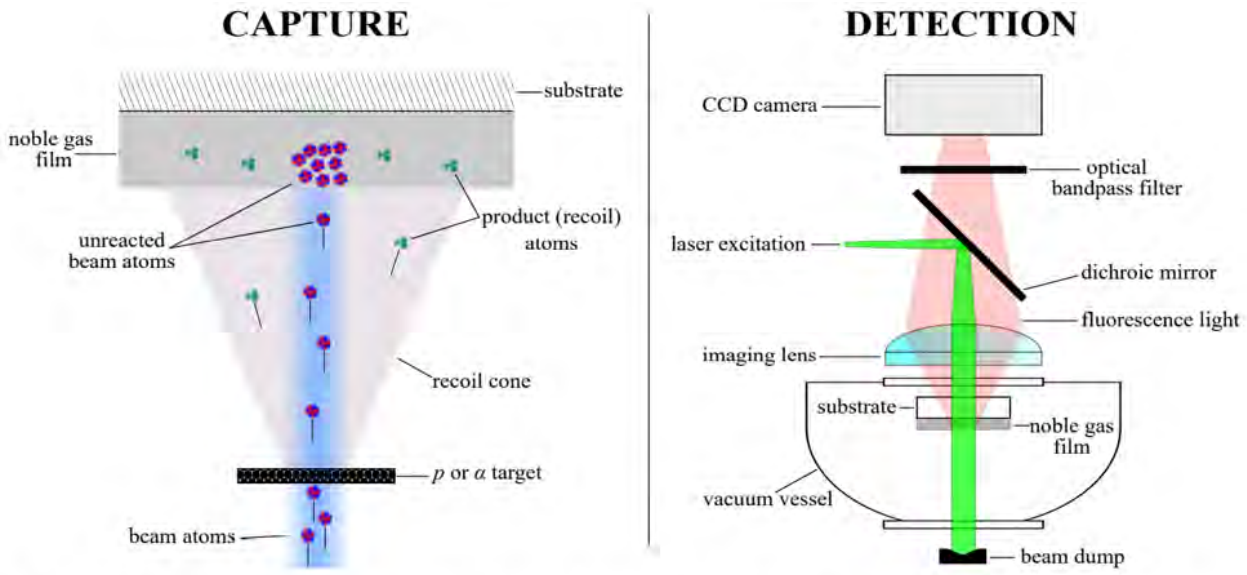

B. Loseth *et al.* Physical Review C 99, 065805 (2019). (arXiv:1903.01278)

Figure 1.1: A cartoon depiction of capturing all product and unreacted beam atoms in a noble gas film (left) and the subsequent detection method of measuring laser-induced fluorescence via a CCD camera in order to "count" the number of product atoms embedded in a film. Note that the true laser geometry is different so as to limit the amount of laser light that could be perceived by the CCD. This figure is reproduced from Loseth PRC [LFF+19].

While the concept of this detection method offers several advantages when executed, there are some limitations. The SAM technique requires laser-friendly atoms that have quick and efficient excitation-emission cycles, as well as stable or long (τ ¿ 1 day) lifetimes. Additionally, the product atoms must be uncommon and different from the beam used to induce the reaction. Finally, there is no isotope selectivity without a recoil separator. Fortunately, this last limitation can be accounted for—and will be—in the future by placing pSAM after a recoil separator instead of solely the end of a beamline. Still, this method provides an alternative to dealing with background neutrons, making it a promising, complementary technique to cross section measurements.

The formation of the universe is a complicated puzzle; tools to help put the pieces together include nuclear physics and astrophysics. Through these disciplines, insight can be

gained about the origin of the elements that make up the world, everything from what is in the atmosphere to the Earth to humans to our iPhones. Studying nuclear reactions—the results of different atomic nuclei colliding and interacting to create new nuclei—enables the uncovering of the picture of our world's creation. One of the key pieces of information needed is the cross section, or the probability that a reaction will occur. Think about searching for directions on Google maps. To get from point A to point B, there are several possible routes and the most common are suggested. The most popular route to the destination is like the most probable reaction to create the element of interest. Determining which route is most probable, and how probable it is, reveals information about the destination, an isotope of an element, and it gives us indications about which routes might be most popular to similar destinations. In Chapter 2, the nuclear astrophysical motivation of this project and specifically a few reactions of interest will be explored. Information about what is being studied by the Single Atom Microscope project and why it is challenging but important is divulged, as well as an overview of how the work plans to be done.

The following chapter, Chapter 3, summarizes previous development of the project and explains the reasons for design choices. Achieving a sensitive measurement of reaction cross sections requires three physical capabilities: the ability to grow optically-transparent and thin noble gas films, beamline access for embedding atoms in said film, and optical access to the film for CCD imaging. The prototype Single Atom Microscope (pSAM), which has been built and tested, accommodates for these necessities. The requirements of these noble gas traps are explained and conclusions about the ideal growth parameters are discussed. This chapter also lists the major equipment that was used to grow films and what was learned from the ReA3 experiment in 2019 which investigated how the films would react to incident beams.

New progress is encapsulated in Chapter 4. Information about fluorescence cross sections, the measurement technique and experimental parameters for calibration studies, and the collected data is included. The data collected includes annealing studies, atomic beamline fluorescence studies in vacuum, in-medium fluorescence studies, laser power scans, equipment testing, and background minimization studies. Additionally, this chapter investigates many major factors that affect the fluorescence cross section, from the start of the atoms' exit from the oven nozzle, to their implantation into noble gas films, and finally to the measurement of the embedded atoms' fluorescence by the charged-couple device camera. Simulation code was developed to model the atomic distribution of atoms out of the oven nozzle and thus throughout the film, determine the solid angle factor of measuring fluorescence from atoms implanted in noble gas films, and the spatial laser intensity over a film so that the fluorescence cross section could be calculated. Furthermore, this chapter reports the analysis of this data and a new number for the measurement of the fluorescence cross section for rubidium atoms implanted in a solid krypton film and conclusions about the results.

Finally, the last chapter, Chapter 5, details personal contributions to the Single Atom Microscope project, the impact of the fluorescence cross section measurement, and the future work that remains before an experimental nuclear reaction cross section measurement can be made. Calibration studies will need to be explored further to map out how the fluorescence cross section changes with film growth deposition temperature and oven temperature. Also, a calibration study should be done with very few atoms embedded to conclude if the current setup is capable of achieving single atom sensitivity like is theorized. When the calibration is mapped out for the atomic species of interest and the sensitivity required is reached, then the next step would be to determine more precisely what percentage of atoms will neutralize within the noble gas film solid trap. With that information obtained, the Single Atom

Microscope project should be ready to take a nuclear reaction cross section measurement. 1

Chapter 2. Motivation & Background

2.1 Motivation

2.1.1 A Big World Begs Big Questions

A great mystery of the universe is how stardust came to compose everything and everyone. What is the origin of the elements that make up everything? Studying the life cycles of stars of varied masses and the abundances of elements in their photospheres provides information about which elements are produced and which nuclear reactions may be taking place. Three methodologies must converge for each piece of the puzzle to be put into place: nuclear physics experiment, astrophysical theory, and astronomical observation. Theory can produce complex models that help explain the parameters needed for the production of different elements. Observation provides the stellar abundances of elements around the universe. Experiment measures nuclear reactions to give context about the limits of production of different elements based on the environment. Theory shows experiment what reactions need to be measured, experiment provides data for theory to improve simulation and for observation to know what needs to be observed, and observation provides theory data to improve accuracy in simulations. When all three are in agreement for all isotopes of the elements, the answer of the origin of the elements will be revealed.

The chart of nuclides provides the picture on the box for the puzzle of the origin of the elements. To get from one isotope to another, different reactions take place. Experiment has helped find some of the edges of the puzzle by finding limits to the number of protons and neutrons an atom can have. Given an idea of how many puzzle pieces—isotopes—exist, the next step is to figure out which reactions made which isotopes.

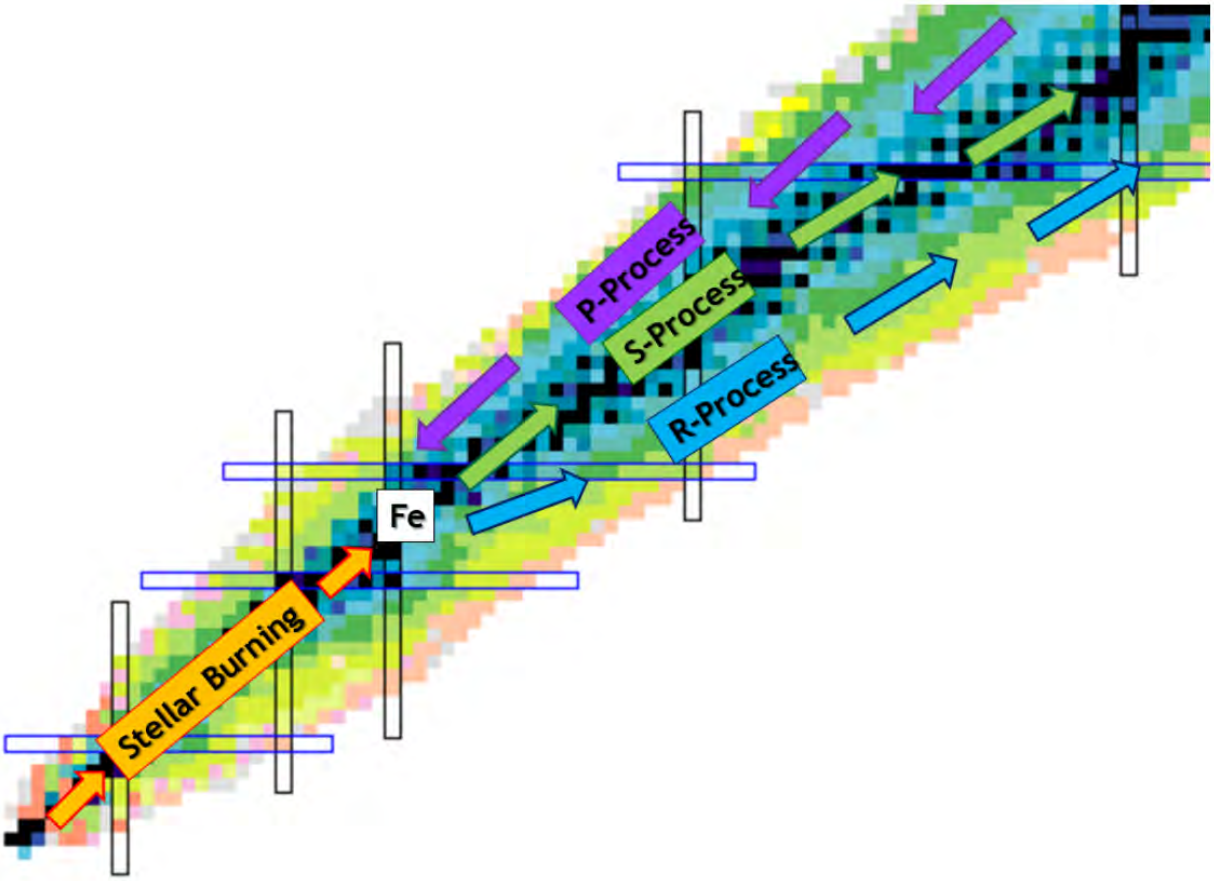

Figure 2.1: The chart of nuclides shows the region of isotopes that each process can access. As you move up the chart, the proton number of the isotopes increases, as you move right, the neutron number of the isotopes increases. Horizontal lines have the same number of protons, vertical lines have the same number of neutrons. Further, the darker the color the of the square, the more stable the isotope is. This figure is reproduced from [Pal20].

Myriad nuclear processes have occurred for billions of years, resulting in the current map of stars, planets, and everything that makes up these celestial bodies. Nucleosynthesis is the umbrella term for these processes of creating new nuclei from existing nuclei and nucleons—protons and neutrons. Figure 2.1 shows the general regions on the chart of nuclides that are created by different nuclear processes. Two of them are the p-process, a series of photodisintegration reactions, and the s-process, or slow neutron-capture process. Each process can access different isotopes on the chart of nuclides, but none can access all of them. Instead, each accesses a given region of the chart, making study of all possible processes paramount. Some reactions are key to understanding the path a process takes along the chart. For example, there are branching points in the chart where there are more than one type of reaction likely to take place. It is important to understand the probability for each reaction to occur so the path along the chart of nuclides can be found and to determine how much of an element that reaction is likely to produce in an astrophysical setting. For the Single Atom Microscope (SAM) project, one of these branching points of interest is that at Kr-84, which studying ^{84}Kr(p, γ)^{85}Rb will shed light on. Another type of key reaction to study is a rate-determining step. These reactions provide crucial particles for other reactions to have the possibility of occurring. In particular, one interest is ^{22}Ne(α, n)^{25}Mg which is a key source of neutrons for the s-process. Studying reactions such as these uncovers information about the origin of the elements, but to do so requires more sensitive methods of measurements.

Stars are created from a cloud of dust condensing into a ball. That "dust" is made up of hydrogen and an equilibrium is created between the energy released from the hydrogen nuclei fusing together and the gravitational pull of the star. The continuous fusing of hydrogen nuclei to form helium will eventually leave it with helium at the core, making the form of

the star a helium center with a hydrogen shell. Mass dictates the possible evolution of a star, though all stars will spend most of their lifetime in the aforementioned stage known as main sequence burning. The reactions of interest are processes that occur in intermediate mass stars, 0.5-8 solar masses ($M_{\odot}$), which follow a path to become asymptotic-giant branch (AGB) stars and massive stars, above $11M_{\odot}$, in which stars are able to achieve the silicon burning stage to produce iron [Pal20].

After initial creation, a massive star will continue hydrogen burning to form helium at its core in the main sequence stage until the core is purely inert helium. Hydrogen in the outer shell continues to burn, adding more mass to the helium core. Without fusion releasing energy at the core, the equilibrium is unbalanced and the gravitational pull begins to shrink the helium core until the temperature and pressure rise to the point that helium fusion can begin. With a large burst of energy, the core expands and the hydrogen layer is heated as the star becomes a super-giant. Again the core is replaced with the newly synthesized element, carbon, until the helium is left only in a layer beneath the hydrogen shell. These steps of the shrinking core and new elemental burning repeat with carbon, neon, oxygen, and silicon until there is an iron core [Pal20]. See Figure 2.2 for illustration of the layered structure created. This is the limit of the cycle of burning for these massive stars because there is no longer enough energy to balance with the star's gravitational pull. In fact, iron burning would not be favorable because it would not release energy since it is an endothermic reaction, not an exothermic one [Pal20].

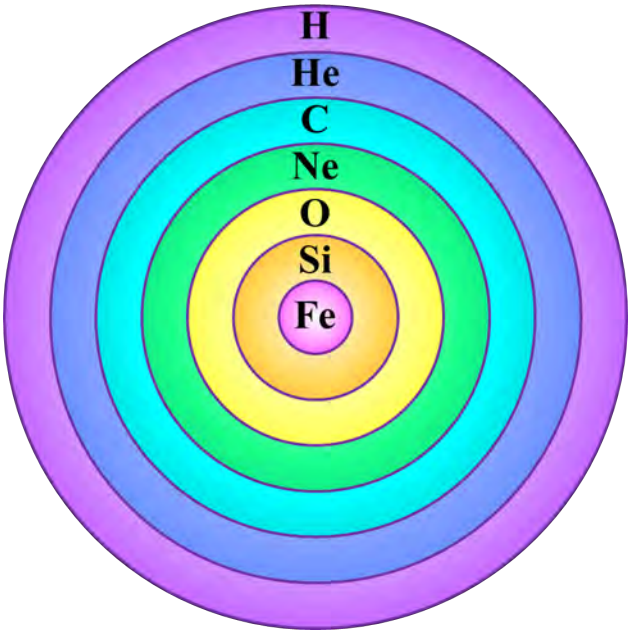

Figure 2.2: The layers of a massive star: layers are not to scale, but the order of the elements in each shell are shown.

From here, the iron core would expand until the inevitable core collapse due to an overpowering gravitational pull. This supernova could leave behind a black hole or a neutron star. With such a powerful collapse, a shock wave reverses through the star passing through each layer it contained prior. When traversing the oxygen/neon (O/Ne) layer, the shock wave presents the right conditions for the p process to take place. There are 35 proton-rich nuclei—known as p nuclei—that are inaccessible by neutron-capture processes, and instead synthesized via the p-process [BBFH57, RDD$^+$13].

AGB stars are too low in mass to fuse carbon, leading them to a different ending, post-AGB. Their core shrinks again and matter is expelled from these types of stars, contributing the majority of the dust in the universe. This expulsion of material forms a planetary nebula and the remainder of the core cools to become a white dwarf. Planetary nebula are considered an end stage, but white dwarves may accrete material from companion stars until they can no longer sustain balance with their gravity and explode in a type Ia supernova. It is in the

AGB stage, helium and carbon burning phases, that there are enough free neutrons for the s-process to occur [Pal20]. Neutron-capture reactions, either in the s-process or the r-process, are responsible for the nucleosynthesis of most elements heavier than iron [BBFH57].

With the p-process and s-process in mind, the Single Atom Microscope (SAM) projects aims to offer an alternative method for measuring pertinent nuclear reactions without the hindrance of high background rates. Measuring a nuclear reaction translates to determining the cross section of the reaction.

2.1.2 Nuclear Reaction Cross Section

A reaction cross section gives information about the probability that a reaction will occur. Cross sections can be explained conceptually by this equation [Ili15]:

$$\sigma = \frac{\text{(number of interactions per time)}}{\text{(number of incident particles per area per time)(number of target nuclei within the beam)}} \tag{2.1}$$

Essentially, a cross section is a quantitative measure of how often the reaction occurs given the environmental parameters where it is being measured. Another way to think about this is in terms of rates. A cross section is the rate at which interactions occur given the flux of incident particles and density of target nuclei. When the beam and target particles interact, there may be a reaction or elastic or inelastic scattering. A reaction cross section refers to all processes aside from elastic scattering, so for a reaction cross section, the number or rate of interactions would be replaced with the number or rate of product particles. In terms of units, a cross section is an area. Reaction cross sections are typically given in units of barns of some order.

In many cases, as discussed in the previous subsection, there are multiple possible reactions that can occur when two particles interact. Each possibility is a separate channel. When investigating ^{22}Ne(α, n)^{25}Mg for example, a competing reaction is ^{22}Ne(α, γ)^{26}Mg [JKM^{+}01]. Measuring the reaction cross section of ^{22}Ne(α, n)^{25}Mg then, is not the total reaction cross section, but rather the reaction cross section for one channel, one possible outcome. Thinking about this in terms of probabilities, it follows that the total cross section is the probability that any interaction between particles will occur; the total reaction cross section is the sum of all reaction cross sections for each possible reaction. In the case of ^{22}Ne(α, n)^{25}Mg and ^{22}Ne(α, γ)^{26}Mg, if these were the only two possible channels, then the sum of their reaction cross sections would be the total reaction cross section. As it stands, measuring the cross sections for both of these reactions will reveal information about ^{22}Ne(α, n)^{25}Mg as a neutron source for the s-process, since ^{22}Ne(α, γ)^{26}Mg affects the abundance of Ne-22 in the stellar environment [WdG23].

In the SAM project, the number of incident particles per area per time will be well known beam parameters and the number of target nuclei within the beam will also be known. This leaves only the number of products particles produced per time to be determined in order to calculate the reaction cross section.

2.1.3 Reasons a Reaction May Be Low-Yield

There are multiple reasons that a reaction might be considered low-yield as there are several factors that play a role in a reaction occurring. Most simply, a reaction may be low-yield because it has a small cross section. Even with the best conditions, the reaction might be dominated by a competing one or the nature of the particles might not lend itself to the reaction taking place. Specifically, the Coulomb barrier can be difficult to overcome at as-

trophysically relevant energies (within the Gamow window). When reaction rates are slow or inefficient, whether due to the Coulomb barrier or to reaction channels being blocked by unstable nuclei, cross sections will be small. Additionally, experimental limitations might be the cause for a reaction to be low-yield. Rare isotope beams may have too low of an intensity for sensitive measurements to be possible given traditional detection methods [Los20]. Further, reactions that are measured with high background rates can lead to very small signal to background ratios and thus be low-yield.

2.1.4 Challenges of Measuring a Low-Yield Reaction

Low-yield reactions are especially challenging to measure due to the nature of the reactions and the experimental requirements to produce them. Traditional methods often employ inverse kinematics, where the smaller mass particles make up the target nuclei and the larger mass ones the beam nuclei. This results in a narrow cone of scattered product nuclei which can be separated from the beam with a recoil separator. However, most traditional methods focus on detecting the small products—the protons, neutrons, or gamma rays. These techniques are thus susceptible to the high background rates from cosmic rays, natural background sources, and beam-induced background counts, which as aforementioned, can significantly outweigh the reaction rate. When the cross section of a reaction is already small, a large background rate can decimate the signal to background ratio. Some experiments have been and are being performed in underground laboratories to avoid this obstacle, where the background rates can be reduced by multiple orders of magnitude such as in the case of CASPAR at Sanford Underground Research Facility [WdG23].

Experimentally, a small cross section can translate to high beam currents and dense targets still only producing a handful of reactions per day. This means that a low-uncertainty

measurement requires unity or near unity sensitivity. Even with lower background rates, the detection scheme will need to be efficient as missing the collection of even one particle can greatly affect the measurement.

Additionally, some reactions are made more difficult to measure due to beam limitations. Some rare isotope beams are contaminated with other nuclei because of how they are produced, which creates the beam-induced background referenced above. Further, not all rare isotope beams have sufficient beam intensities needed for the reactions to occur. And finally, selectivity is limited. Heavy nuclei may have very similar charge-to-mass ratios hindering the ability to separate products from the beam even with recoil separators since intense magnetic fields would be required along with a great distance.

Due to these challenges, the SAM project as an alternative technique plans to offer high efficiency, selectivity, and sensitivity without the complications posed by elevated backgrounds since it will measure the large product atoms from astrophysically relevant reactions through optical imaging. With this detection method, the SAM technique will be apt for studying reactions with extremely small cross sections that can result from a high-current stable isotope beam and reactions that require a low-current rare isotope—radioactive—beam.

2.2 Reactions of Interest

2.2.1 Reaction With a Small Cross Section

Slow neutron capture, or the s-process, gives access to heavy elements. For a nucleus to capture a neutron, free neutrons must be available and they must come from somewhere. One key source of production of free neutrons is from ^{22}Ne(α, n)^{25}Mg. Knowing the production

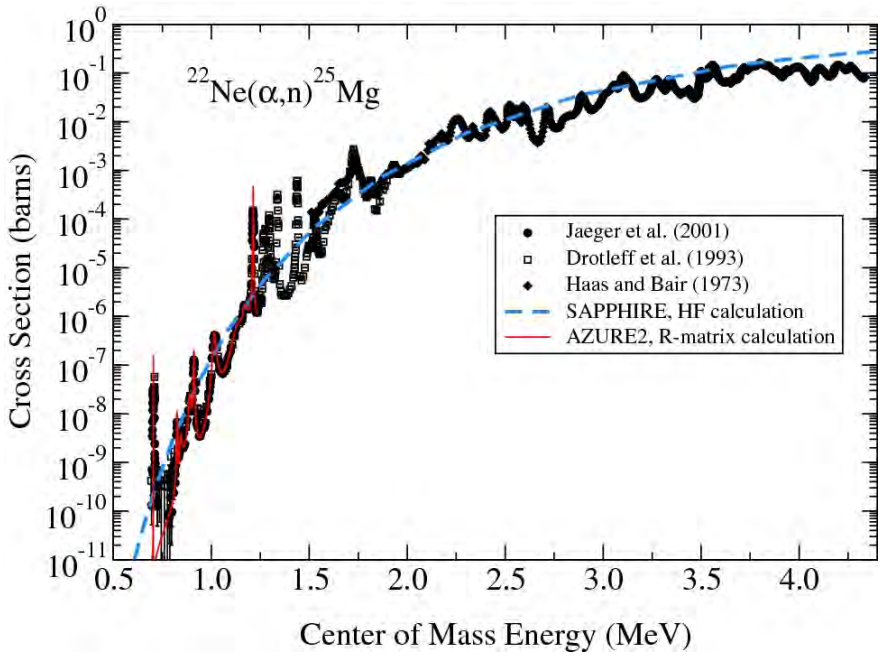

Figure 2.3: This figure is reproduced from [WdG23] and shows the experimental cross sections by Jaeger el al. [JKM$^+$01], Drotleff et al. [DDH$^+$91], and Haas et al. [HB73]. The solid red line indicates the results of an R-matrix calculation of the cross section over the data region from [JKM$^+$01]. The dashed blue line illustrates the HF calculation done over the entire energy range, which actually extends to 18 MeV center of mass energy.

rate of neutrons helps determine how fast elements are produced by the s-process. In other words, ^{22}Ne(α, n)^{25}Mg is a rate-determining step for the s-process to occur. This reaction is predicted to have a cross section within the Gamow window on the order of 10^{11} barns, which is more manageable than the previous estimated low of possibly 10^{-15} barns [WdG23, JKM$^+$01]. Figure 2.3 from [WdG23] shows the predicted cross section of ^{22}Ne(α, n)^{25}Mg over a wide energy range. The astrophysically relevant range is 0.5–1.0 MeV.

The SAM technique will be described in the next section, but overall it offers an alternative method of detection for measuring nuclear reactions. Rather than measuring the small products, it optically detects the large product atoms produced in the nuclear reactions of interest by trapping them in a solid noble gas film. The reaction ^{22}Ne(α, n)^{25}Mg is a great candidate for the SAM technique for multiple reasons.

Previously, only one atom per day was expected to be produced for this reaction [Los20, WKL12]. With a larger cross section now predicted [WdG23], the production rate should be higher and the SAM technique becomes even more feasible as multiple atom detection may be enough to get a higher quality measurement compared to the required single atom detection thought to be needed before. That said, single atom detection seems feasible for the SAM project, which will be useful since the cross section of this reaction within the Gamow window is still small and is projected to span four orders of magnitude within this energy range. Also, while this may still be a relatively low yield experiment, the Facility for Rare Isotope Beams (FRIB) is able to create high intensity radioactive beams at a higher production rate than before.

What should be noted as well, is that previously in Dr. Ben Loseth's thesis, the high beam currents required the unreacted beam intensity (10^{15} pps) be attenuated by some factor of a million to avoid significant damage to the noble gas film solid trap for the product atoms [Los20]. Now, while attenuation may still be recommended, film damage should be less of a concern as the experiment should be able to be run with less beam exposure than previously needed. Attenuating the beam intensity can be done with a recoil separator, which, as will be shown, contributes to making this reaction a great candidate for the SAM technique. Since Ne-22 is a noble gas, the unreacted beam particles caught in the Ne-22 solid trap would not contribute to background fluorescence during the optical imaging of the product Mg-25 atoms. Additionally, due to its design, the SAM method is unsusceptible to beam contaminants that may be challenging to completely remove from high-intensity beamlines.

Finally, this technique will be complementary to traditional methods, offering a unique and alternative angle for measuring reactions. Since this technique is unique from traditional methods, it offers the possibility of increasing certainty in existing measurements.

2.2.2 Reaction With a Low Beam Intensity

In addition to reactions with small cross sections, the SAM technique can be useful for measuring reactions that would utilize low beam intensities. In traditional methods, low beam intensities can limit the sensitivity of measurements, but the SAM technique plans to offer single atom sensitivity and high selectivity between atomic species, making it a promising method for improving on cross section measurements in this category.

The p-process involves photodisintegration reactions—(γ, n), (γ, p), and (γ, α) [Pal20]. This process is helping to explain the disparity between the overabundance of molybdenum and rubidium in observation compared to theory. Through this process, p nuclei—proton-rich isotopes that are inaccessible through neutron capture processes—can be created. An example reaction is ^{91}Nb(p, γ)^{92}Mo, which is a key reaction in the production of p nucleus Mo-92 [RNH^{+}16]. The cross section of this reaction is predicted to be between 1 mub–1 mb within the Gamow window [Rau]. A benefit of low beam current for the SAM technique is that there are no extra precautions required for ensuring the maintenance of a film's integrity. Therefore, the capture efficiency should be near unity.

In contrast, measurements relying on the detection of gamma rays have lower efficiencies and have to battle against high backgrounds from cosmic rays or environmental sources. This means they require more beam time to achieve reasonable signal to background ratios for their measurements. There are similar challenges for low-energy neutron detection too. And because the nuclides involved in this reaction are heavier, the higher mass means limitations on the efficiency of recoil separator systems without selecting a high charge state. Therefore, the SAM technique could potentially significantly outperform these methods.

2.2.3 Pilot Reaction

With the arduous nature of measuring ^{22}Ne(α, n)^{25}Mg, the still-difficult-yet-more-approachable ^{84}Kr(p, γ)^{85}Rb provides the opportunity for a proof of principle experiment, making it the first planned measurement for the SAM project. With Kr-84 as the beam particles, the unreacted beam that is captured within the Kr noble gas solid trap will be optically invisible. The strong transition of product Rb-85 atoms is accessible too, making this reaction an ideal choice for pilot measurements.

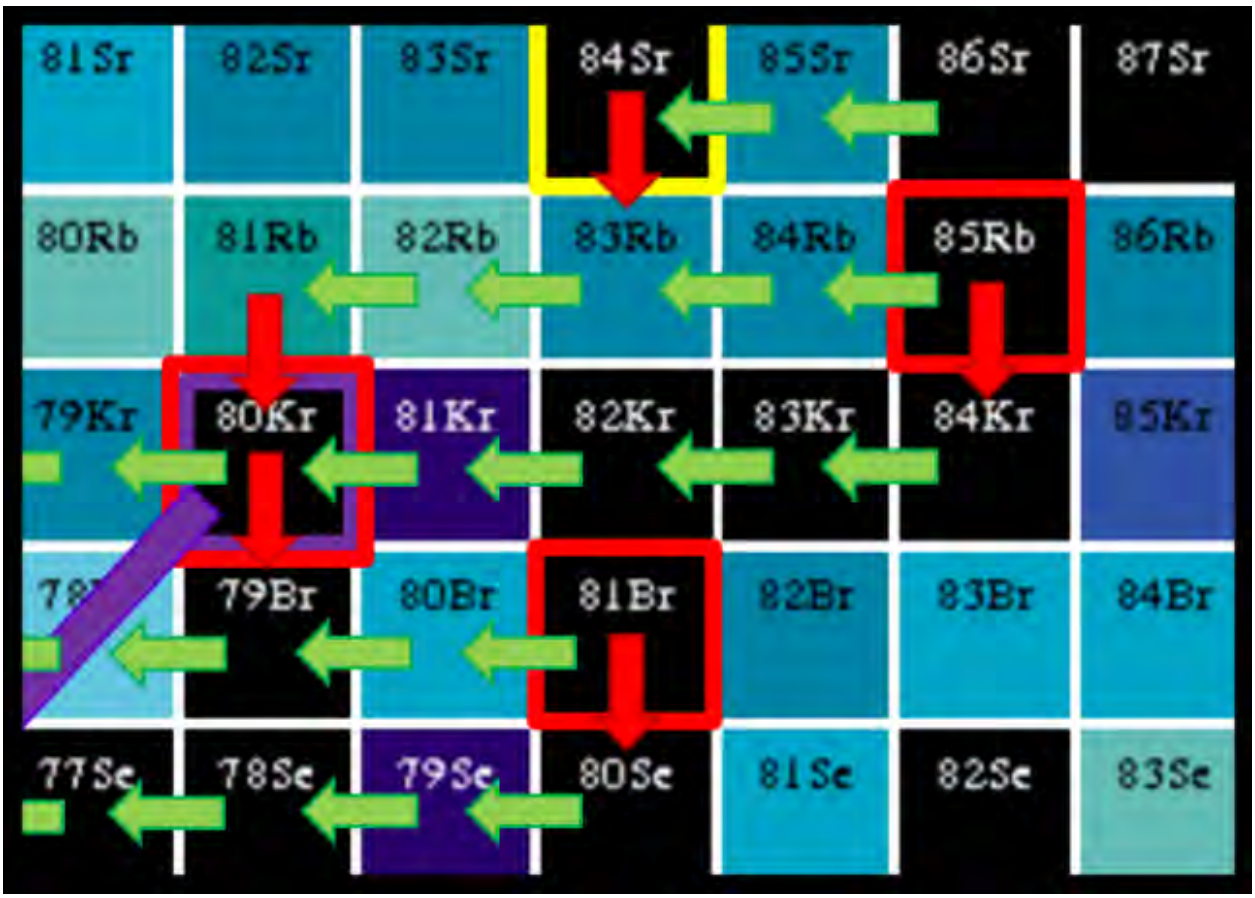

Figure 2.4: A section of the chart of nuclides which shows the reaction network around Kr-84. This figure is reproduced from [Pal20].

This reaction, ^{84}Kr(p, γ)^{85}Rb, is of interest as the reverse reaction is a branching point in the reaction network. The cross section of this reaction provides information about the

production of a p nucleus, Kr-78.

Figure 2.5: The reactions leading to and away from Kr-78, Kr-84, Rb-85. These are reproduced from [RG].

There are currently a couple different measurements for ^{84}Kr(p, γ)^{85}Rb and they are not in agreement. One experiment at FRIB with a cylindrical detector of optically isolated NaI crystals with 4π coverage called SuN reports a cross section of 0.305 mb with an uncertainty of 0.056 mb at an effective energy of 2.367 MeV amongst a few other data points at other energies [PKSD$^+$22]. This measurement is in conflict with the measurement from TRIUMF of 94 μb with an estimated uncertainty of $\pm$16% at an energy of 2.435 MeV [LGW$^+$21]. Using the SAM method, a unique style of measurement would allow for one—or neither—of these measurements to be supported. As the SAM technique utilizes a significantly different approach, any systematic errors that led to the discrepancy between these measurements would likely not be present.

2.3 An Alternative Method

2.3.1 SAM Technique Overview

All around, whether studying reactions for the s-process or the p-process, greater sensitivity is needed and the SAM technique aims to provide some. Given the extreme low-yield of many

reactions of interest, an alternative method will complement traditional ones and ultimately increase the certainty of validity of nuclear reaction measurements.

The Single Atom Microscope (SAM) project sets out to develop a novel detector for the purpose of measuring rare, low-yield nuclear reactions. Due to the Coulomb barrier, some reactions have incredibly small cross sections at astrophysical energies—0.5 to 1 MeV. Because of this, the SAM technique intends to offer a new method with high efficiency, selectivity, and sensitivity.

With the SAM technique, noble gas will be cryogenically-frozen to create solid traps. These traps will be downstream from beamline interactions with target nuclei such that they capture the product atoms of the reaction. These product atoms will then be excited by a laser so the induced fluorescence can be measured as a way to "count" the embedded atoms.

2.3.2 High Efficiency

Since the SAM technique is intended for inverse kinematics configurations, the setup ensures that most if not all product atoms produced can be captured within the noble gas film trap. As higher mass beam particles are incident on small mass target nuclei, the product atoms can only travel in a narrow cone. Strategic placement of the film trap allows for near-unity efficiency. This is ideal since the reactions intended to be studied are rare and low-yield, so maximizing detection is imperative.

2.3.3 High Selectivity

The absorption and emission spectra of nuclei in medium are shifted from when in vacuum. When in vacuum, the absorption of laser light and emission of photons from nuclei are approximately the same. When in medium though, generally the absorption spectra becomes blue-shifted and the emission bands red-shifted. So rather than being the same wavelength, the laser wavelength needed to excite the atoms is lower when in medium and the emitted photons fluoresce at a higher wavelength in medium than when in vacuum. This separation of spectra means that the excitation laser light can be optically filtered from the fluorescence of the product atoms. Since nuclei all have specific transitions, their absorption and emission spectra are unique—like fingerprints—and therefore this method offers high selectivity for exciting and measuring the product atoms that are captured in the noble gas trap. This also means that because the method is able to differentiate between different atomic species, it can overcome beam contamination or separation issues. However, it should be noted that the SAM technique alone is not enough to distinguish between different isotopes of the same species. For that, a recoil separator should be employed.

2.3.4 High Sensitivity

Single atom sensitivity appears to be feasible with SAM, especially as it has been demonstrated with the barium atoms in solid xenon [CWF$^+$19]. With this method of detecting the large product atoms rather than the smaller products, traditional background sources are not a concern. The measurement of the laser-induced fluorescence from the product atoms caught in the noble gas solid is impervious to neutron and γ-ray backgrounds.

With the SAM technique, the ability to detect single atoms relies on a high signal to

background ratio. Minimizing light background from the environment and the laser can be done with a calculated geometrical setup and optical filters. In order to be able to actually "count" the embedded product atoms though, calibrated measurements of their fluorescence is needed. These calibration studies, discussed in Chapter 4, shed light on how bright the atoms are in medium—how many photons per second they emit.

Chapter 3. The Study of Noble Gas Films

3.1 Requirements of the Host Matrix

3.1.1 Why Noble Gas Films

The SAM projects sets out to measure nuclear reactions from a different perspective than most methods—by measuring the "large" product particles instead of the small ones. With this method, high background rates of the "small" particles produced are not a concern. In the case of ^{84}Kr(p, γ)^{85}Rb, that means measuring the number of Rb atoms produced instead of the gamma rays. In order to do this, the SAM method aims to trap the Rb atoms and the selected method is with cryogenically-frozen noble gas matrices. The major reasons for this choice include accessibility, indiscrimination, and nonreactive nature.

First and foremost, simply it is possible to use noble gases. Accessible freezing points enable the use of Neon, Argon, Krypton, and Xenon, though currently the SAM project has not done any testing with Xenon. Growing a film—a thin layer of deposited atoms—with noble gases can therefore be done, and be done well enough that they are transparent. Film clarity impacts the ability for quality spectroscopic experimentation and thus the ability to measure the number of product atoms trapped. Secondly, a solid trap offers non-selectivity for the products it captures since neither the element nor charge-to-mass ratio influence its ability to catch atoms. Noble gases are ideal candidates to employ in the production of these solid traps because their nature prevents them from chemically reacting. Not only does this further which atoms they can capture safely and securely, but it also enables better purification of the gas before deposition. Impurities could cause problems in a couple of ways. They could react with each other or the product atoms and affect the products'

spectra. Or, while unlikely, it is not impossible for impurities to experience excitation and emit their own photons in the same laser scanning range used to induce fluorescence from the product atoms and this would skew the measurement. Despite a low probability of that happening, in experiment only a handful of product atoms are expected, so extra emitted photons from impurities could significantly increase optical backgrounds if there is a high density of impurities throughout the film. Noble gases help avoid that issue.

Some considerations for using noble gas films are if they can handle the heat load from the beam that does not react with the target as it would be incident on the film and if the reacted atoms which are ionized will fully neutralize by the time they stopped in the film. These considerations were examined in previous work on this project and full details of the relevant research and experiment can be found in Dr. Ben Loseth's thesis or a summation can be found in the next chapter. As a preface though, the experiment proved that a Kr film could withstand the Kr beam for a long time without compromising its integrity and at least some portion, possibly all, of the ionized Rb beam used to simulate product atoms neutralized within the film. Lastly, it is unclear which trapping sites product atoms will occupy when they stop within the film, so it is ideal if all trapping sites are accessible.

3.1.2 Film Size Requirements

A good host matrix must be efficient by capturing all of the product atoms. Geometry facilitates efficiency for the noble gas films. When studying ^{22}Ne(α, n)^{25}Mg, a recoil separator will lie between the Helium target and the noble gas film to separate Mg-25 from Mg-26. The area that the recoil separator will deposit Mg-25 atoms is one inch in diameter—the same as that of the films grown in the SAM method [ZZB10]. Before that experiment comes the pilot reaction study of ^{84}Kr(p, γ)^{85}Rb. As this reaction does not require the use of a

recoil separator, there are two options. Either account for the area of the film in comparison to the possible area the product atoms could reach or, preferably, install the proton target close enough to the film such that all recoiling product atoms are captured within it. This should be made easier by the conservation of momentum at play between the fast, heavy ion beam incident in the direction of the light target.

A diameter of one inch accounts for the breadth of recoiling products, but the film's thickness is another important factor. How to grow very thin, 1-10μm, films with excellent clarity is well-known [STS$^+$15], but they are unusable for this experiment as solid traps. Measuring these types of nuclear reactions calls for high energy ions to fly at the film. For them to be embedded in the nonreactive noble gas film, rather than the unpredictable sapphire substrate, the film needs to be thicker than 10μm. With an anticipated ion energy of about 0.1 to 1 MeV/nucleon, the projected stopping distance over that range for either Rb in Kr or Mg in Ne goes up to *almost* 100μm. Therefore, 100μm is a suitable thickness to ensure all ions and atoms from experiment on the beamline will be captured within the film itself.

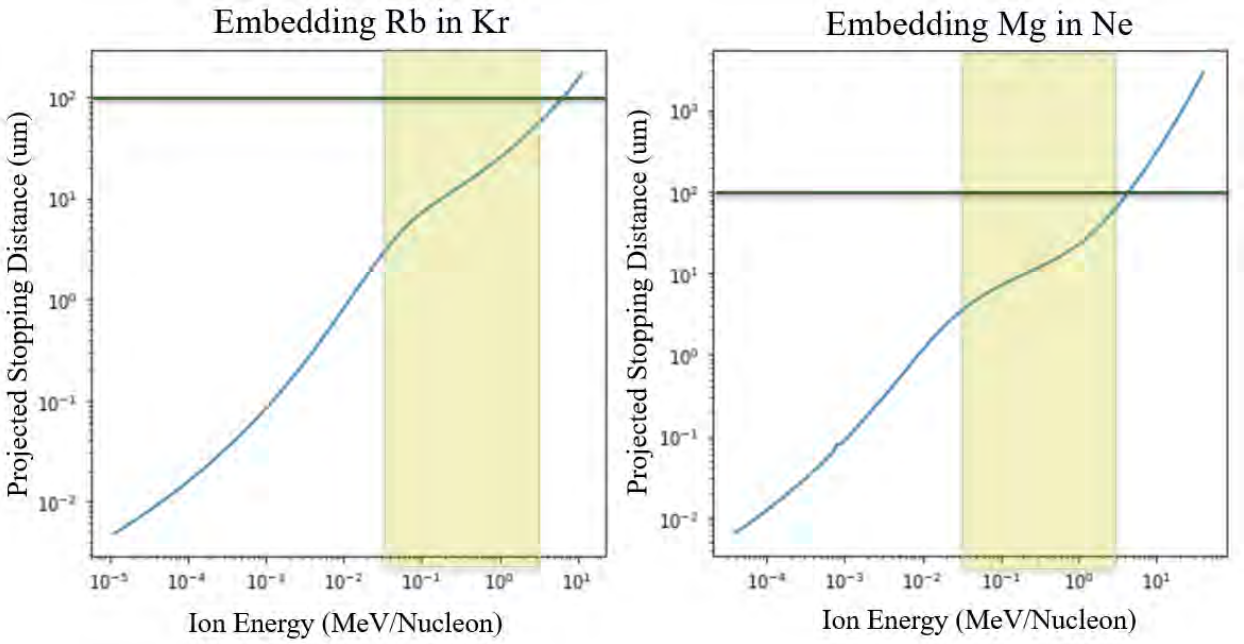

Figure 3.1: A plot of the projected stopping distance of recoiling product atoms in a noble gas film compared to the ion energy of the beam. At left, see the calculation for Rb-85 produced by a Kr-84 beam stopping in a Krypton film; and at right, that for Mg-25 produced by a Ne-22 beam stopping in a Neon film [ZZB10]. The shaded regions show the astrophysically-relevant energy range. This range is the Gamow window and encompasses were most reactions will take place based on the overlap of the Coulomb barrier and Maxwell-Boltzmann distribution [BD04]. The horizontal lines highlight 100μm to show a film with that thickness would capture all product atoms.

3.2 Film Growth Equipment

A more detailed account of all equipment and materials used between the Gas Handling System (GHS) and prototype Single Atom Microscope (pSAM) can be found in Dr. Ben Loseth's thesis [Los20]. In this section, the main components are given with context about how they are used provided.

3.2.1 Equipment Used to Grow a Film

Growing a film involves the use of a Gas Handling System (GHS) and the prototype Single Atom Microscope (pSAM). Together these two systems provide control over the noble gas flow rate, system temperature, and more. The first of these systems, pictured in Figure 3.2, purifies and controls the flow of the noble gas supply. Beginning at the noble gas tank, the GHS utilizes a regulator before optionally flowing the noble gas through a getter purifier to remove impurities. For all film growths done with Kr gas discussed in this thesis, the bypass system was used, so the getter purifier was more or less irrelevant. Then, the gas flow path continues to a control valve that adjusts during film growth to enable the ideal flow rate for optimizing film quality. A PID (proportional-integral-derivative) controller aids in the control valve's adjustments based on the readings from the pressure gauge immediately following the valve. There are actually two pressure gauges just after the valve, a cold cathode sensor (CC) and a Baratron pressure gauge. The CC is able to measure very low pressures and is used to verify the GHS is at a low enough vacuum to be considered "clean" before filling the system with gas again. During a film growth, it is turned off to protect the device. The Baratron pressure gauge is able to measure pressure without re-calibration to account for the type of gas being used. This works because the Baratron is really a parallel-plate capacitor measuring the capacitance and calculating from that value a gas-type-independent pressure. Past here, the gas flows through an elective cold trap station. If employed, the liquid Nitrogen cold trap can offer another round of purification. This was unused for Kr films, but is recommended for Ne films. Finally, the noble gas flows into pSAM through flexible, capillary tubing (1/16 OD, 0.04 ID, approximately 20 in length) which passes inside copper shielding—that it is thermally isolated from—and is directed

at the face of the sapphire substrate. Upon exiting the tubing, gas is deposited onto the sapphire substrate, building up a lattice of noble gas. For all noble gases of current interest, that lattice is expected to face-centered cubic (fcc) in structure [JRR18].

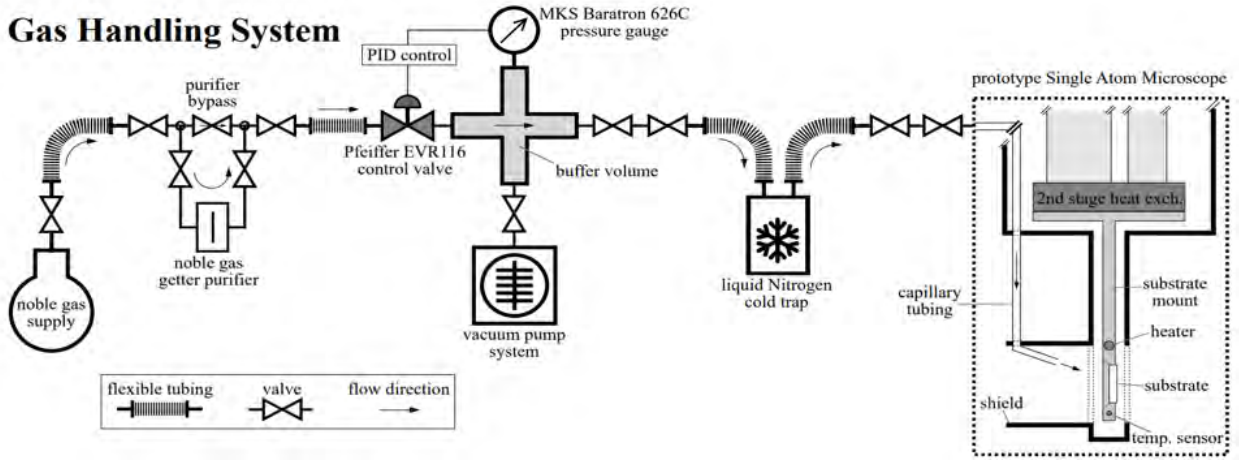

Figure 3.2: The Gas Handling System (GHS) allows for the purification and flow control of the noble gas that will be cryogenically deposited onto the sapphire substrate within the prototype Single Atom Microscope (pSAM). This figure is reproduced from BTL thesis [Los20].

Table 3.1: List of Key Components & Specifications in the Gas Handling System (GHS)

Device Type	**Vendor Model #**	**Relevant Specifications**
Kr Gas Tank	Praxair Research Grade Purity	99.999%
Dual-Stage Regulating Valve	Matheson 3120A	
Needle Control Valve	Pfeiffer EVR 116	
Capacitance Manometer	MKS Baratron 626C	0.1–100 Torr
Cold Cathode Ionization Vacuum Sensor	MKS HPS Series 423 I-MAG	$10^{-11} - 10^{-12}$ Torr

As the GHS regulates the gas flow, pSAM utilizes a few key features to control the temperature of the system whilst still allowing for optical access needed to monitor the film growth and to complete analysis afterwards. A pulse-tube cryocooler, specifically the

Cryomech PT415 Cryorefrigerator, enables pSAM to reach sufficiently low temperatures for depositing noble gas onto a synthetic sapphire substrate. This two-stage cryocooler has a cooling power of 40 W at 45 K and 1.5 W at 4.2 K, meaning that there is enough cooling power to offset the blackbody radiation from the enclosing vacuum vessel that sits at room temperature [Los20]. It is due to the cryocooler coupled with aluminized mylar shielding and a copper shield on the substrate mount that allows the substrate to reach single digit (Kelvin) temperatures cryogen-free. Additionally, the sapphire substrate's high thermal conductivity at low temperatures and using indium as a gasketing material [Los20] between the substrate and the copper mount ensures great thermal contact between the substrate and the copper mount. Temperature is recorded via sensors at two internal locations within pSAM, one at the "4K stage," shown in Figure 3.3, and one lower on the substrate mount adjacent to the substrate itself. Base temperatures achieved at each location are approximately 4.5 K and 2.5 K respectively. These temperatures meet the threshold for growing Neon films, which require the lowest deposition temperature. In conjunction with the temperature sensors, a heater (50 Ohm resistor) and a temperature controller are used to monitor and adjust the temperature in pSAM as needed. Pressure is documented as well with a micro-ion gauge.

Access to low temperatures means nothing without access for a beamline to embed atoms in the film and access for optical collection of the fluorescence from those implanted atoms. Originally, two chambers were designed and installed on pSAM to account for beamline and optical access. Note in Figure 3.3 that pSAM has a growth chamber and an imaging chamber. The first is where, you guessed it, the film is grown. This is also the level at which there can be beamline access for embedding atoms and where the turbo-molecular pump and vacuum sensors reside. The imaging chamber is also used for its namesake—optical imaging. However, pSAM was designed with some flexibility in mind, and as it turned out, thankfully

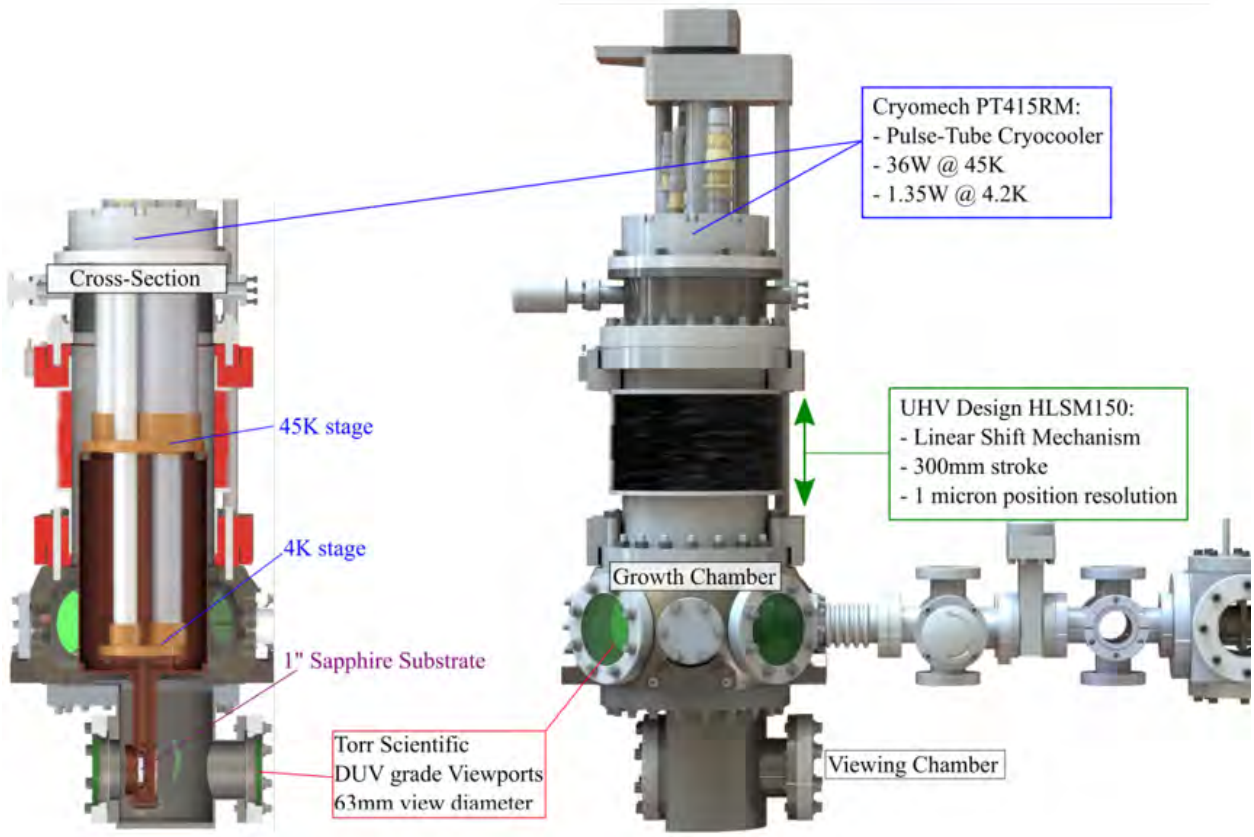

Figure 3.3: A digital rendering of pSAM shows key features such as the cryocooler, linear shift mechanism, and large viewports at each chamber. Note the cross section which shows the one-inch sapphire substrate for scale. Additionally, note the atomic beamline at right of the growth chamber. This in-house "beamline" will be discussed in Chapter 4, but it is also the location for true beamline access and recoiling products to travel down. This figure is reproduced from BTL thesis [Los20].

so. The substrate shield protruding from the flat, vertical, copper mount has cutouts for laser access through any film on the substrate. Since both chambers have large viewports, the growth chamber is also an option for imaging fluorescence from film-inserted atoms. A linear shift mechanism (LSM) works with a stepper motor providing the ability to move the substrate mount between the two chambers and finely adjust vertical position to ensure proper alignment of the film when trying to embed atoms. A residual gas analyzer (RGA) can be used for diagnostic purposes, measuring what atoms or molecules are present based on mass-to-charge ratios.

When growing a film, the GHS purifies and prepares the noble gas for deposition onto the substrate and pSAM prepares the environment in which the deposition takes place. During the film growth, the GHS adjusts the control valve to maintain the desired flow rate and stop it when the film has reached the desired thickness. It is imperative to have some way of monitoring the thickness of the film growth in real time. To do that, a laser diode is manipulated with a beam expander, beam splitter, and various lenses and mirrors so that the laser power and transmission can be analyzed during the film deposition to determine the growth rate. The laser path exits the diode and passes through the expander and an iris. From there it enters the splitter where part of the beam goes through a lens to focus onto a photodiode. This is where the laser power is recorded. The other part of the laser beam is raised to the growth chamber level with a set of elevating mirrors and passes through a lens, the substrate within pSAM, and another lens before focusing onto a second photodiode. Here is where the laser transmission through the substrate is measured. While the laser power should remain constant, the laser transmission, and consequently the transmission to power ratio, will exhibit an interference pattern as the film growth progresses. As the frequency of oscillations increases, the film growth rate increases. In practice, finding an average growth

Table 3.2: List of Key Components of the prototype Single Atom Microscope (pSAM)

Device Type	**Vendor Model #**	**Relevant Specifications**
Pulse-Tube Cryocooler	Cryomech PT415 Cryorefrigerator	Cooling Power 1st Stage: 40 W @ 45 K 2nd Stage: 1.5 W @ 4.2 K
Temperature Controller	Lakeshore Model 331	
Heater: 50 Ohm Resistor	Lakeshore HTR-50	5–60 K (Above Substrate)
Cernox Resistor Temperature Sensor	Lakeshore CX-1050-AA	1.4–325 K (Near Substrate)
Cernox High Temperature Sensor	Lakeshore CX-1050-CU-HT	1.4–420 K (2nd Stage Heat Exchanger)
Substrate Mount	OFE C10100 Copper Alloy	Oxygen-Free, Electrolytic
Linear Shift Mechanism	UHV Design HLSM150	300 mm linear motion
Stepper Motor	McLennan 23HT18C230	Fitted to 50:1 IP57 Gearbox
Sim-Step Microstepping Motor Drive	McLennan MSE570M	
Sim-Step Stepper Motor Controller	McLennan PM1000	
Micro-Ion Gauge	MKS Series 392	$10^{-9} - 760$ Torr
Residual Gas Analyzer (electron multiplier)	SRS RGA200	m/q = 0–200 amu $10^{-4} - 10^{-10}$ Torr (off) $10^{-6} - 10^{-12}$ Torr (on)
Diode Laser	Thorlabs CPS635R	638 nm, 1.2 mW (typically)
Fixed Gain Detector (Photodiode)	Thorlabs PDA10A	200–1100 nm
10x Beam Expander	Thorlabs GBE10-A	400–650 nm
Beam Splitter	Thorlabs CM1-BS013	400–700 nm
Fused Silica Viewport (Anti-Reflective Coating)	Torr Scientific Ltd VPZ64QBBAR	2.5" view diameter (700–1100 nm)

rate is done by measuring the "distance" between several maxima or minima, counting the number of oscillations over that distance, and using the index of refraction for the type of film you are growing. The "distance" between peaks when viewing them corresponds to the time between points of data. The number of peaks corresponds to a specific thickness grown which will depend on the orientation of the laser beam and the index of refraction of the film type. With a thickness and time, the film growth rate is calculated and then used to find the length of time the deposition should continue before using the GHS controls to end it. Film thickness can be calculated with the equation:

$$t = \frac{1}{2} m\lambda (n^2 - sin^2\theta)^{-1/2} \tag{3.1}$$

where t is the thickness of the film correlating to the number of m oscillations in the interference pattern, λ is the laser diode wavelength of 638 nm, n is the index of refraction (1.38 for krypton [SK74]), and θ is the angle of incidence of the laser beam onto the substrate—which is 45° in this case [Los20, Goo78]. Putting these numbers together results in a thickness of about 293.6 nm for each oscillation in the interference pattern. Note that it is recommended to use only maxima or minima when finding m, which means its value is either an integer or half-integer. Knowing the thickness that an oscillation corresponds to was especially useful for growing the films needed for the calibration studies. As those films are only 5 μm total, counting the total peaks, which is not feasible for thicker films, became a very useful method.

The equipment and processes shared in this section are for growing films that are to be used as solid traps. However, the equipment is the same for the very thin films grown for calibration studies described in the next chapter, with the addition of optics and materials to implant atoms within the film. Similarly, the general process is nearly the same, excepting

adjustments for embedding atoms. In the next chapter, the other equipment and alterations to the process are explained.

3.2.2 Equipment Used to Study a Film

There are four main categories of data collected throughout the film growth and analysis processes. All equipment used to gather the first three categories of data are in Table 3.1 and Table 3.2 in the previous section. Equipment needed for the fourth category is included at the end of this section in Table 3.3.

First, there is the GHS data which includes pressure readings and the noble gas flow rate settings. Notation of the pressure readings are important for preparation for a successful film growth, but the gathered data is recorded during the growth itself and used as one diagnostic to help determine if the film growth was overall normal. If the pressure went up for a higher gas flow when it should have and remained relatively constant, then that means that from the GHS perspective, the film growth went as expected. Any anomalies can indicate a problem with the regulator setting on the gas tank or an issue with the Pfeiffer control valve or gas flow pathway.

Secondly, there is the collective pSAM data. This data includes pressure and temperature measurements before, during, and after the film growth. This is mainly used as another diagnostic tool. Before film growth, pSAM needs to be pumped down to vacuum if not done already, then cooled down, and when the pressure and temperature are both stabilized and within the typical and safe ranges, then the film growth may begin. During the film growth, this data is monitored as an alternate perspective to see that the deposition occurs normally. If there is a malfunction with something that causes a change in temperature, then the noble gas may not deposit regularly. A sudden pressure drop could indicate a clog in the gas flow

path preventing it from reaching the substrate. Additionally, after the film growth, pSAM data is noted to confirm the pressure decreases and stabilizes once the gas flow path is closed.

The third category of data is the thin film thickness (TFT) data. TFT data includes the diode laser readings. As described in the previous section, this data—the power reading and the transmission through the substrate—is used to determine a growth rate in real time so that the deposition ends when the film reaches its desired thickness. Afterwards, this data is used with a peak finding algorithm to try to determine a more accurate estimate of the total film thickness. Some manual efforts are required as the algorithm is currently limited in its ability to distinguish between smaller amplitude peaks or uneven interference patterns. This data is also useful for confirming that the diode laser power was consistent and for showing a general trend in the transmission, but a better analysis of the transmission is done with the last category of data.

Finally, the fourth main category of data recorded is referred to as the white light source (WLS) data. Prior to and after the growth of the film, the broadband transmission of light from a deuterium-halogen light source is measured. These measurements show how much light gets through an "empty" substrate without a film and how much light gets through the substrate with a film on it. Gathering this data utilizes a light source, optical fibers, lenses, and a spectrometer. With this data, and an additional background measurement with the light source turned off, the film quality can be quantified. The setup for the equipment used in these measurements is illustrated in Figure 3.4. Summarily, the light source is directed through a fiber. Accompanying optics are positioned to shine the light through the film and substrate to the opposite lens, which focuses the light into an optical fiber connected to the spectrometer. Furthermore, the WLS data can be collected on a continuous basis to measure the film's transmission over time. Because films are light-sensitive, this has been

done only a couple of times during a film growth. More often it is done after the film growth ends to see how the transmission decays. High quality films—those with high transmission—can last for days without notable decreases in transmission. In this case, the pSAM data is recorded concurrently. Typically there would be a gradual trend in the decay of a film. Anything outside of this norm can usually be explained with the help of the pSAM data. For example, if the film is maintained at the upper end of the suitable temperature range for possible depositions, sometimes the film can begin to sublimate. Pressure changes in the pSAM readings can help support or refute this conclusion.

Table 3.3: Additional Equipment For Film Studies

Device Type	**Vendor Model #**	**Relevant Specifications**
Deuterium-Halogen Light Source	Ocean Optics DH-2000-S-DUV-TTL	190–2500 nm
Optical Fiber	Thorlabs MHP550L02	
Fiber Collimating Lens	Ocean Optics 74-UV	
Focusing Lens	Thorlabs LA1951-A	AR Coating 350–700 nm
Spectrometer	Ocean Optics Flame-S-VIS-NIR-ES (current)	350–1000 nm
	Flame-S-UV-VIS-ES	200–850 nm

3.3 Film Quality Analysis

3.3.1 Quantifying Film Quality

Measuring the transparency of a film via the transmission of light from the white light source (WLS) enabled careful determination of the ideal parameters for film deposition. Transparency of a film is measured using the film's transmission ratio which divides the amount of

light that gets through a film by the amount of light that transmits without a film present. Background is subtracted off of each—the numerator and the denominator. As described briefly in the previous section, three pieces of data are collected for this measurement: one spectra of the WLS transmission through the substrate before a film is grown, one spectra after the deposition of the WLS transmission through the film on the substrate, and one spectra with the WLS closed for a background measurement. This is used to construct a transmission ratio.

$$\text{Transmission Ratio} = \frac{\text{With Film} \ - \ \text{Background}}{\text{No Film} \ - \ \text{Background}} \tag{3.2}$$

Previously the WLS and spectrometer was used almost exclusively. However, the amount of light transmitted can be measured with the spectrometer as counts versus wavelength or now with the CCD (Charged Couple Device) camera as count distribution spatially (2D). The WLS measurement to find the transmission ratio is usually done in the imaging chamber of pSAM, though it can also be done in the growth chamber if you have space for the optics. With fluorescence measurement optics in place for doped film growths, the optical real estate is limited and the imaging chamber provides a direct view rather than one at a 45° angle. Figure 3.4 illustrates the setup for a WLS measurement through the imaging chamber with the spectrometer.

The dominant parameter for optimizing a film's transmission is the deposition temperature. Figures 3.5 and 3.6 illustrate this point. In Figure 3.5, the film clarity is vastly different between the two films. The film clarity correlates to their transmission ratios, though it should be noted that a film may look clear to the eye but when back-lit be cloudier than expected. The WLS data should be relied on to quantitatively know about a film's

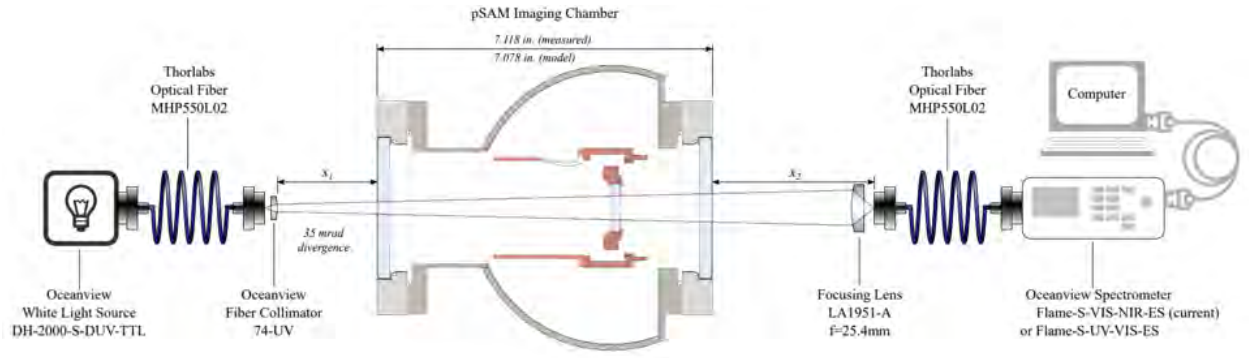

Figure 3.4: To quantify a film's transmission, a white light source is shone through the sapphire substrate before and after a film is grown and collected by a spectrometer to determine the amount of light getting through the noble gas film. This figure is reproduced from BTL thesis [Los20].

transmission. There is a distinct, undeniable pattern between the transmission ratio and the deposition temperature. In Figure 3.6, a sample of transmission ratios over wavelength for several Kr films deposited at varying temperatures is shown. In this case, with this version of pSAM, the ideal temperature, to have the highest transmission ratio across the full wavelength range, was 36 K.

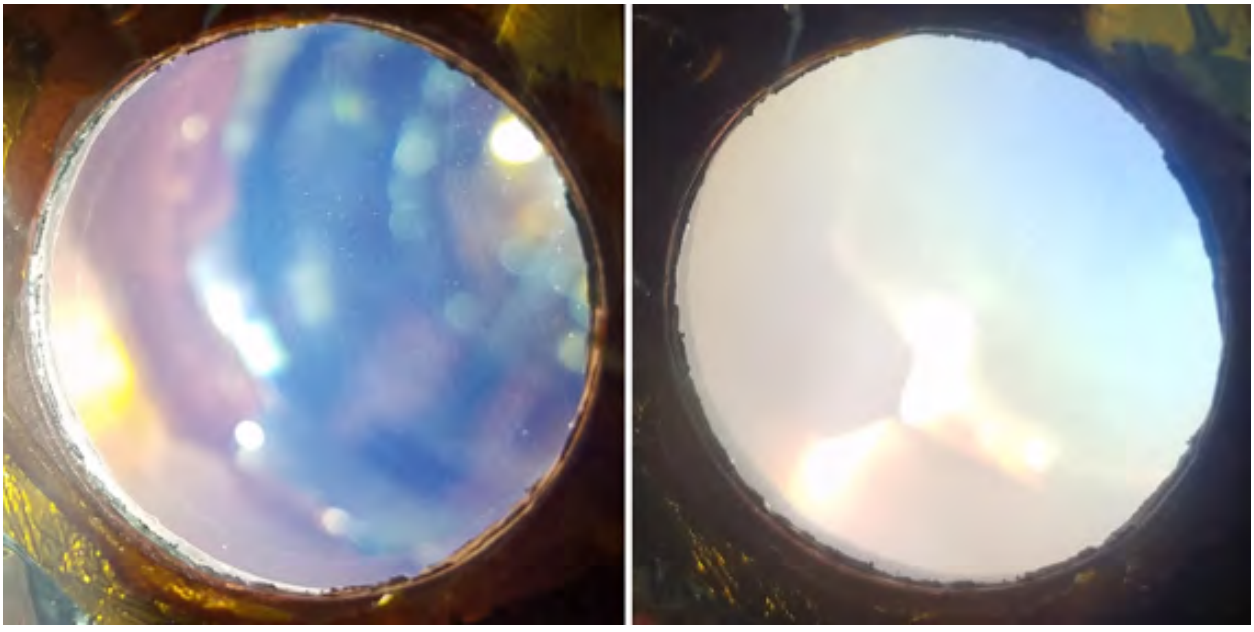

Figure 3.5: Two examples of noble gas films grown in pSAM. On the left is a clear film with a high film transmission ratio and on the right is a cloudy film with a low transmission ratio. This figure is reproduced from BTL thesis [Los20].

There are a few interesting qualities of Figure 3.6 worthy of explanation. For one thing, each of the plotted lines have oscillations present. This is indicative of an interference pattern caused by the presence of a "back-film"—a film unintentionally grown on the back side of the substrate. As noble gas flows through thin tubing aimed at the substrate, most of it is deposited on the front face of the substrate. A small portion of it manages to float around to the back face of the substrate where it adheres and produces an incredibly thin back-film. Measuring the wavelength of the oscillation pattern allows for the calculation of an inferred back-film thickness. On average, the intended film's thickness is approximately 100 μm and the back-film about 5 μm. In addition to the mere presence of oscillations, the figure shows that the amplitude of them decreases at lower wavelengths. This is caused by the back-film's variance in thickness.

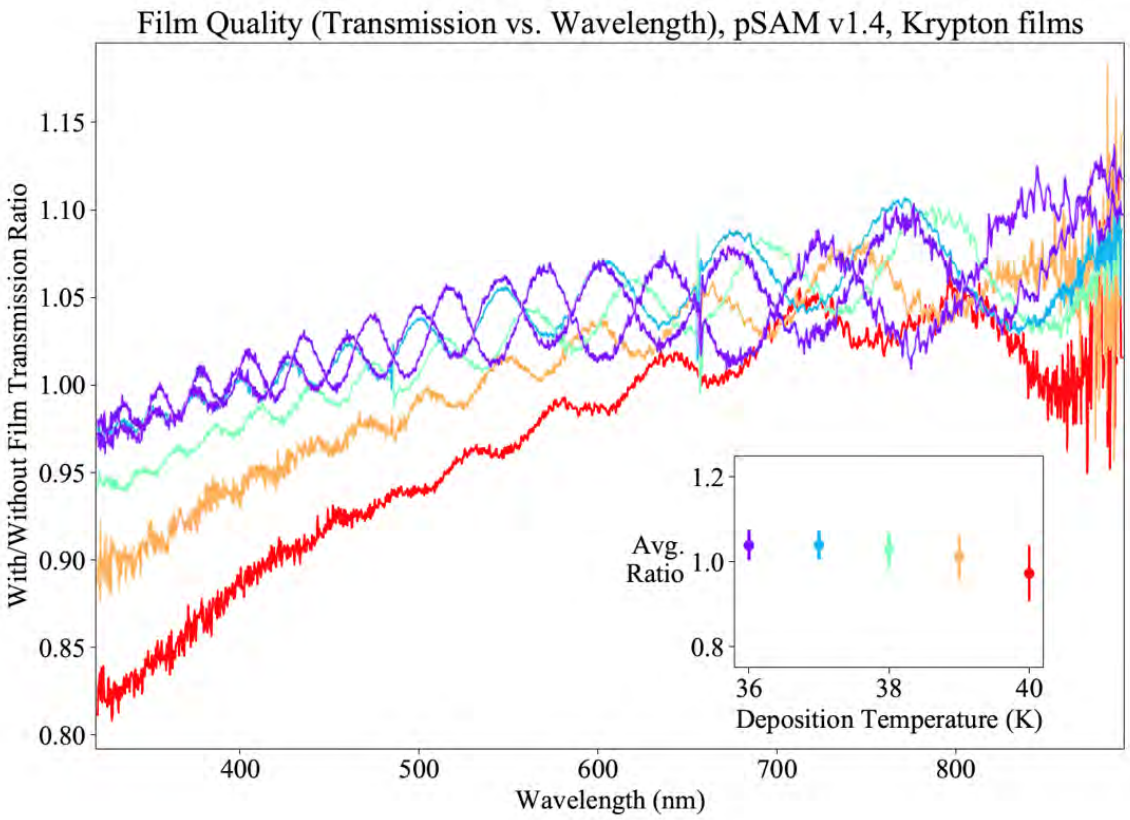

Figure 3.6: The Transmission Ratio of six films grown at various deposition temperatures are shown on this plot. Note that there are two films grown at 36K.

In addition to the oscillations, note the value of the transmission ratio across Figure 3.6. As the transmission is measured as a ratio, intuition expects a maximum ratio of one. However, as seen in the figure, the maximum transmission ratio can exceed one, translating to more light transmitting after the film is deposited. In fact, an average transmission ratio—the transmission ratio averaged over all wavelengths—of a very clear film is often about 1.15 now, with 15% more light transmitting through the film than through the substrate alone. The increased transmission is caused by the anti-reflection coating effect.

At the surface between two mediums, light can either transmit or reflect. Without a film grown, there are only two boundaries to be wary of (aside from the viewports) which is the front and back face of the substrate—surfaces between sapphire and vacuum. After

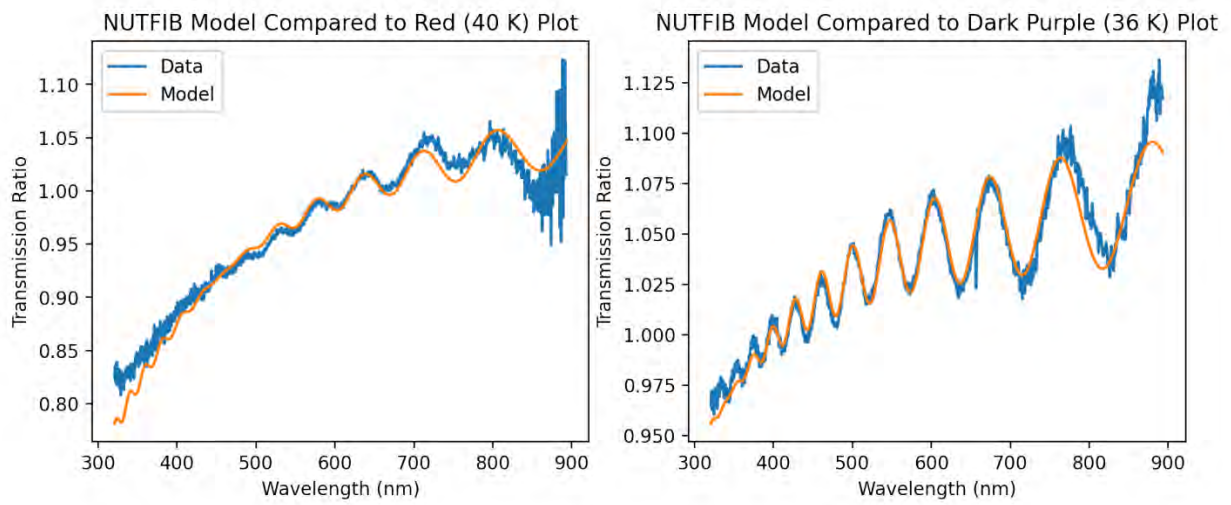

Figure 3.7: The Bubble Model was used to describe the interference pattern created from light scattering in the noble gas films. According to the model, the scattering results from vacuum pockets within the film. These plots were the work of Joseph Noonan reproduced from a technote he wrote [Noo21].

a film is grown, there are then boundaries from vacuum to film, film to substrate, substrate to back-film and finally back-film to vacuum. At each boundary, other than the first, light that is reflected can then transmit or reflect at the next surface it hits.

Referring to Figure 3.6 again, one last feature to note is that the transmission of each film appears to decrease at lower wavelengths, especially those of films grown at higher temperatures. This is caused by a type of light scattering throughout the film known as Mie Scattering. Typically, Mie Scattering is due to particulates in a film. On the contrary, what created the best model was describing the "particulates" as small, spherical vacuum pockets, or bubbles. The Bubble Model yielded that dispersed throughout the films there are significantly fewer bubbles than noble gas atoms, but that the bubbles are larger than the size of the atoms [Noo21]. Further, none of the scattered light is transmitted, so the more bubbles—vacuum pockets—there are, the lower the film quality. The Bubble Model also revealed that it is a valid assumption that the substrate and back-film do not have vacuum

pockets and that the bubbles' radii and density in the intended film are uniform [Noo21].

With a CCD camera, analyzing films spatially is possible. A short study was conducted of the film's spatial transmission using approximately the same method. Instead of the light transmitted being directed into the spectrometer, it was measured by an earlier model CCD camera (Andor Clara). With the CCD camera, the film's image must be focused onto it so there are some optics to consider and a filter should be used. The limited data analyzed did not show a clear pattern of non-uniformity in the transmission ratio across the film and showed a standard deviation of less than 10% for the high quality film analyzed. There were several limitations to this study including the specifications of the CCD and considerations that were not yet implemented as far as removing pixels that were out of the film/substrate area. This would be an interesting study to conduct again as the new CCD camera is higher quality and much of the legwork is already done now that similar techniques were needed for the fluorescence analyses. Analyzing a film spatially was done during the calibration studies described in the next chapter in the context of laser power scans and where Rb atoms embedded based on the fluorescence observed. However, there was no WLS present for images taken of un-doped Kr films and no transmission ratio calculated via the CCD because of that.

3.3.2 Film Growth Conclusions

Since the GHS and pSAM give control over several parameters, each was adjusted when originally doing film growth studies to produce the highest quality films. The main conclusion was that deposition temperature is the most impactful parameter. There are a range of temperatures for each noble gas that will allow for film deposition. These ranges increase with atomic mass, meaning Neon requires a lower temperature for deposition than Krypton.

Neon is the lightest noble gas able to be deposited as Helium is inaccessible due to the extremely low temperature it requires. Thus far, pSAM has been used to grow Neon, Argon, and Krypton films. Though there are a range of temperatures that will produce these films, there is an ideal temperature that will produce the clearest films with the highest transmission. It was found that some deposition temperatures within the range will produce hazy or even fully opaque films. Based on the film studies previously conducted, Neon is optimally grown at 8 K or base temperature around 4.6 K if it can be stabilized enough for the film not to shatter; Argon should be deposited at 27 K; and Krypton films are ideally grown at 34 K [Los20].

Another aspect of the film growth that affects the success to some lesser degree is the flow of gas from the GHS into pSAM. The parameters shared in Table 3.4 show parameters that under usual circumstances do not lead to clogs in the flow path and have the best transmission.

Table 3.4: Typical GHS Parameters For a 100 μm Kr Film

Stage Duration (min)	**Stage Pressure (Torr)**	**Ideal Flow Rate (Torr*L/s)**	**Ramp Up Rate (Torr*L/s)**
1	5	3.28E-6	2E-3
38	125	1.4E-3	1E-2

Since growing films that are clear is paramount, there is an inherent question about the possibility of improving a film's quality after it is grown. Some think annealing is the answer to that question. The idea of annealing films is to take a "bad" film—a cloudy one—and warm it up so that the atoms can realign themselves into a clearer crystal structure before cooling it down again. To see if annealing was a worthwhile tool, the following annealing studies were completed.

Films were grown without annealing first to create a baseline, shown in Figure 3.8, to

see how they act over a period of at least 24 hours. The baseline includes Argon films grown in the range of 22K to 34K, increased in increments of 2K. Since the film grown at 24K was a terrible initial film quality of almost zero, it was the first one on which annealing was attempted.

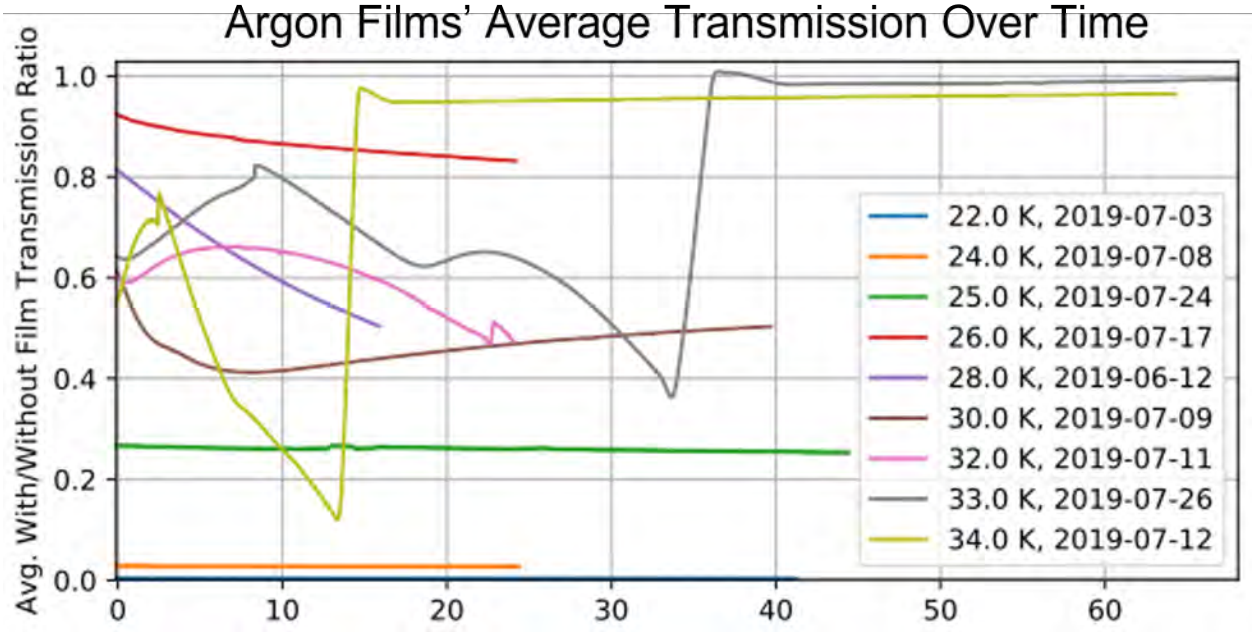

Figure 3.8: Annealing

The process used to anneal was simple, though there are several aspects that can be changed. First, a film is grown at some temperature that will yield a film that is at least somewhat unclear. Immediately after film growth and an initial transmission scan, the white light source (WLS) continuous monitoring is started. In this type of monitoring, the average transmission over all wavelengths is recorded over time. The data is saved for a few minutes before changing the temperature. The temperature is increased to an annealing maintain temperature which is maintained for at least several minutes or until the film is no longer increasing in quality, whichever length of time is longer. Then the temperature is lowered back to the deposition temperature and the data is saved for a few minutes at the before

completing the scanning. A post-anneal film quality scan is also taken to compare with the initial film quality scan. Finally, WLS continuous monitoring is resumed to see how the film's quality decays over time for comparison to the decay of films grown at the same temperature but that did not undergo annealing.

As mentioned there are several aspects of the annealing process that can be adjusted. They include: initial growth temperature, annealing max temperature, temperature ramp up rate, temperature ramp down rate, annealing maintain time, and if there is a repeated series of annealing. The repeated series of annealing would involve using an annealing process multiple times to see if the quality can be improved repeatedly. It should also be noted that the initial growth rate may play a factor in the initial film quality and that there may be a "point of no return" for films with too low a quality. For the first set of tests, each film grown had the temperature of its surroundings increased at a rate of 0.1 K/min—the slowest possible with the current setup—up to 30K, maintained at 30K for approximately 35 minutes, then decreased at 0.1 K/min to its deposition temperature. After seeing no notable increases in film quality in three annealing tests that used films grown at different temperatures, a few changes were made.

Films were grown and monitored at 25K and 33K because it appeared that 25K may be a good film quality to start at—as it was estimated to have a quality between the films grown at 34K and 26K—and 33K seemed like it may be a "sweet spot" for annealing based on the long term film qualities observed in the baseline. There seems to be a pattern in the films in which the quality improves faster at higher temperatures. The quality increases then peaks and decreases or perhaps begins to melt. The film at 34K increases over 0.1 but was completely melted at about 14 hours and at 32K the quality only increases about 0.05 over five hours, so 33K was theorized to be a good middle ground. After those films were grown,

monitored, and their data was added to the baseline, a film was grown at 25K. To anneal, the temperature was ramped up to 30K and then cooled back down to 25K for monitoring. All other aspects remained the same: ramp up rate, ramp down rate, annealing temperature maintain time, and the fact that the film was cooled back to the original growth temperature. This showed positive results, illustrated in Figure 3.9, in which the overall transmission was increased nearly uniformly across all wavelenghts and the average transmission increased nearly 8%. Another positive finding was that the long term properties appear to remain the same after the film is cooled back down—a film annealed but cooled to 25K acts like the 25K un-annealed film did. For this reason it seems likely that films grown at a higher deposition temperature with a film quality prone to decreasing rapidly should be cooled to a lower temperature after growth and/or after annealing.

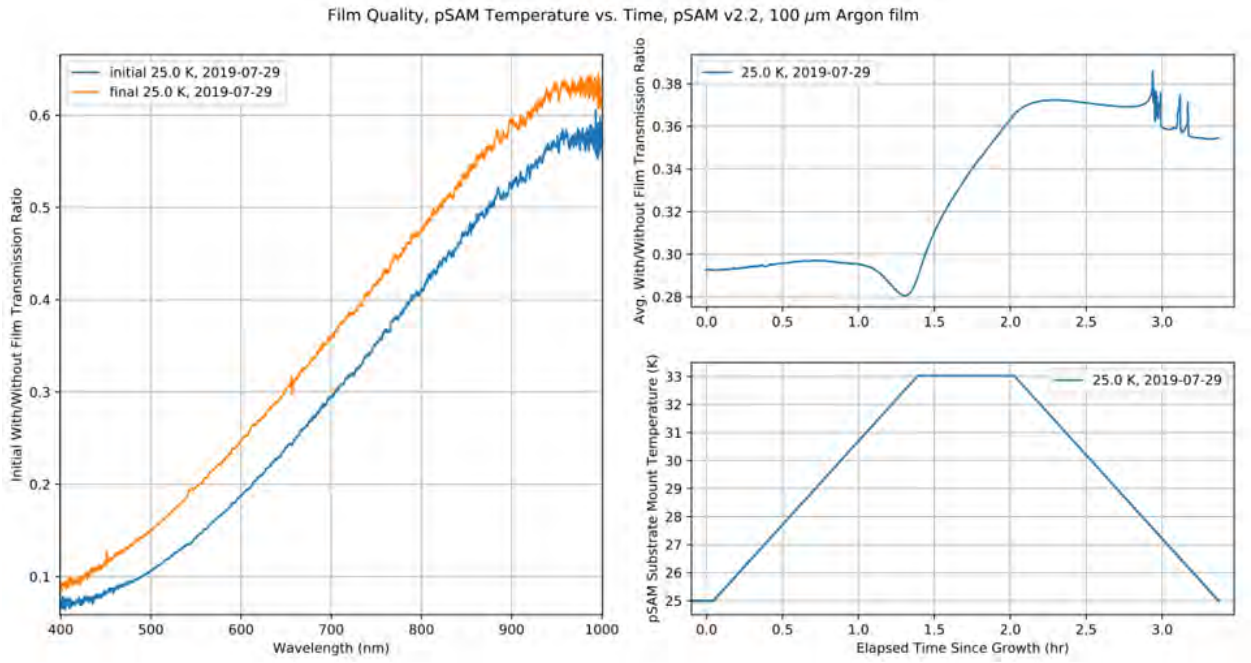

Figure 3.9: Annealing

Though 33K seems to be a good annealing temperature, seeing how much a film would improve if left at the annealing temperature longer than 35 minutes is not economical. It

is possible that ramping the temperature up and down could be done faster, but there is a risk of cracking or shattering the film, as they are not very resistant to temperature changes. The entire process for melting a bad film, preparing for a new film's growth, and depositing a new film is about four hours, so an annealing process of three hours for even a 10% increase is not enough to warrant the process. Given that the growth settings are well-known for our system at this point, annealing is not a fast enough method to be a good tool to improve a film's quality. Therefore, studies were stopped before exploring if this annealing temperature yields the same results for films grown at other temperatures.

Furthermore, it is possible that some of these films are improving in quality because they are melting, not because they are actually getting clearer. The problem is that we don't have a way to measure the film's thickness after it's been grown. One idea to test if the film is melting or getting clearer is to try to anneal a film at about 1.0 film quality. Since the best quality amongst any films is over 1, about 1.15, if the film quality is improved above 1.0, then it would be confirmed that the film is getting clearer. This wouldn't prove that the film isn't melting, but it would prove that the film is getting clearer. As stated though, the best way to get a clear film is to just grow it at the best settings from the beginning.

In September 2019, the SAM project commissioned an experiment (E19501) on ReA3 at the National Superconducting Cyclotron Facility (NSCL), now known as the Facility for Rare Isotope Beams (FRIB). There were two goals for this experiment: determine if a charged particle beam affects film clarity and determine if ions embedded in the film neutralize.

Experimental set-up, shown in Figure 3.10 consisted of a 1-cm aperture connected to an ammeter which sits prior to a Faraday cup which could be moved in and out of the ion beam of the reaccelerator line ReA3. The Faraday cup allowed calibrated measurements of the beam current, while the aperture provided constant, though uncalibrated, measurements.

Some fraction of the beam is scraped off by the aperture, enough to measure a current for a continuous measurement of the relative change of the beam intensity. Following this the ion beam enters pSAM at the substrate level, incident on a Krypton film. Two ion beams were used, one to address each goal of the experiment.

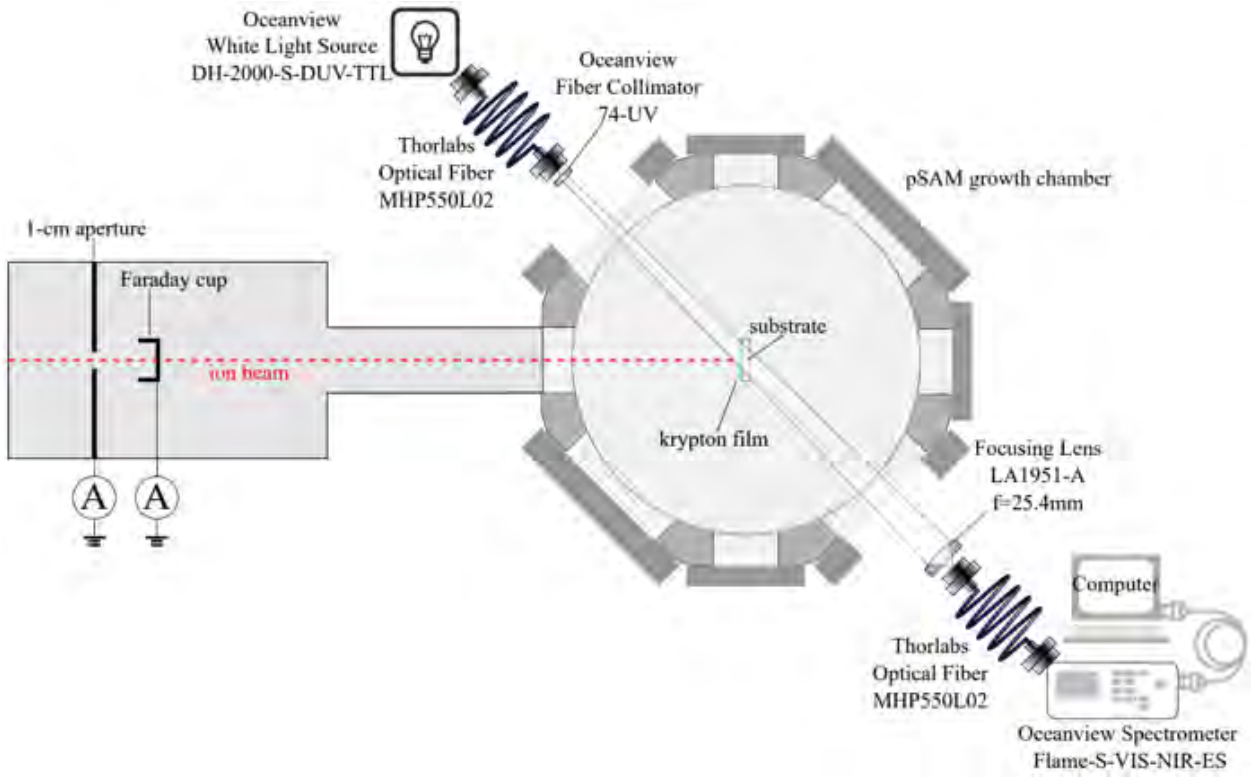

Figure 3.10: A non-proportional bird's eye view of the reaccelerator line (ReA3) to pSAM. The box at left represents the entire beamline with the ion beam indicated by a red-dashed line. The beam passes through a one centimeter aperture which is used in conjunction with the retractable Faraday cup to measure the ion beam's current. Within pSAM, the ion beam terminates at some depth within a Krypton film deposited on the sapphire substrate. Film quality assessment, as explained in 3.3, was then possible using the white light source and spectrometer setup. This figure is reproduced from BTL thesis [Los20].

First, a $^{84}Kr^{+31}$ beam with an energy of 1.7 MeV/nucleon was used to determine if the unreacted beam would affect the quality of the film. Figure 3.11 shows that the average transmission of a Kr film exposed to Kr beam eventually decayed at a similar rate to a Kr film without beam exposure. Curiously, a Kr film exposed to any beam, of Kr or Rb, seemed

to maintain its initial quality longer than one not exposed to beam.

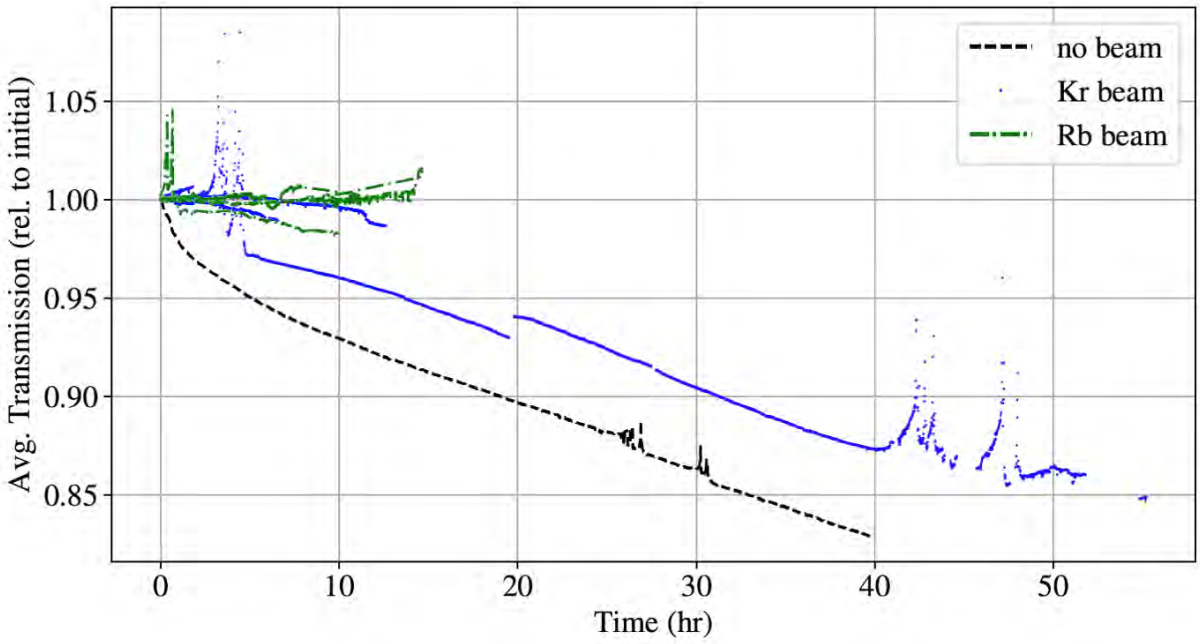

Figure 3.11: The average transmission ratio of Krypton films, all grown in the same manner, are shown over time. The quality decay rate of the film with (blue line) and without (black dashed line) a Kr beam incident on the film are approximately the same, though the film exposed to Kr beam maintained its initial quality longer. The film exposed to a Rb beam (green dot-dashed line), however, appears to decay in transparency at a slower rate, though there is less data for that film. This figure is adapted from BTL thesis, with a scale reference added [Los20].

This was physically seen on the film after moving the beam to a different location on the film—where the beam had been was still clear compared to the rest of the film which had begun to cloud. Average film transmission was taken using the WLS spectroscopy method but averaging the the transmission ratio across all wavelengths. In this way, each data point in Figure 3.11 represents the transmission averaged over all wavelengths at a point in time after the end of the film growth and initial analysis scan. An average transmission in general, could be found using the CCD camera method as well, by averaging the transmission over all pixels of the spatial plane of the film/substrate. Due to the round nature of the film on a square CCD image though, this method is slightly less accurate caused by skewing from the

corners that are off the film. For this reason, it is suggested to use an average transmission from the former method.

Spatial information was collected too, shown at left in Figure 3.13, which also confirms a Kr film virtually unchanged after exposure to 53 hours of the Kr beam. As the top and bottom green plots are nearly identical, it can be concluded that the Kr ion beam appears optically transparent on the Kr film. In other words, the Kr beam does not negatively or significantly impact the Kr film.

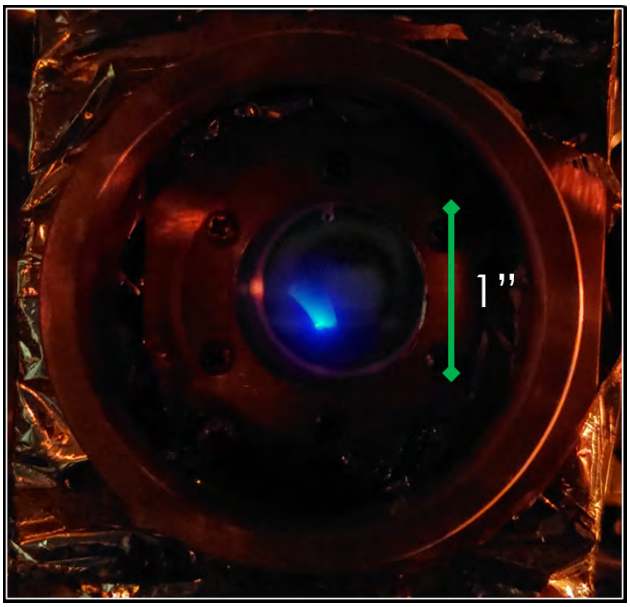

Figure 3.12: A camera image of the viewport during experimentation shows the ion beam fluorescing on the Krypton film. The scale is given by the green line marked one inch.

Second, a $^{85}Rb^{+31}$ beam with the same energy of 1.7 MeV/nucleon was used incident on a fresh Kr film. A spatial view of the film revealed that at least some portion of the Rb neutralized within the film. Note in Figure 3.13, the bottom right plot shows a bright spot. This is fluorescence corresponding to neutral Rb.

It was hypothesized that by the time Rb ions stopped in the film, it would be either Rb^{+1} or neutral. Since Rb^{+1} is optically identical to Kr—transparent to the laser light

used—the verdict is that at least some portion of the ion beam fully neutralized, since this bright spot appears. Due to uncertainties in calculating the photon to atom conversion for atom brightness, the amount of the ion beam that neutralized could be anywhere between 10% and 100%. This is why the calibration of the brightness of atoms in medium is needed.

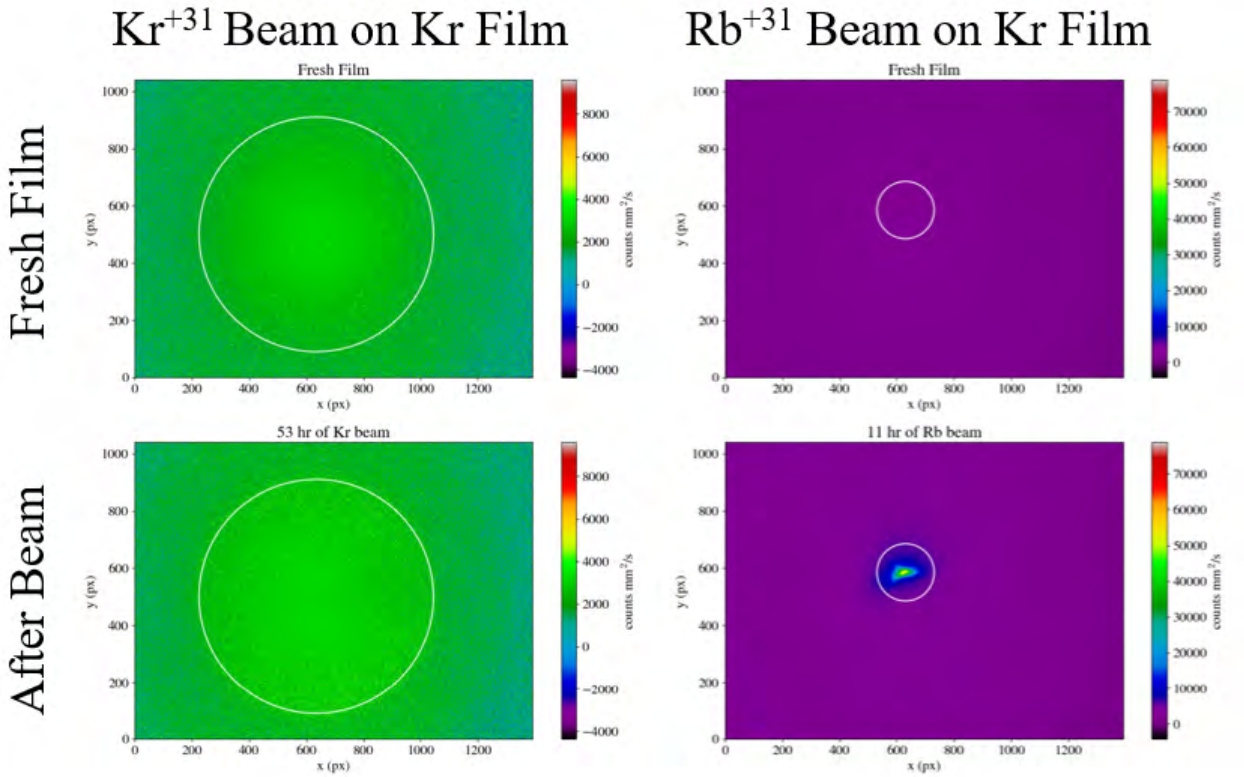

Figure 3.13: The two plots at left show results from a Kr ion beam incident on a Kr film. The top left is a spatial plot of a fresh film, while the bottom is the same film after 53 hours of Kr beam exposure. The circle represents the size of the film/substrate. On the right side, there are two plots that show a new, fresh Kr film at the top and the same film after 11 hours of Rb beam exposure. Note that the film/substrate is the same size, but this time the circle represents the region of interest in which high counts from Rb atoms fluorescing is recorded.

3.4 Conclusion

The prototype Single Atom Microscope is already outfitted to achieve the low temperatures needed to grow clear noble gas films, to allow beamline entry for embedding atoms, and to

optically access the film to collect fluorescence from the implanted atoms. Transparent films can be grown and more impressively, have their transmission measured and nearly every feature of it explained. Overall transmission is most dependent on deposition temperature, so an ideal growth temperature has been determined for growing Krypton, Argon, and Neon films. Film quality can be measured using a transmission ratio across wavelengths using the WLS spectroscopy method, a transmission ratio across the spatial plane of the film using the CCD camera method, or as an average transmission over time using either method (though the WLS option is more practical). Beamline access is not only possible, but has also been utilized to prove that the experiment is feasible as far as the film's lifetime and optical viability are concerned. It was observed that the films can not only withstand the ion beams, but also that at least a portion of incident Rb ions will neutralize by the time they stop within the film. Finally, due to the versatility of pSAM's chambers, there are options for the optics to provide sufficient measurement of the embedded atoms' fluorescing photons. As it is able to meet these requirements, pSAM is prepared as a viable method for measuring nuclear reactions. Calibrating the fluorescence of atoms in medium is needed to ensure the experiment can be successful and the process of achieving that calibration is discussed in the following chapter.

Chapter 4. Calibration of Rubidium's Fluorescence in Solid Krypton

4.1 Fluorescence Cross Section

4.1.1 Theory and Importance of the Fluorescence Cross Section

The fluorescence cross section provides insight about the intrinsic brightness of atoms. In this case, the goal is to determine the brightness of rubidium atoms embedded in a krypton solid. This brightness refers to the number of photons per unit time that a single embedded atom emits given a specified laser intensity and frequency. To assert the fluorescence cross section from the experimental setup and data, numerous models and assumptions need to be identified.

Deriving equation 4.1 takes into account the intermediate flow regime explained in the previous section for calculating the angular distribution of atoms that effuse out of the oven and for the Doppler broadening that accompanies the reality of the spread of those atoms. Further, the equation below follows the model of point-to-point imaging from one "voxel" on the film to a pixel on the CCD camera. This means that all photons emitted from atoms within one unit volume defined in the film which hit the lens will converge onto one coordinating pixel on the CCD camera. Subsequently, the solid angle factor should be based on the geometry of the lens as that is the relevant solid angle with the assumed one-to-one imaging. The lens is approximated as an infinitely thin lens. Additionally, the photon emissions from all embedded atoms are assumed to emit isotropically.

The coordinate system used in all simulations and equations including the following one

assumes that the xy planes of the oven nozzle exit, film, lens, and CCD camera are coincident such that the z-axis intersects at the center of each xy plane. With this definition, z = 0 at the oven nozzle exit.

Given the above assumptions and models, the fluorescence cross section can be calculated using the following equation:

$$\sigma_f = N_d(\vec{r_a})[[\frac{I_{laser}(\vec{r_a})}{h\nu_\gamma}][\tau_{exp} V_{bin} \frac{\frac{dN_a}{dt}}{\frac{dz(\vec{r_a})}{dt}}][\frac{j(\theta_a)}{\pi K_{norm} {r_a}^2}][\int \frac{\hat{n_\ell}(\vec{\ell} - \vec{r_a})}{4\pi \left|\vec{\ell} - \vec{r_a}\right|^3} dA_\ell]]^{-1} \tag{4.1}$$

where:

$\sigma_f \equiv$ fluorescence cross section

$N_d \equiv$ number of photons

$\vec{r_a} \equiv$ oven nozzle exit to a point in the film

$I_{laser} \equiv$ laser intensity

$h \equiv$ Planck's constant

$\nu_\gamma \equiv$ laser excitation frequency

$\tau_{exp} \equiv$ CCD exposure time

$V_{bin} \equiv$ volume of film bin located at $\vec{r_a}$

$\frac{dN_a}{dt} \equiv$ flow rate of atoms out of nozzle exit

$\frac{dz(\vec{r_a})}{dt} \equiv$ film growth rate

$j(\theta_a) \equiv$ angular distribution of atoms out of oven nozzle exit

$K_{norm} \equiv$ transmission probability found via the integral of the angular distribution, sometimes referen

$\vec{\ell} \equiv$ oven nozzle exit to a point on the lens surface (film-side)

$\vec{n_\ell} \equiv$ normal unit vector on lens surface at location $\vec{\ell}$ on lens

$dA_\ell \equiv$ area of small chunk of lens at $\vec{\ell}$

Experimentally, the parts that make up this equation can be summarized as the converted photon count rate from CCD detection, laser properties, film growth rate and pixel-correlated volume, atomic distribution and flow rate out of the oven nozzle, and geometric factor from the solid angle. With the noted properties of the experimental design and equipment used,

the analysis combines the ABF data and IMF data to find the fluorescence cross section.

Fluorescence cross section (FCS) can also be thought of in terms of the absorption cross section. The difference between these two values is only a quantum efficiency factor as shown in equation 4.2. As the absorption cross section was unable to be measured in this collection of data, the quantum efficiency factor cannot be defined. However, conceptually it is worth noting the relationship between the two. Relating to this context, the absorption cross section is imbued with the probability that an excitation will occur given specified parameters of the laser excitation. The fluorescence cross section is the flip side infused with the probability that an emission will occur given the same parameters. If the quantum efficiency were maximized at one, then the normalized rates at which excitation and emission occur would be equal.

$$\sigma_f(\nu_\gamma, \nu_f) = f_{QE}(\nu_f)\sigma_a(\nu_\gamma) \tag{4.2}$$

The transition rate of atom from the ground to excited state can be written as

$$R(\vec{r}) = \int_0^{\inf} \phi(\nu, \vec{r})\sigma(\nu)d\nu \tag{4.3}$$

where:

$$\begin{aligned} R(\vec{r}) &\equiv \text{transition rate from the point of view of the atom} \\ \vec{r} &\equiv \text{location of the atoms} \\ \phi(\nu, \vec{r}) &\equiv \text{number of photons per time, area, and frequency} \\ \sigma(\nu) &\equiv \text{absorption cross section} \end{aligned}$$

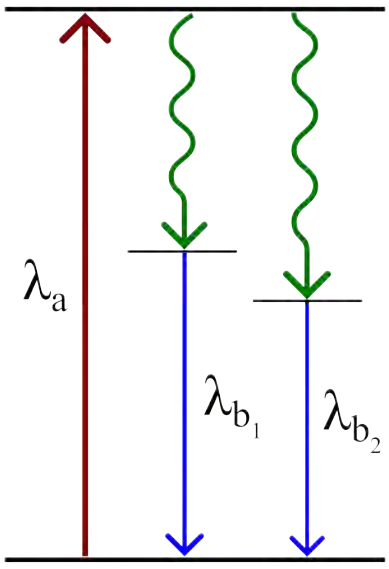

Figure 4.1: This Jablonski diagram shows the general expectation of atom excitation within a medium. Here at some laser excitation wavelength, λ_a, there is a possibility of the atom returning from its excited state to the ground state with some loss of energy via a non-radiative source, signified by the squiggly line, and then by a photon emission of wavelength λ_{b_1} or by a different amount of energy loss and then a photon emission of wavelength λ_{b_2}.

This same equation can be put in terms of photon energy, but in either case, the absorption cross section is an inherent trait that determines if a transition will occur. The rate of transition to an excited state depends not only on the innate absorption cross section, on the number and energy of photons incident on the atom, but also in a medium, attenuation of the light needs to be taken into account.

In Figure ??, a generic Jablonski diagram illustrates the main idea of the absorption of a photon from the excitation laser at one given wavelength which could result in the emission of a photon of varied energies. While the hyperfine structure of Rb-85 and Rb-87 are well described [Spe], and transitions present in the ABF data, the specifics of how these transitions translate when in a Kr film medium are unresolved. In vacuum, the excitation and emission wavelengths are the same, but in medium there is a shift in either direction away from the in-vacuum value with the excitation wavelength being lower than before and

the emission wavelength being higher than before. Given enough time, all excited atoms will return to the ground state, but how they do that exactly varies. With a perfect quantum efficiency of 1, all atoms would return to the ground state via λ_{b_1} as an example. Anything less than 1 means that some portion of atoms in the excited state reached via excitation wavelength λ_a are decaying via the route that includes an emitted photon with some other wavelength, λ_{b_2}. In this experiment, it is currently assumed that all emitted photons have wavelengths of approximately 923 nm, in other words with a quantum efficiency of 1.

4.1.2 Prospects of Single Atom Sensitivity Across the Field

Single atom sensitivity is an interest among many fields of research, including, of course, nuclear and particle physics, but also for quantum sensing and axion detection. With overlapping interests, there are several experiments trying to piece together how alkali metals behave when embedded in solid matrices. For example, observations from experiments of Rb-doped Ne films included clear evidence of resistance to photobleaching [LDUW21]. The optical properties of the embedded Rb atoms did not significantly change until $\gtrsim 10^9$ optic cycles of excitation and emission [LDUW21]. Additionally, this same experiment, though it did not calculate the fluorescence cross section, was able to calculate the laser-induced fluorescence quantum efficiency to be only about 6% within a factor of three and the quantum efficiency indicated by the radiative lifetime to be about 70% [LDUW21]. Building on this work, more experiments growing samples of Rb-doped Ne films at varied cryongenic temperatures yielded information about the temperature dependence for the optical depth and the spectrum measured [DLW21]. Since the spectrum was vastly different on a temperature range of 3.0–5.1 K, with a peak around 3.3 K, it is clear that the absorption spectra is temperature dependent, meaning that fluorescence cross sections of atoms embedded in

solid states would be as well since the fluorescence cross section is related to the absorption cross section via quantum efficiency–see Section 4.1.1 [DLW21]. Further work on this project yielded single atom detection of Rb atoms embedded in solid Ne [LDW24]. In this experiment, the total light collection efficiency based on geometry and optical elements of the setup was about 18% and the background, though subtracted off the final image, was comparable to the brightness atoms' signals [LDW24]. Varied brightness was observed for different atoms in the sample, attributed to the varied LIF quantum efficiency, which could be due to multiple trapping sites [LDW24]. With this experiment came an updated report of the quantum efficiency, now stated to be $\gtrsim 0.4$ for the brightest atoms [LDW24].

In [GSM12], samples of Rb-doped Ar, Kr, Xe, and Ne films were observed. While there was no signal observed for Rb in Ne, the excitation-emission spectra were measured in-medium for the other samples. As also observed in this work, the "blue-triplet" was recorded at 722/731/743 nm excitation wavelengths and the emission wavelength centered around 923 nm—which is not observed, but rather assumed in this work based on this previous experiment [GSM12]. Additional related experiments have studied Yb in a Ne matrix, which showed an optical background from matrix-scattered light of 17.03% [LXP$^+$21] and Rb in Ar and Ne matrices that did not measure the fluorescence cross section explicitly, but was able to measure a fluorescence signal [BCC$^+$22].

4.1.2.1 Experimental Setup

Further details of the preliminary results summarized in this section can be found in B. Loseth's thesis [Los20].

In the first attempts for atomic beamline fluorescence (ABF) and in-medium fluorescence measurements (IMF), the setup of the atomic beamline and pSAM followed that diagrammed

in Figure 4.2. Rubidium metal was contained in the titanium crucible within the oven of the ABF portion (left) of the setup. Using a tantalum resistive heating element, the vapor pressure could be adjusted such that an appropriate density of Rb atoms effused out of the crucible, via a long nozzle. This nozzle had an opening that was 10 cm long and 1 mm in diameter in an effort to produce a narrow, collimated beam of Rb atoms. While stated to be 35 mm beyond the end of the nozzle, in actuality the Rb atomic beam was intersected by the laser about 50-60 mm beyond the nozzle exit, depending on the accuracy of the nozzle length included. This intersection is depicted in Section 4.2 Figure 4.11. The emitted fluorescence was measured by an Avalanche Photodiode (APD), situated 95 mm above the intersection center. In conjunction with the reference signal from an optical chopper pulsing the laser excitation beam at a frequency of 1 kHz, the APD's output was submitted to a lock-in amplifier to improve the sensitivity.

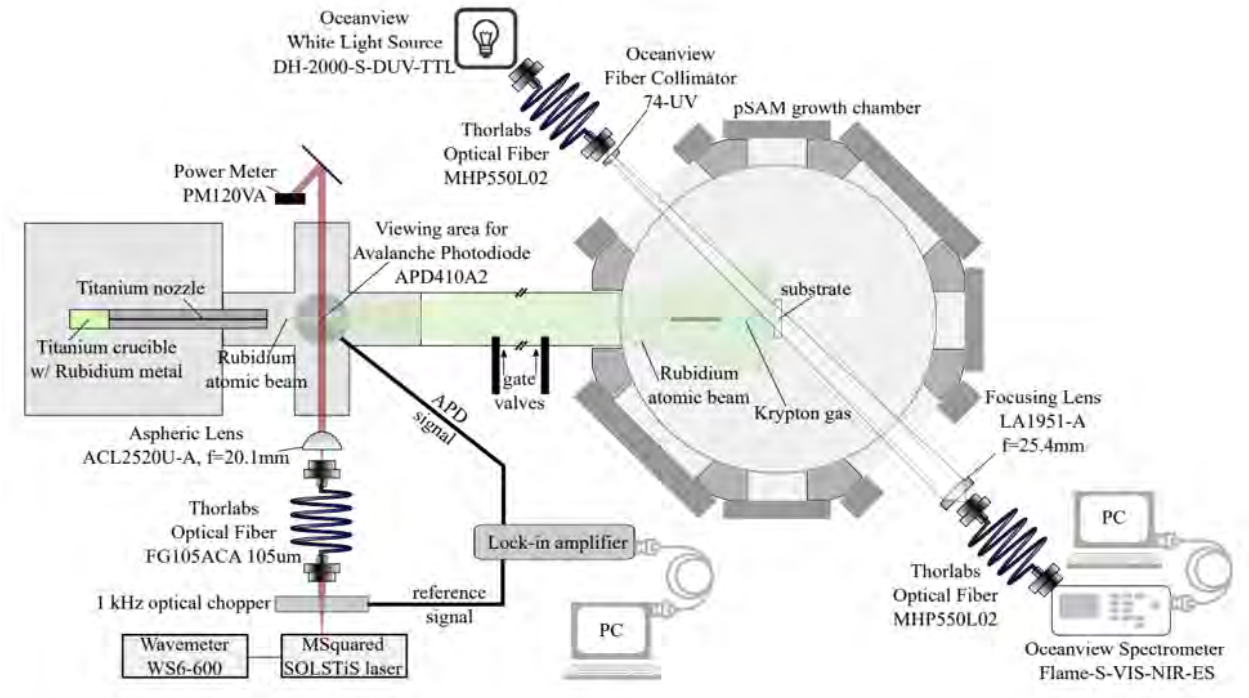

Figure 4.2: A depiction (not to scale) of the full ADF setup for conducting ABF and IMF measurements.

Table 4.1: Table of ABF laser scan parameters.

Avalanche Photodiode (APD410A2) properties			
Responsivity @ 795 nm	Transimpedance Gain	Conversion Gain	
13.75 $\frac{\text{A}}{\text{W}}$	500 $\frac{\text{kV}}{\text{A}}$	$6.875 \times 10^6 \frac{\text{V}}{\text{W}}$	
Lock-in Amplifier (SRS SR530) settings (25 °C rubidium source)			
laser power	sensitivity	time constant	approx. signal amplitude
0.3 mW	100 μV	30 ms	2 V
4.0 mW	500 μV	30 ms	7 V
Rubidium D_1 laser scan parameters			
center λ (nm)	scan width	scan rate	
794.9769	10 GHz	20 $\frac{\text{MHz}}{\text{s}}$	

At this point, fluorescence measured in the ABF intersection volume could be used to calculate the atomic beam intensity, since the fluorescence of Rb atoms in vacuum is known. The Rb atoms meanwhile traveled down the atomic beamline and codeposited with krypton on the sapphire substrate, producing a Rb-doped Kr film. Gate valves between the crucible and the substrate enabled control over embedding Rb atoms. During the film growth with Rb atom implantation, absorption measurements were taken with the use of the white light source (WLS) and a Flame spectrometer. In Table 4.1, the standard ABF laser scan parameters are shown.

Finally, at the end of the doped film's growth, the substrate with the film was moved to the imaging chamber for laser-induced fluorescence measurements. The IMF measurements were taken using the optical setup shown in Figure 4.4. With the laser fiber-coupled and collimated by an aspheric lens, the subsequent focusing lens was placed such that the uncollimated beam profile expanded until it was the size of the substrate it was incident upon. On this trajectory, the laser hit a dichroic beamsplitter which sent the laser in the direction of the substrate. At the same time, fluorescence from the embedded Rb atoms could pass through

the beamsplitter, towards a different, larger aspheric lens which imaged onto the Andor Clara CCD camera. In front of the CCD was an long-pass edge filter. The filter and beamsplitter both worked to lower the amount of laser light hitting the CCD sensor, while allowing any light greater than 830 nm to pass through. The parameters used for IMF scans of the Rb-doped Kr film are summarized in Table 4.2

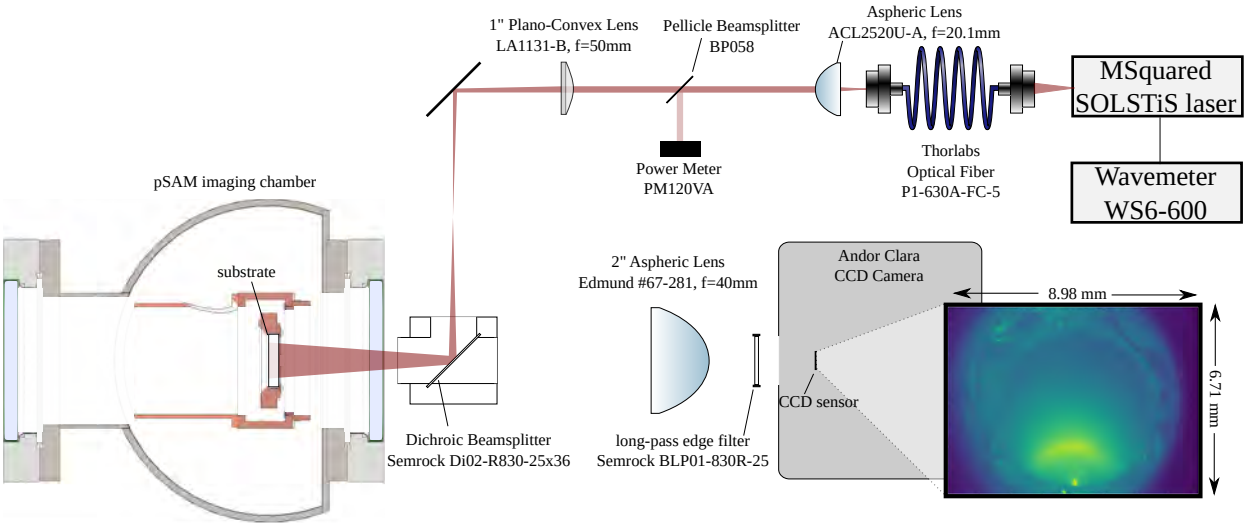

Figure 4.3: Experimental setup for fluorescence imaging of matrix isolated rubidium samples. Included is an actual image of the substrate illuminated by background light from the ion gauge. The capillary tubing for noble gas deposition is just visible at the bottom edge of the substrate (the image is inverted).

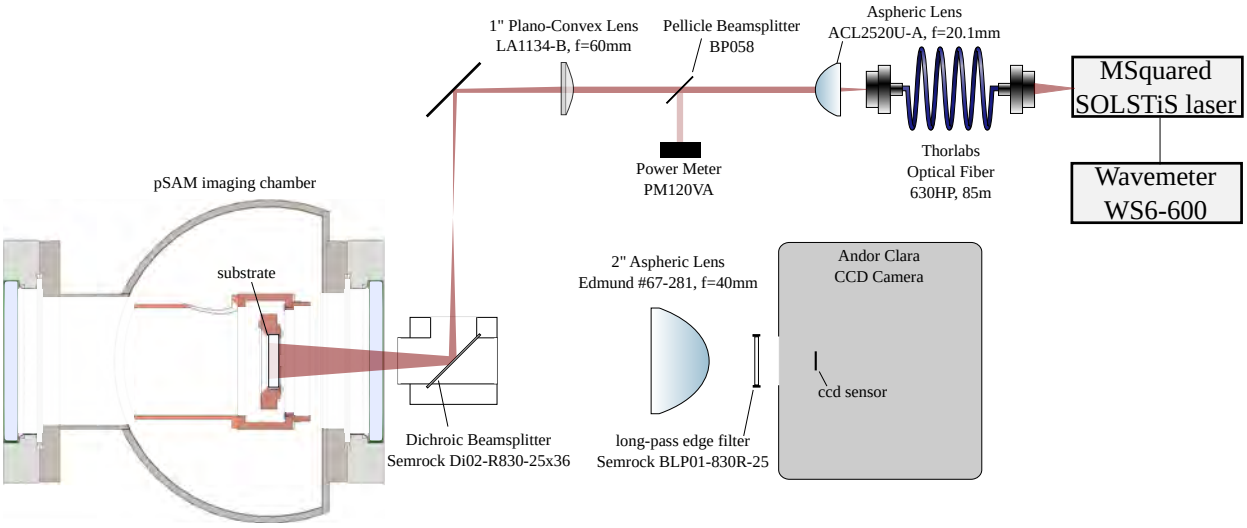

Figure 4.4: Diagram of the laser-induced fluorescence imaging setup.

Table 4.2: Table of IMF scan parameters for spectra in Figure 4.8.

CCD acquisition parameters		
exposure time	integrations	mode
0.8 s	6	Extended NIR
PreAmp gain	pixel readout rate	sensor temperature
1x	1 MHz (16-bit)	- 55 °C
laser scan parameters		
λ range (nm)	scan rate	
700 – 760 nm	20 $\frac{\text{GHz}}{\text{s}}$	

4.1.2.2 Results & Conclusions

Results and conclusions about the absorption, fluorescence, and quantum efficiency were gleaned from the observations about three Rb-doped Kr films with varied concentrations of Rb atoms implanted. All films were grown at 8 K and had growth rates around 5 μm/hr, because using the typical parameters of 34 K and between 13–140 μm/hr did not exhibit absorption or laser-induced fluorescence. These films were grown with what will be referred to as the "oreo" method, which was adapted from [GSM12] and refined in the more recent experiments shared later in this chapter. In this technique, a layer of krypton is deposited first, followed by a layer of rubidium and krypton codepositing, and finished with another layer of krypton only. This sandwiches the doped layer between noble-gas-only layers, much like America's favorite sandwich cookie. Changing the oven temperature—meaning altering the current through the heating element which surrounds the crucible containing the Rb metal—and the duration of deposition time by opening and closing a gate valve between the Rb source and substrate in pSAM (see Figure 4.2) allows control over the amount of Rb atoms embedded in the film.

For each of these three films, absorption was measured using the standard method with the white light source (WLS) to find the transmission of the films, as described in Section 3.3. Absorbance is the log of the inverse of the transmission ratio. In Figure 4.5, the absorbance of the three films can be seen to clearly show strong peaks, corresponding to high absorption of light at those wavelengths. These wavelengths correspond to two triplets related to two trapping sites within the Kr film's lattice, plus a few additional peaks which only appear for the highest Rb density film.

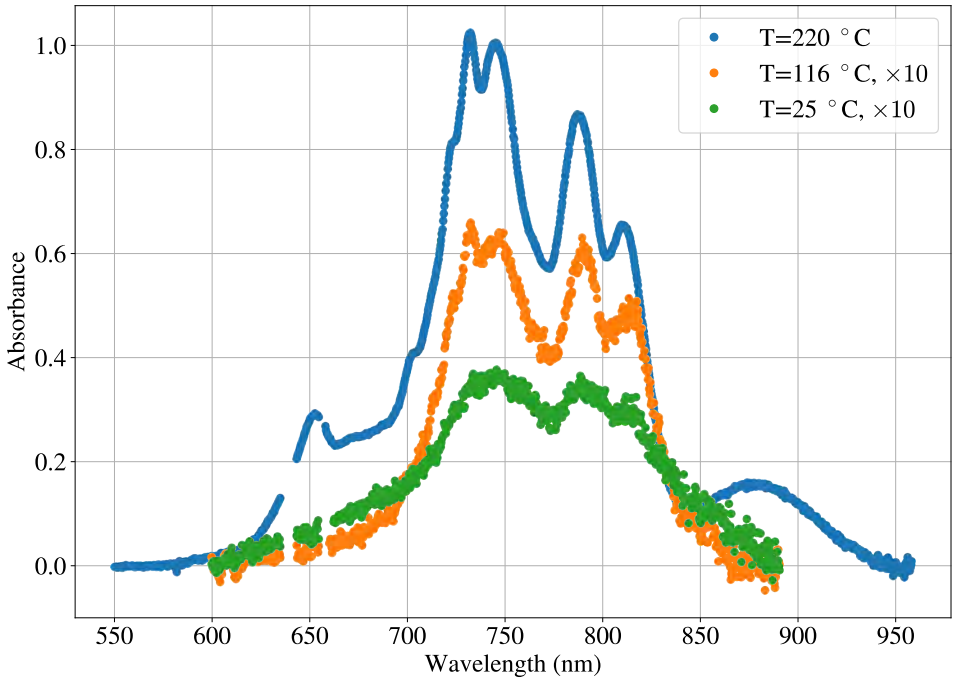

Figure 4.5: Absorption spectra of the three rubidium doped krypton films. The absorbance for films with a lower concentration of rubidium have been multiplied by 10 to aid in visibility. [Los20]

Taking the absorbance a step further, it can be used to calculate the absorption cross section. This requires knowing the angular distribution of Rb atoms out of the oven. Since the best model to use was unknown at the time, the models expected to be the upper and lower limits of angular distribution—a cosine model and a J(θ) model from [SMG$^+$98] that

excluded interatomic collisions—were both shown in Figure 4.6. The difference between these two assumed extremes was a factor of about 5.

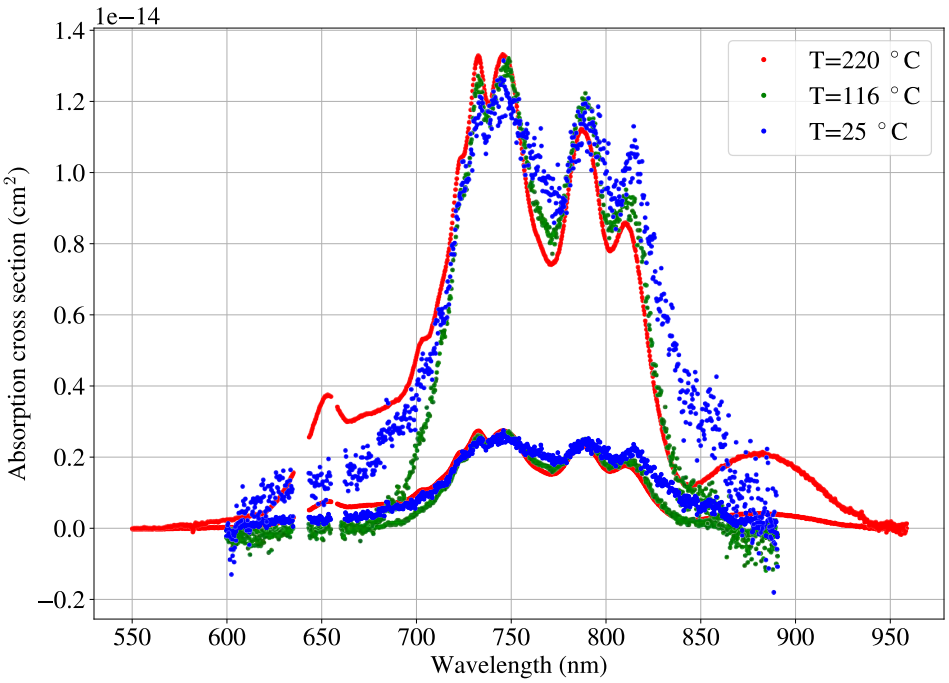

Figure 4.6: Absorption cross section of rubidium in solid krypton assuming the cosine (upper limit) and $j(\theta)$ (lower limit) angular distributions out of the rubidium source. [Los20]

To find the fluorescence cross section, as aforementioned, the number of Rb atoms implanted in the film needs to be known, which can be done through a calculation of the Rb number density in the Kr film. Analysis of ABF measurement spectra yield information about the number of atoms and their angular distribution out of the nozzle exit through the amplitudes and shapes of the peaks respectively. Figure 4.7 shows an ABF measurement representative of the Rb atomic beam during experiments with the three films of interest. The peaks agree with the literature [**?**] in terms of frequency location, but note that the concentrations of Rb-85 and Rb-87 were different. Experimentally, the breakdown of Rb-85 to Rb-87 was about 0.637 to 0.363, whereas literature denotes it to be 0.7217 to 0.2783. For an accurate extraction of the number of atoms exiting the nozzle from the ABF data,

the solid angle factor due to the size of the APD sensor and its distance from the atomic beam and laser beam interaction volume needs to be accounted for. Additionally, there is a point of saturation for the APD, so an experiment increasing the laser power to find the saturation intensity was done. Future measurements were all done well below this point of saturation for the detector. Additionally, the model for the angular distribution, again, was still unknown at the time of these experimental measurements, so many calculations were done at the presumed upper and lower limits. With the adjustments for the solid angle and APD integrated power and measured laser light intensity, the measured APD signal was used to calculate the fluorescence power of an atom and the number density of the Rb atomic beam. Integrating the number density of the Rb atomic beam over the area of the substrate with the assumption that the embedding region was 2 cm in diamter and 85 cm from the nozzle gave the number of Rb atoms implanted in the film. Uncertainty in the number of Rb atoms embedded in the film comes from the uncertainty in the laser beam radius, the position of the substrate, and namely the saturation intensity. A summary of the three films can be found in Table 4.3.

Table 4.3: A summary of growth parameters and implanted atom calculations for three rubidium in krypton sample concentrations. [Los20]

T_{source} (°C)	dep. time (s)	Kr growth rate (μm/hr)	${}^{upper}_{lower}S$ (Rb atoms/s)	N_{film} (Rb atoms)	n_{film} (Rb atoms/cm^3)	Rb conc. (ppm)
25	1452	5.29	2.6×10^{13}	2.9×10^{13}	3.8×10^{16}	1.9
			3.1×10^{12}	6.0×10^{12}	7.9×10^{15}	0.39
116	693	4.72	1.1×10^{14}	5.6×10^{13}	1.8×10^{17}	9.0
			1.3×10^{13}	1.1×10^{13}	3.7×10^{16}	1.8
220	1542	4.65	7.9×10^{14}	8.3×10^{14}	1.3×10^{18}	65
			9.4×10^{13}	1.7×10^{14}	2.7×10^{17}	13

In Figure 4.8, an IMF measurement of the Rb-doped Kr film from the film with the high-

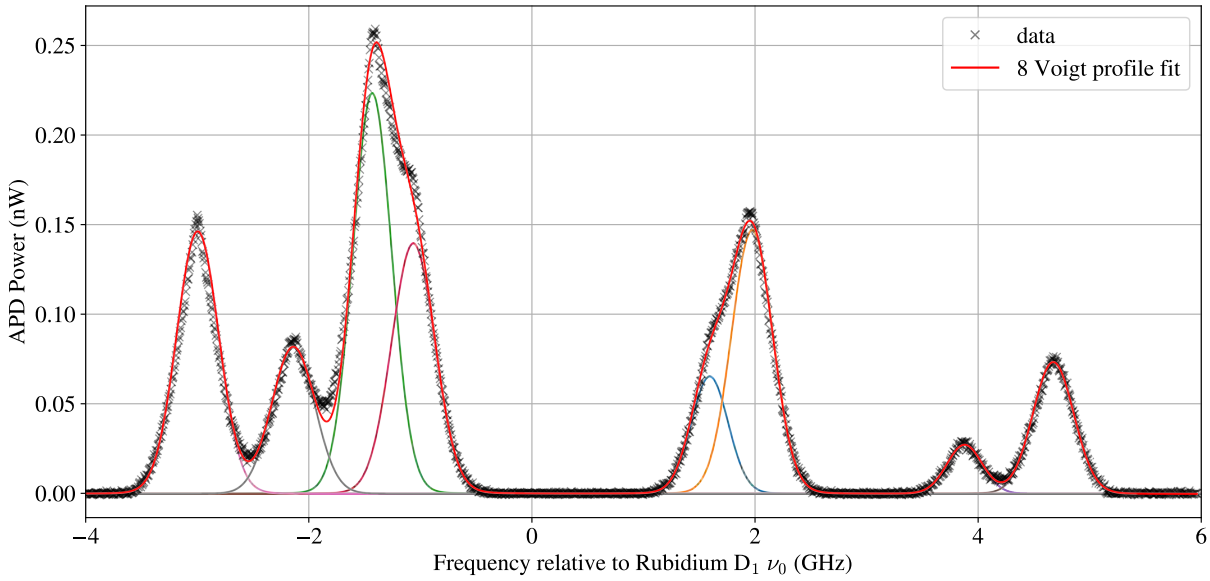

Figure 4.7: Fluorescence power as measured by the APD as the frequency of excitation light is scanned through the Rubidium D_1 transition. [Los20]

est number of Rb atoms embedded is shown (oven temperature 220degC). From [GSM12], the emission wavelength of the blue, lower-wavelength triplet is centered about 923 nm, which is the assumed wavelength being recorded by the CCD camera since its detection efficiency significantly decreases for wavelengths above 950 nm. The IMF scan is best fit to five Gaussian peaks, whose peak excitation wavelength, full-width half-max (FWHM), and resonance strength are recorded in Table 4.4. An IMF scan on an empty Kr film and on the bare substrate did not show any notable fluorescence over the background observed in the Rb-doped film.

Finally, the fluorescence power per atom was calculated. The total counts from fluorescing Rb atoms over the region of the film hit with the laser, the CCD exposure time, the wavelength-dependent CCD count to photon ratio (used with $\lambda = 925$ nm), and the solid angle efficiency of the CCD sensor from the substrate are all used to calculate the total fluorescence power. Then, dividing that by the total number of Rb atoms in the region of

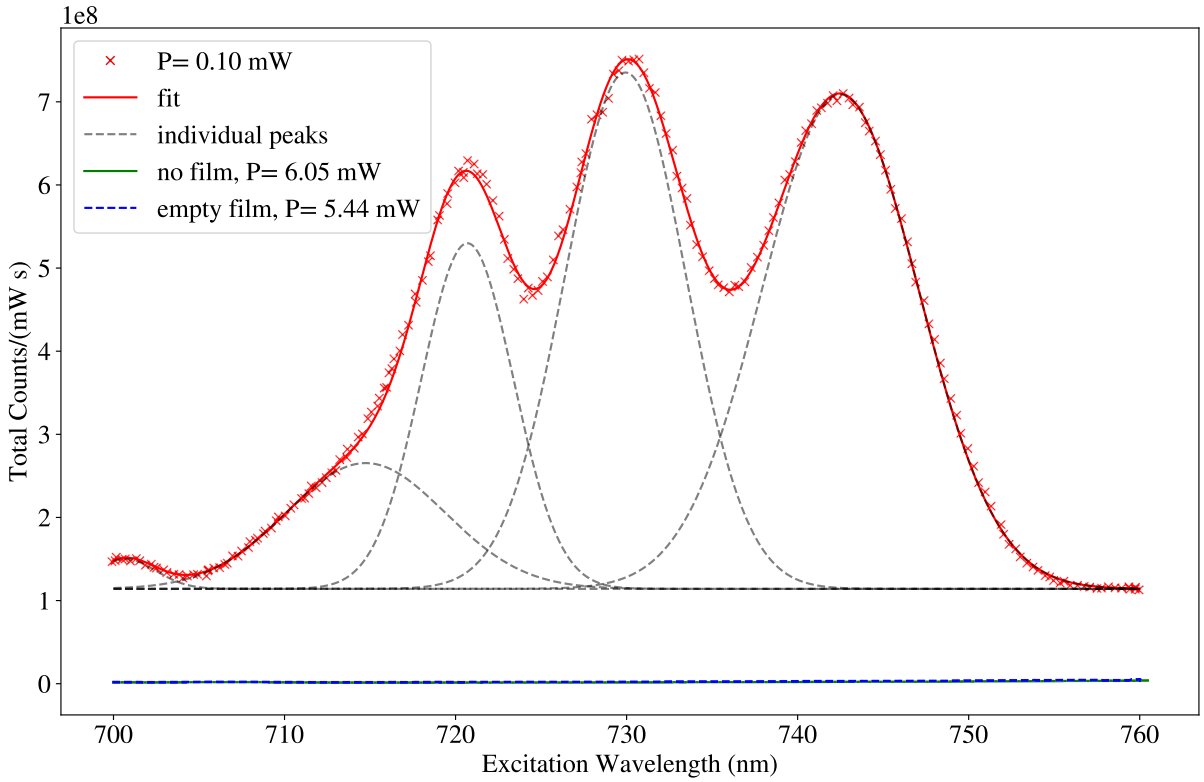

Figure 4.8: An IMF measurement of the laser-induced fluorescence spectrum for rubidium in solid krypton. The y-axis units are the total CCD count rate summed over the entire substrate and normalized to the laser power. [Los20]

Table 4.4: Laser induced fluorescence peaks for a Rb-doped Kr film, with uncertainties given in parenthesis. Here, λ is the excitation wavelength of the laser. Resonance strength is given with respect to the amplitude of the strongest resonance at 730 nm. [Los20]

λ (nm)	FWHM	strength
700.9(3)	4.1(5)	0.061(6)
714.3(5)	9.6(1.1)	0.240(9)
720.6(3)	6.6(2)	0.74(4)
730.0(3)	8.0(2)	1.000
742.5(3)	10.9(2)	0.940(8)

the film hit with the laser and by the laser intensity gives the fluorescence cross section. This division occurs when finding the slopes of the data illustrated in Figure **??**. The fluorescence power per atom of each film was plotted against increasing laser intensities and uncovered a linear relationship between them, the slope of these lines being the fluorescence cross section. Despite the absorption cross sections matching well between the three Rb-doped films, the fluorescence cross sections vary by over an order of magnitude, the film with the highest number density of Rb being on the low end. The quantum efficiency is the ratio of the fluorescence and absorption cross sections, and subsequently, these values varied more than anticipated as well due to the variance in the fluorescence cross sections. In vacuum, this value would be one as the cross sections should be equal—equal light absorbed and emitted due to conservation of energy. However, in medium, the value would be expected to be something less than one. A summary of the measured cross sections and quantum efficiencies are in Table 4.5.

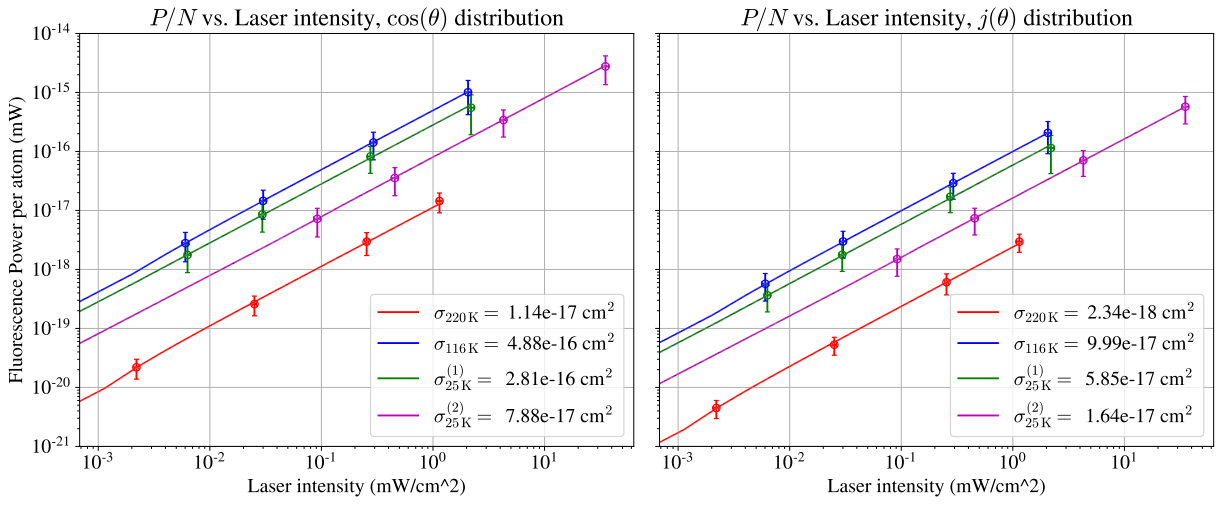

Figure 4.9: Fluorescence power per atom as a function of laser intensity for each film and for the upper and lower bounds on the predicted number of atoms in the film. The slope of each line is the fluorescence cross section σ_f. [Los20]

To conclude and summarize the previously obtained results, the absorption cross sections

Table 4.5: Measured cross sections and quantum efficiencies at $\lambda_{\text{excitation}} = 730$ nm.

T_{source} (°C)	σ_a (cm^2)		σ_f (cm^2)		ϵ_{QE}, $\lambda_{\text{emission}} > 830$nm	
	$\cos(\theta)$	$j(\theta)$	$\cos(\theta)$	$j(\theta)$	$\cos(\theta)$	$j(\theta)$
25	1.2×10^{-14}	2.4×10^{-15}	2.8×10^{-16}	5.8×10^{-17}	2.3×10^{-2}	2.4×10^{-2}
			7.9×10^{-17}	1.6×10^{-17}	6.6×10^{-3}	6.7×10^{-3}
116	1.3×10^{-14}	2.5×10^{-15}	4.9×10^{-16}	1.0×10^{-16}	3.8×10^{-2}	4.0×10^{-2}
220	1.3×10^{-14}	2.6×10^{-15}	1.1×10^{-17}	2.3×10^{-18}	8.4×10^{-4}	8.8×10^{-4}

for three Rb-doped Kr films with different concentrations of Rb implanted were consistent and corresponded to the two triplets of peaks recognized in current literature. In combination with the ABF spectra measured, it follows that the ABF measurement technique for calculating the atomic beam intensity must be at least reasonably accurate. With a refined model for the angular distribution of Rb atoms out of the nozzle exit, the factor of five difference in the absorption cross section can be greatly reduced. As it stood at this point, based on the Doppler broadening of the peaks, the cosine distribution model was expected to be the more accurate model. Continue to the next section to see how this model was resolved. Further, the IMF spectrum from laser-induced fluorescence of the embedded Rb atoms also matched with literature, but for some reason the fluorescence cross section varied with Rb concentration unpredictably. In essence, while the fluorescence power was linearly dependent on the laser intensity for all sample films, the fluorescence cross section did not have a persistent trend with increasing Rb number density. Finally, the quantum efficiencies were quite low for the in-medium samples. While expected to be less than one, the numbers are all less than 5% and vary greatly across different concentrations of Rb and different sizes of laser beam profiles incident on the films. This could correspond to a high percentage of absorbed energy being transferred nonradiatively through lattice vibrations in the film.

4.1.2.3 Refining the Technique

Since these preliminary results, several steps have been taken to improve the measurement in the forms of experimental setup adjustments, equipment upgrades, background minimization, and simulation upgrades. These efforts increased the signal to background ratio and advanced the models used to explain the physics of the measurements. The details of the updated and upgraded setup is in Section 4.3.1, but differences from the previous setup are summarized here.

A long nozzle was used in an effort to create a narrow collimated beam of atoms, but the beam observed was rather wide spread, as if there was no collimation at all. Connecting the data to the observation of what appeared to be a drip mark at the end of the nozzle, it was concluded that Rb must have leaked out the nozzle—meaning that Rb in liquid form filled the nozzle and dripped out the end before traveling as a vapor down the atomic beamline. To correct for this, when the Rb is loaded into the crucible now, it is filled less than halfway such that the level of the liquid form is fully below the nozzle opening.

A major adjustment to the experimental setup was changing the geometry of the laser incident upon the substrate and doped film. As shown previously, the laser was sent through a beamsplitter which sent uncollimated laser light normal to the face of the substrate. This resulted in a high level of laser background counts on the CCD. Instead, now the IMF measurement occurs in the growth chamber rather than the viewing chamber. This allows the laser to be sent in at a 45deg angle, while still having the CCD camera view the substrate and doped film straight on. Further, the optics used to adjust the laser beam profile size have been changed so that it is a collimated beam of light hitting the substrate/film. This means there should be little to no laser light being reflected off the interior of pSAM and that much

less laser light is reflected off the substrate directly towards the CCD sensor. Additionally, a test was done for an IMF measurement with and without the beamsplitter to determine if it was still needed. According to its datasheet, the beamsplitter has a transmission of about 95.8% for 923 nm light—the peak emission wavelength from Rb atoms embedded in Kr [GSM12]. Based on the test done, the cost of losing counts from fluorescence was not worth the possible diversion of reflected laser light, as the number of counts was not notably changed with or without the beamsplitter.

Equipment upgrades included a replacement for the Avalanche Photodiode and a new CCD camera. Replacing the APD with a single photon detector (SPD) resulted in a lower intrinsic background and a more sensitive device for counting photons. With this new device, the optical chopper, which was used to get a background reference signal, was no longer required either. Further increasing the signal to background ratio in this regime was a lens that was installed within the 6-way cross between the laser/atomic beam interaction and the SPD to focus the source atoms emitting photons onto the SPD sensor. While the lens increased the signal, a filter added directly in front of the SPD sensor, Aktar low-outgassing adhesive black-out foil installed along the entire interior of the 6-way cross, and a black-out box enclosure encompassing the ABF setup each significantly reduced the background from laser light and other external sources. An upgraded CCD camera improved sensitivity on the IMF side of measurements with black-out fabric at the end of the laser table reduced the background. Recording the bias counts of the CCD now as well gives a more accurate measurement of the counts due to fluorescence from embedded atoms. All of these physical improvements are depicted in the updated experimental setup diagram shown in Figure 4.10.

Finally, as stated in Loseth's thesis [Los20], the angular distribution of atoms effusing out of the nozzle end was not well known, noted as angular intensity J(θ), and therefore two

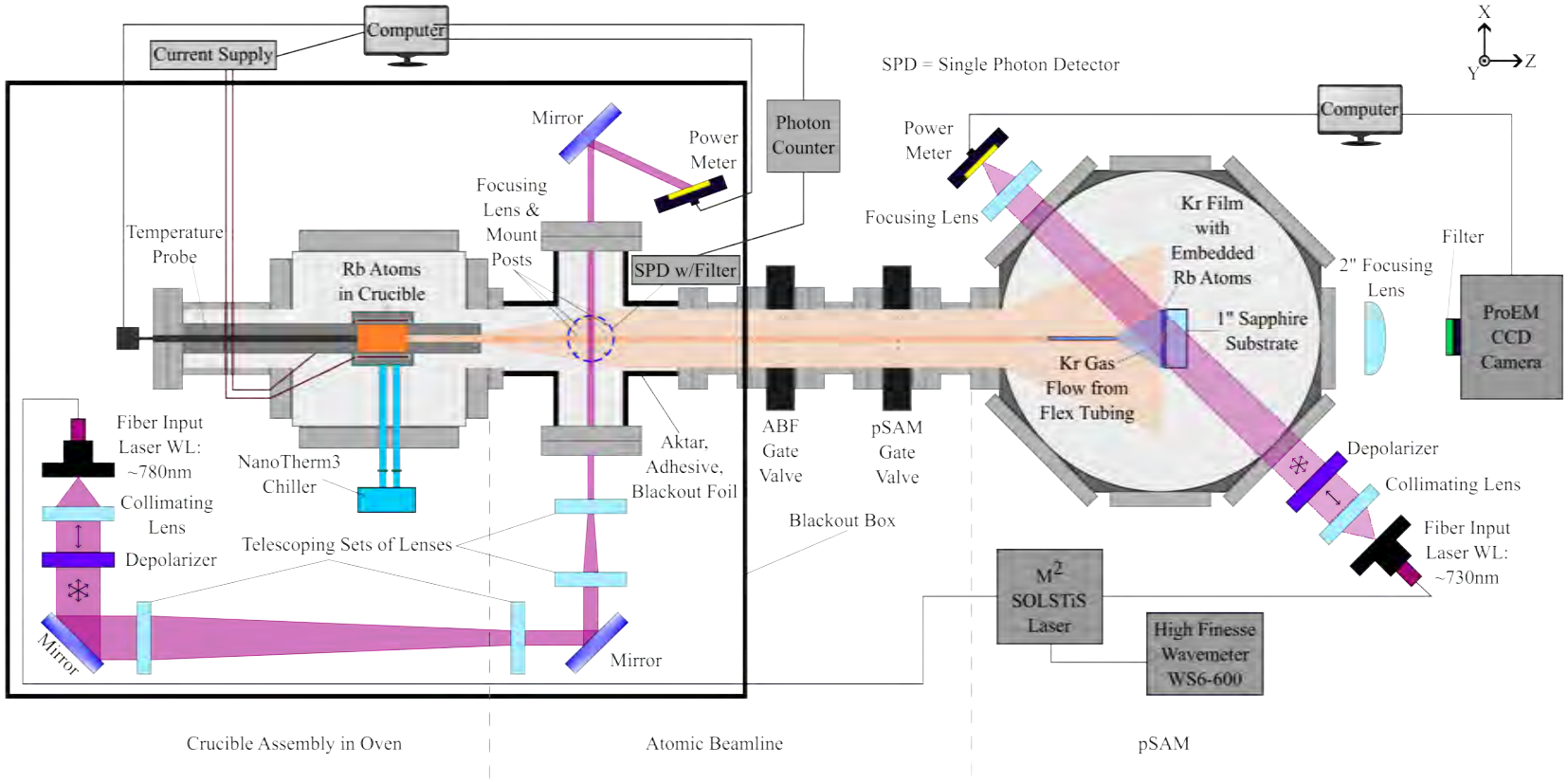

Figure 4.10: The total pathway and surrounding equipment from the oven to the film within the pSAM growth chamber.

models were used to calculate what were expected to be the upper and lower limits. As it turns out, the upper limit of a cosine distribution was less than the distribution model that fit the data better. Instead of a cosine distribution, it seemed an equal distribution across all angles was a better fit, referred to as a vapor cell model. In the vapor cell model it is treated more similar to a gas cloud of Rb atoms, which aligns with the conclusion that Rb liquid leaked out of the end of the nozzle before traveling as a vapor down the beamline. Additionally, on the lower limit end, a model from [SMG+98] was used, but it did not account for interatomic collisions. As an upgrade, now all simulations and calculations account for interatomic collisions through the use of a more complex model for the angular distribution.

4.2 Measurement Overview

Once again, the goal of the SAM project is to measure rare, low-yield nuclear reactions by counting the product atoms captured in a solid, noble gas film. Determining the cross section of a nuclear reaction with this method requires the ability to singly count the product atoms that get embedded into a film. "Counting" the atoms requires the brightness of atoms in medium to be calibrated via the measurement of fluorescence of a known number of implanted atoms.

In an experiment, rare nuclear reactions of interest are expected to only produce around five atoms per day, which could make it easier to spot isolated atoms in a film. However, for calibrating in-medium fluorescence (IMF), an accelerated beamline is not used. Instead, an atomic "beamline" is created through the effusion of a vapor out of the oven nozzle. These atoms travel down the system and then co-deposit with noble gas atoms creating a "doped" film. An IMF measurement uses a laser incident on the doped film to induce fluorescence

which is recorded by a charge-coupled device (CCD). Since the number of atoms implanted needs to be known for a calibrated measurement, an accurate model of the number and angular distribution of atoms effusing out of the nozzle must be determined. Spectroscopy of the atomic beamline fluorescence (ABF) in vacuum from a laser scan over a range of frequencies aids in determining the number of atoms coming out of the oven and their spread. Using both theoretical models and experimental data to evaluate the angular distribution of the atoms coming out of the nozzle of the oven, the number of atoms captured in a film can be determined. With a known number of atoms in a doped film, the fluorescence measured can be used to calculate the brightness of a single atom in medium. For an accurate calibration, varied amounts of atoms should be implanted in the film. If a linear relationship between the number of atoms and the recorded brightness emerges, then the brightness of an individual atom can be extrapolated.

For single atom detection to be achieved, it is necessary to know how many photons a single product atom produces while embedded in a noble gas solid. Uncovering that number in the form of the fluorescence cross section requires us to know three pieces of information during calibration experiments: how many atoms are embedded in the film, how many of their photons are being recorded, and what portion of counts recorded are solely attributable to the embedded product atoms.

The first of those questions—how many atoms are embedded in the film—is the most complicated to determine, as it is necessary to work backwards to answer it. To know how many atoms are embedded in the film, the number of atoms that effuse out of the oven within the atomic beamline portion of the setup and their angular distribution must be resolved. Phase one in the calibration experimental setup, illustrated by Figure 4.11, is the atomic beamline fluorescence (ABF) measurement. In this measurement, the laser-induced

fluorescence (LIF) at the intersection of the laser and atomic beams is recorded. The laser is scanned over a short range of frequencies to produce a spectrum which allows the number of atoms and their angular distribution to be deduced. Details of the ABF results are in Section 4.3.1.

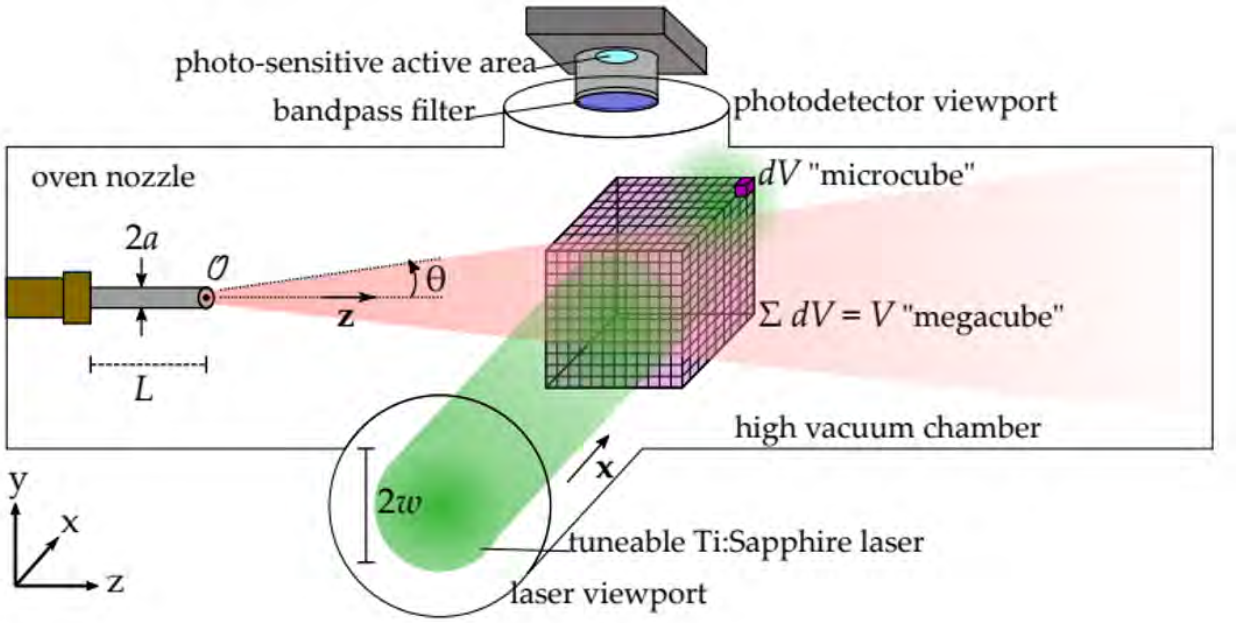

Figure 4.11: A cartoon depiction (not to scale) by R. Ready of the atomic beam and laser beam interaction within the 6-way cross on the ABF. The red triangular region represents the cone-shaped atomic beam effusing from the oven's nozzle at the left. The green cylinder represents the laser beam which intersects the atomic beam. At the intersection, a pink "megacube" comprised of smaller, individual "microcubes" can be used to summarize the nature of the laser beam and atomic beam interacting.

In phase two, the in-medium fluorescence (IMF) portion of the experiment was developed. This phase takes place within the pSAM growth chamber and the surrounding areas as it includes a charge-coupled device (CCD) camera. For an IMF measurement, a very thin noble gas film must be grown while product atoms are simultaneously co-deposited. Then, a laser is shone on the film and a portion of the photons is collected through a large lens that focuses them onto the CCD. Here, the geometry of the setup affects the second piece of

information needed—how many of the produced photons are being recorded. Adjustments in the physical setup could alter the solid angle factor if the distance between the film and the focusing lens leading to the CCD is changed. Figure 1.1 shows one possible geometry, but see Section 4.3.1 for details about the arrangement used currently. Accounting for the solid angle in calculations yields the total number of photons produced by the embedded product atoms. By doing so, no matter how the geometry changes, the calculation of the total number of photons emitted isotropically will remain the same.

Finally, phase three combines the previous phases for an asynchronous dual fluorescence (ADF) measurement. Just before the process of growing a doped film begins, an ABF measurement is taken to be used in analysis to determine the number of atoms traveling down the beamline path. Then a doped film is grown using the method outlined in section 4.3.1. After the film is fully deposited, then an IMF measurement ensues. With comparison to a calculated CCD image, the brightness of atoms in medium can be calibrated. Analysis takes into account the photon to count ratio of the CCD and all sources, external and internal, of background. Following this analysis, the fluorescence cross section and thus the photon emission rate for a single embedded atom can be determined.

4.2.1 Required Elements to Calculate the Fluorescence Cross Section

Experimentally, the variables needed to calculate the fluorescence cross section (FCS) can be summarized into six parts: laser intensity distribution and frequency, film growth rate, atomic beam (Rb in this case) flow rate, atomic beam angular distribution, geometric or solid angle factor, and CCD measurement. The fluorescence cross section is calculated using

variables connected to each of these categories.

The measurable two-dimensional distribution of the laser intensity corresponds to variable $I_{laser}(\vec{ra})$ in equation 4.1 from Section 4.1.1 and the recorded laser frequency used to excite the embedded Rb atoms is referenced as ν_γ. How fast the thickness of the noble gas film increases, the film growth rate, is determined empirically and represented by $\frac{dz(\vec{ra})}{dt}$. In the ABF portion of the experiment, both the atomic beam flow rate, written as $\frac{dN_a}{dt}$ in the FCS equation, and the atomic beam angular distribution, related to $j(\theta_a)$ and consequently K_{norm}, require measurements and analysis to be calculated. Comparing the measured ABF spectrum to a simulated spectrum reveals the atomic flow rate via the amplitudes of the spectral peaks and uncovers the angular distribution by matching the shapes of the spectra. A combined $\frac{j(\theta_a)}{\pi K_{norm}}$ gives literally the fraction of atoms per unit solid angle, which is subsequently multiplied by the solid angle factor given by the geometry of the experimental setup. A physical measurement from the film to the light-collecting lens between the film and CCD is elevated by code to account for the solid angle from each point in the film to each point on the lens. This results in a calculation in the form of a two-dimensional array with the summed solid angle over the lens for each bin of the film. In the FCS equation, this translates to $\int \frac{\hat{n_\ell}\dot(\vec{\ell}-\vec{ra})}{4\pi|\vec{\ell}-\vec{ra}|^3} dA_\ell$ and is dependent on the size and placement of the light-collecting lens relative to the film. Finally, the measurement from the CCD camera and its experimental parameters connect to V_{bin}, τ_{exp}, and $N_d(\vec{ra})$. Scaling the size of the CCD pixel to the film's approximated dimensions marks the volume of the film correlated to each pixel on the CCD, V_{bin}. An important setting to control on the CCD is the frame exposure time, τ_{exp}, which must be noted for an accurate calculation of the FCS. Lastly, as the CCD camera registers counts per pixel, the photon to count ratio specific to the model of CCD, and experimentally measured, is used to convert from counts per pixel to photons per pixel,

$N_d(\vec{ra})$.

In short, all of these factors are required elements to calculate the fluorescence cross section because they affect the number of photons per embedded atom that will be measured. Laser intensity affects the excitation-emission cycle of the implanted atoms. Typically, emission increases linearly as the excitation of atoms increases, but if the laser intensity gets too high, then that will no longer remain true. In any case, the number of photons that result will change with the intensity of the laser. As the film growth rate changes, so does the density of Rb atoms at any given point in the film. This in turn will affect the number of photons per atom measured across the film. In addition to affecting the Rb atom density over the film, the Rb atom flow rate and angular distribution from the oven nozzle also affect the overall number of atoms that get embedded in the film. Consequently of course, affecting the number of implanted atoms, alters the number of photons that will be emitted and measured. If the geometry of the experimental setup is modified, primarily concerning the distance from the film to the light-collecting lens that focuses onto the CCD, the solid angle factor will change and the calculation of the total photons assumed to emit isotropically will follow suit. Knowing what fraction of emitted photons are measured affects the calculation for the total number of photons emitted from the embedded atoms to find the photons emitted per atom in medium. Measurements from the CCD measure the number of photons emitted as directly as possible via counts. Naturally, the exposure time and portion of the film in frame will affect how many counts the CCD measures, especially given the assumption of point-to-point imaging from the film to the CCD camera. Not accurately recording or simulating any of these six factors could have a large impact on the calculation of the fluorescence cross section.

4.2.2 Laser Intensity Distribution

Laser intensity distribution across the film and substrate was investigated by taking a series of laser power scans on an un-doped, or empty, krypton film. Essentially, CCD images were collected to find an average frame for various laser wavelengths of interest over as wide a range of laser power possible. Each average frame was a composite of 100 CCD images. Laser wavelengths of 706, 721, 730, 743, and 757 nm were used as they correspond to peaks or troughs on the IMF signal recorded. The power range over all wavelengths was as low 0.002 mW with an upper limit of 20 mW. Note that the upper limit varied based on laser frequency. Additionally, scans were taken with the same conditions and parameters with the only exception being that the laser was shuttered. The other purpose for the laser power scans will be explained in Section **??**.

For the main laser wavelength of interest, 730 nm, the CCD images taken with a laser intensity set to 1 mW were averaged by pixel. These frames were chosen because they best matched the experimental settings from when the doped film data was collected. An average frame with the laser off was subtracted so that all counts included were only due to the laser. Pixels that were off the substrate were set to zero counts and the remaining total counts were used to make a ratio relating the measured laser power to total counts. Multiplying the average laser background CCD frame pixel-by-pixel by the average laser power per total counts resulted in a laser intensity distribution frame with the average power per pixel. This same frame was also used to create a laser power ratio array by dividing by the total power. This was done so that the frame can be multiplied by the exact power measured at the time of IMF measurements. Again, in terms of the FCS equation, this corresponds to the variable $I_{laser}(\vec{r_a})$, which is in units of W/m^2. Using the area of the film that corresponds to each

pixel converts the laser intensity in terms of power/pixel to power/area for the correct units.

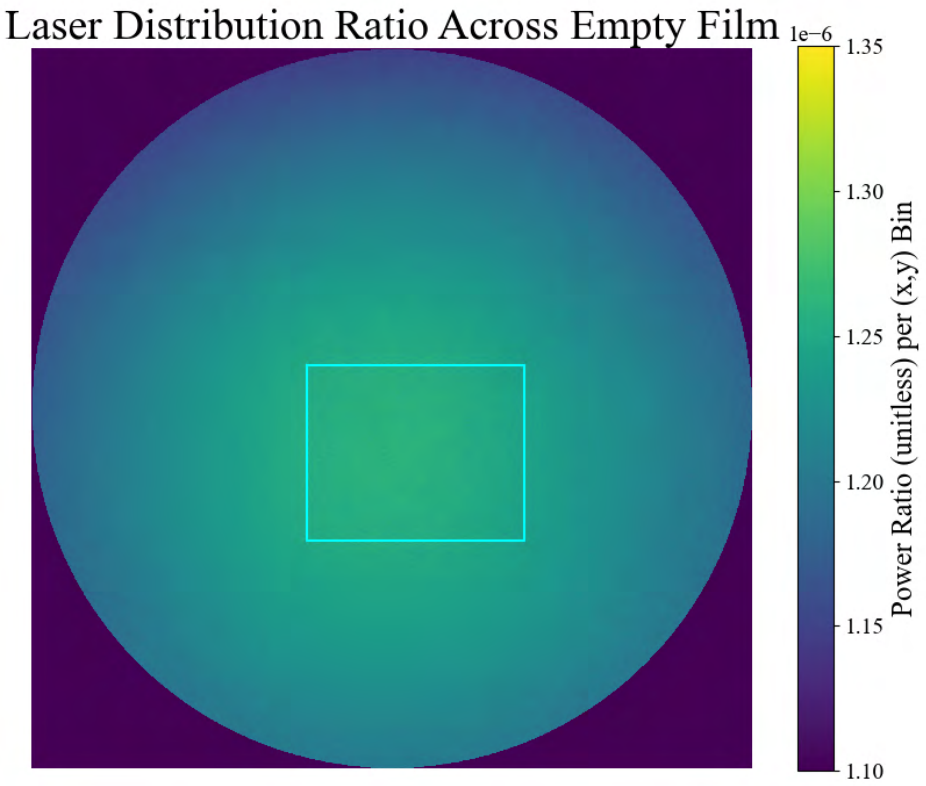

Figure 4.12: Here is an image of the spatial power ratio CCD frame. Multiplying this frame by the total laser power measured by the power meter gives the distribution of power per CCD pixel such that each pixel would have the power experienced within the correlating area of film. This can be used then to get the laser intensity per area of the film in units of W/cm^2. The rectangle outlines the ROI.

Additionally, the impact of the presence of the Kr atoms of the film on the laser background was examined. The overall normalized number of counts were approximately equal over the typical 700–760 nm laser scan range, so it can be concluded that the Kr film doesn't add or subtract laser background counts as recorded by the CCD.

In terms of a simple model used to describe all contributions to the counts measured by the CCD camera, described further in Section **??**, this relates to all terms aside from that pertaining to the embedded atom brightness. The simple model includes terms $b(P)t$, ct, and d for the laser background, non-laser background, and the intrinsic CCD background.

All of these counts will be included in the raw image taken of the un-doped Kr film. The adjusted frame that is the laser intensity per pixel would only include $b(P)t$, where t is the CCD exposure time—labeled in the FCS as τ_{exp}—and $b(P)$ is the laser power per second. The frame without the laser turned on would include both ct and d, the time-dependent background counts and intrinsic CCD background counts respectively.

A separate measurement was taken to find the photon to count ratio for the CCD camera, in which a known amount of light, and therefore a known number of photons, was incident onto the sensor of the CCD camera. A ratio of 5.2 photons/count was found, meaning that it takes an average 5.2 photons to elicit one count on the camera. This ratio can be used to convert between CCD counts and photons. It is important in extrapolating the number of photons a single atom produces when embedded in a solid based on the counts that the CCD is recording. Note that this value is also wavelength dependent. An assumption was made that most photons emitted from the embedded Rb atoms have a wavelength of 923 nm based on measurements from another experiment [GSM12]. For that reason, this measurement used 923 nm incident light. As the photon to count ratio does not drastically change over the range of wavelengths expected from emitted photons, it is a reasonable approximation to assume that the same photon to count ratio can be used to convert all recorded counts into photons. In the FCS equation, this converts the CCD counts per pixel to usable photons per pixel, $N_d(\vec{r_a})$

4.2.3 Film Growth Rate for IMF

For more details about the general film growth process, see Section 3.2. Films grown for IMF measurements are done differently in two ways. First, the film is much thinner, at only about 5 μm instead of the typical 100 μm. Secondly, there are atoms embedded in the

noble gas film following the "oreo method" described in Section 4.3.1. The target doped film growth rate is 5 μm/hr. For reasons currently unclear, faster growth rates, such as those used for 100 μm films, do not seem to show an IMF signal. This is represented in the FCS equation by variable $\frac{dz(\vec{ra})}{dt}$ and should be in SI units of m/s.

The final thickness of the film is then used in conjunction with the film area that corresponds to a CCD pixel to find the volume of the film per pixel, noted in the FCS as V_{bin} in this thesis and congruent to V_{voxel} in [Sin23].

4.2.4 Atom Beam Rate

Finding the atomic beam rate out of the nozzle relies on the ABF data. Atomic beamline fluorescence measurements take place in vacuum and are important for establishing how many atoms embed within the noble gas film. As the atomic beam of Rb effuses from the oven and travels down the ABF system, the laser beam intersects it perpendicularly, and the fluorescence from the interaction is measured on an axis orthogonal to both the atomic beam and incident laser. A lens is used within the ABF setup to focus the fluorescence from the atom-laser interaction onto a detector. More details of the ABF experiment and data collection are shared in Section 4.3.2. The measured emission spectrum is then analyzed to find the atomic beam rate based on the amplitude of the peaks. More details about calculating the atomic beam flow rate can be found in [Sin23].

Adjusting the parameters for a simulated spectrum until it matches the experimentally observed shape and magnitude of the fluorescence spectrum reveals information about the atomic beam rate and the angular distribution of atoms exiting the oven nozzle. With the time over which the spectrum is measured and the amplitude of the spectrum peaks, the atomic beam flow rate can be determined. It is written in the FCS equation as $\frac{dN_a}{dt}$,

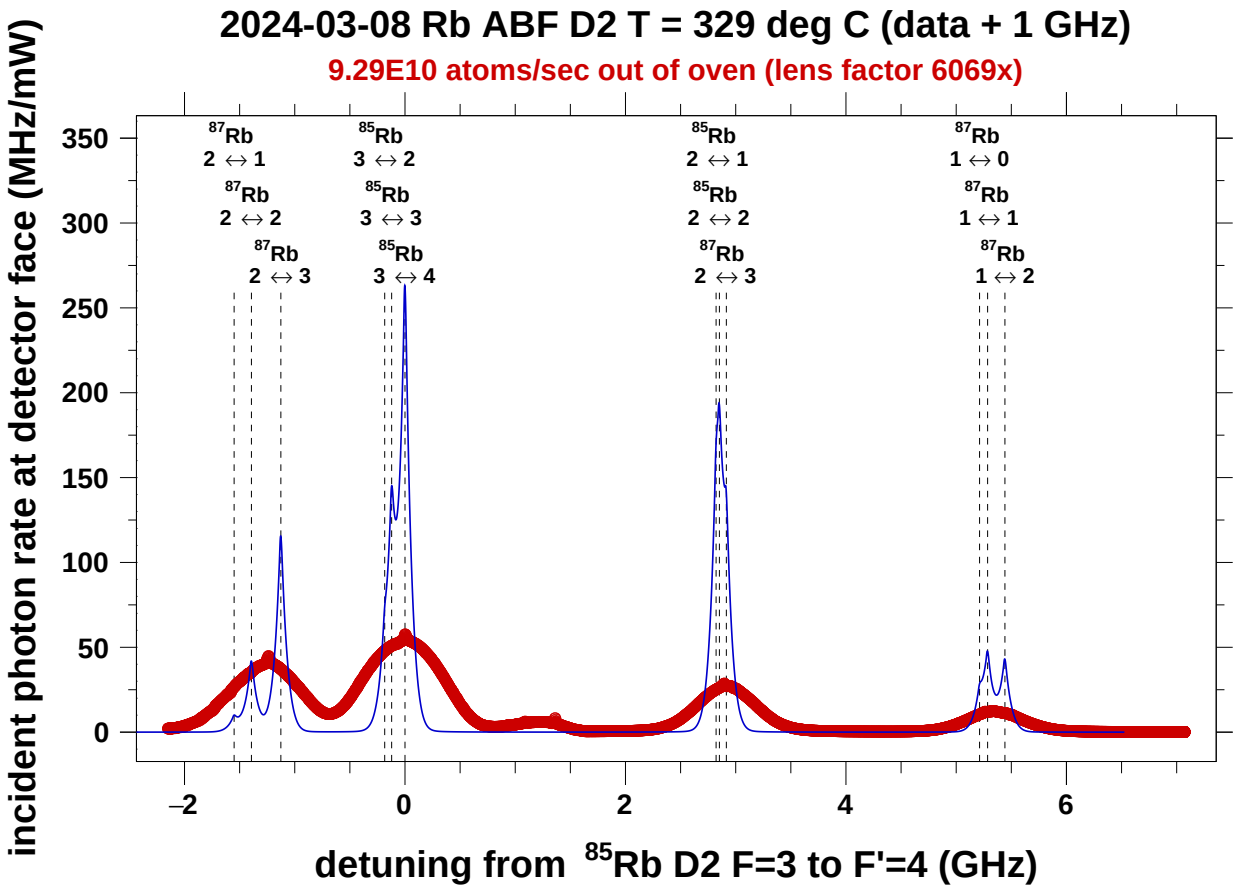

Figure 4.13: This image shows the measured and simulated spectra. The data is from 03/08/2024 when an IMF signal was observed. Due to the high oven temperature there is severe Doppler broadening in the measured peaks. There is also an unidentified extra peak at 1.25 GHz, that had been theorized to be a Rb dimer, but is assumed to be a result of the high oven temperature as well since it did not appear in previous ABF measurements. Comparing the simulated spectrum to the measured one yielded a calculated atom flow rate of 9.29E10 atoms/s.

using units of atoms/s. As seen in Figure 4.13, the calculated atom beam rate was 9.29E10 atoms/s.

4.2.5 Atomic Beam Angular Distribution

In the FCS equation, the angular distribution of the atomic beam is simply $j(\theta_a)$, despite encompassing a complex equation come to be known in the research group as the "big, ugly

equation". This variable also affects K_{norm}, and these variables appear together as a unitless fraction of atoms per unit solid angle $\frac{j(\theta_a)}{\pi K_{norm}}$ in the equation.

Modeling the angular distribution of the atoms effusing out of the oven via a long nozzle included accommodations for an intermediate flow regime in which atoms are assumed to bounce off of each other. Previously, a molecular flow regime was used to theorize the angular distribution of atoms exiting the nozzle. This model is based only on the geometry of the nozzle, with an assumption that there are no or very infrequent interatomic collisions [OK70] [FW22]. As such, it accounts for atoms that pass from the oven to the nozzle exit without any collisions between atoms nor between the atoms and the nozzle interior walls and it accounts for any atoms that do collide with the nozzle interior walls but don't stick. Moving into the intermediate flow regime, this model additionally includes considerations for atoms that collide with each other.

Updating to the intermediate flow regime is a notable upgrade as the collisions between atoms are theorized to be comparable in significance to that of the collisions between atoms and the nozzle walls for this experimental setup. When the mean free path, λ_ℓ, is on the same order of magnitude as the length of the nozzle, as is the case in this experiment, interatomic collisions within the nozzle can no longer be ignored [OK70]. In terms used in the equations below, if the Knudsen number, K_{n_ℓ} and detailed below in equation 4.4, is between γ and 10, then atom-atom collisions become more prevalent and cause a broader angular distribution. While the magnitude of the flow out of the nozzle may still be accurately described by the former molecular flow regime, depending on the pressure, the angular distribution out of the nozzle cannot be described without accounting for atom-atom collisions [OK70]. Therefore, utilizing this regime is important for the calibration process and the ability to accurately measure the brightness of embedded Rb atoms in a Kr film.

$$K_{n_\ell} = \frac{\lambda_\ell}{L} \tag{4.4}$$

$$\tag{4.5}$$

Across the literature, there are some slight, though significant, discrepancies in the equation used for calculating the angular distribution of an intermediate flow regime. After testing different combinations of the alterations, equation 4.10 below was converged on and cross-checked by matching the resultant plot with that included in G. Scoles *Atomic and Molecular Beam Methods Volume I* [SMG+98]. This equation, and this regime, is used to describe the angular distribution of atoms effusing from the end of a long nozzle. A long nozzle is any nozzle for which the aspect ratio, γ given in equation 4.6, is less than one or in other terms, in which the diameter of the nozzle exit is less than the length of the nozzle.

$$\gamma = \frac{2a}{L} \tag{4.6}$$

$$\tag{4.7}$$

In this regime, number density plays an important role in determining the interatomic collision rate. The ratios of the number densities at the exit and entrance of the nozzle channel to the number density within the oven are given as ξ_0 and ξ_1. These values are similar to the atom-wall collision rates at the respective exit and entrance of the nozzle channel, given by ζ_0 and ζ_1, and thus can be approximated such that:

$$\xi_0 = \zeta_0 \tag{4.8}$$

$$\xi_1 = \zeta_1 \tag{4.9}$$

Following the above approximations and the tested and confirmed corrections, the angular distribution for an atomic species ℓ can be explained with:

$$j_{\mathcal{I},\ell}(\theta) = \begin{cases} \xi_0 + \dfrac{\sqrt{\pi}}{2}\xi_0 \dfrac{e^{\delta^2}}{\delta}\Big(\operatorname{erf}\xi - \operatorname{erf}\delta\Big) + (1-\xi_1)e^{-\left(\xi^2-\delta^2\right)}, & \theta = 0 \\ \xi_0\cos\theta\left\{1 + \dfrac{2}{\sqrt{\pi}}\dfrac{e^{\delta'^2}}{\delta'}\left[\dfrac{R(p)}{2}\Big(\operatorname{erf}\xi' - \operatorname{erf}\delta' + F(\xi_0,\xi_1,\delta')\Big) + S(p)\right]\right\}, & \gamma \geq \tan\theta \\ \xi_0\cos\theta\left[1 + \dfrac{2}{\sqrt{\pi}}\dfrac{e^{\delta'^2}}{\delta'}S(1)\right], & \gamma \leq \tan\theta \end{cases} \tag{4.10}$$

where the following substitutions were made:

$$\delta = \sqrt{\frac{\xi_0^2}{2Kn_\ell(\xi_1 - \xi_0)}} \quad , \quad \xi = \left(\frac{\xi_1}{\xi_0}\right)\delta \tag{4.11}$$

$$\delta' = \sqrt{\frac{\delta^2}{\cos\theta}} \quad , \quad \xi' = \left(\frac{\xi_1}{\xi_0}\right)\delta' \tag{4.12}$$

$$F(\xi_0,\xi_1,\delta') = \frac{2}{\sqrt{\pi}}\xi'\left(\frac{1}{\xi_1} - 1\right)e^{-\xi'^2} \tag{4.13}$$

$$S(p) = \int_0^p \mathrm{d}z\sqrt{1-z^2}\left\{\operatorname{erf}\left[\delta'\left(1 + \frac{z}{p}\left(\frac{\xi_1}{\xi_0} - 1\right)\right)\right] - \operatorname{erf}\delta'\right\} \tag{4.14}$$

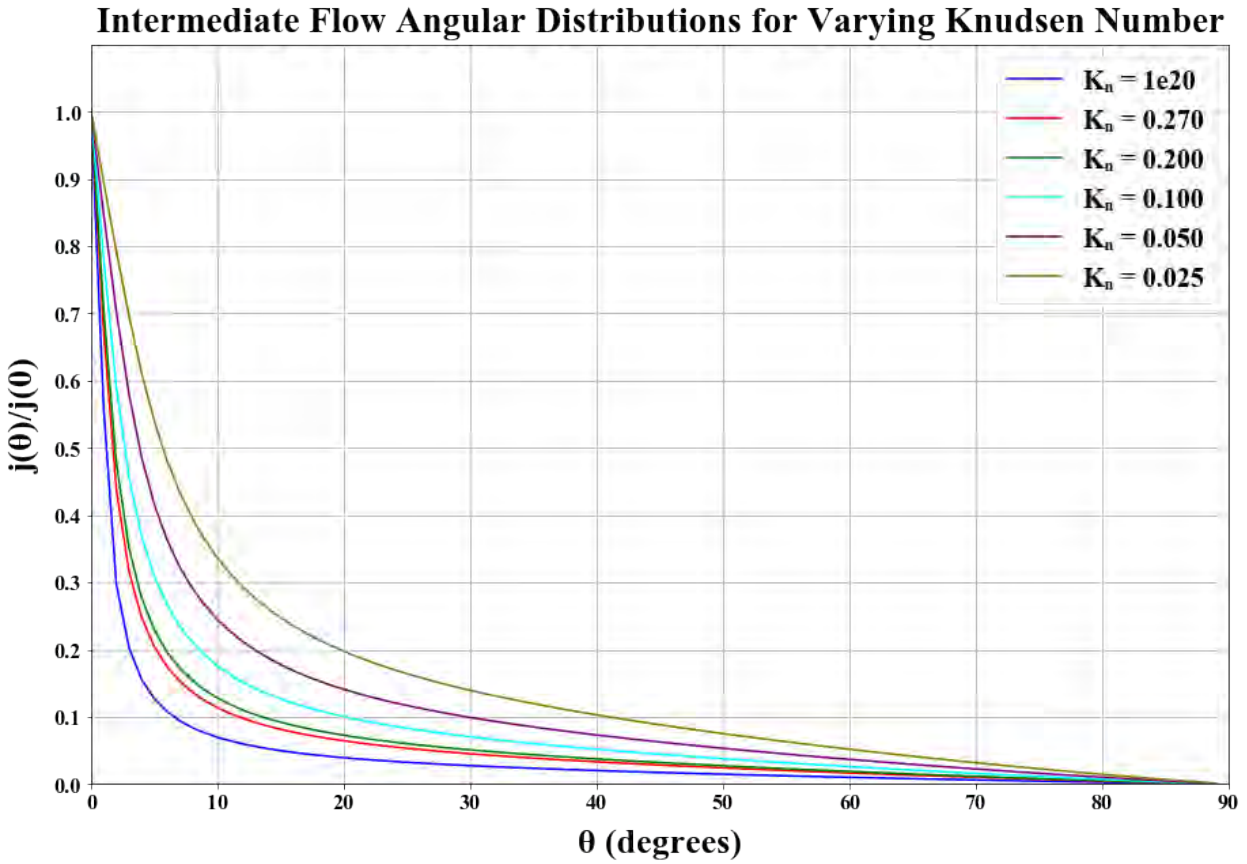

Figure 4.14: Intermediate flow regime angular distributions at varying Knudsen numbers K_n with an aspect ratio $\gamma = 0.024$. This ratio is what will be used for the Single Atom Microscope (SAM) project which utilizes a long nozzle of about 8.3cm long (variable L) and a radius of about 0.1cm (variable a). θ is in degrees. Note that each distribution has been normalized to its center-line intensity $j_{\mathcal{I}}(0)$. Also note that K_n = 1e20 has been used to approximate infinity.

From here, the atom flow rate and the angular distribution can be used in further computational modeling to determine how many atoms embed within the film. The modeled atomic distribution is described and illustrated in Section 4.4.3

4.2.6 Solid Angle Factor for IMF

When the laser is incident on the embedded atoms in the film, the photons are assumed to fluoresce isotropically. This means that the photons recorded by the CCD camera are only a fraction of all emitted. To account for this, the solid angle factor is calculated based on

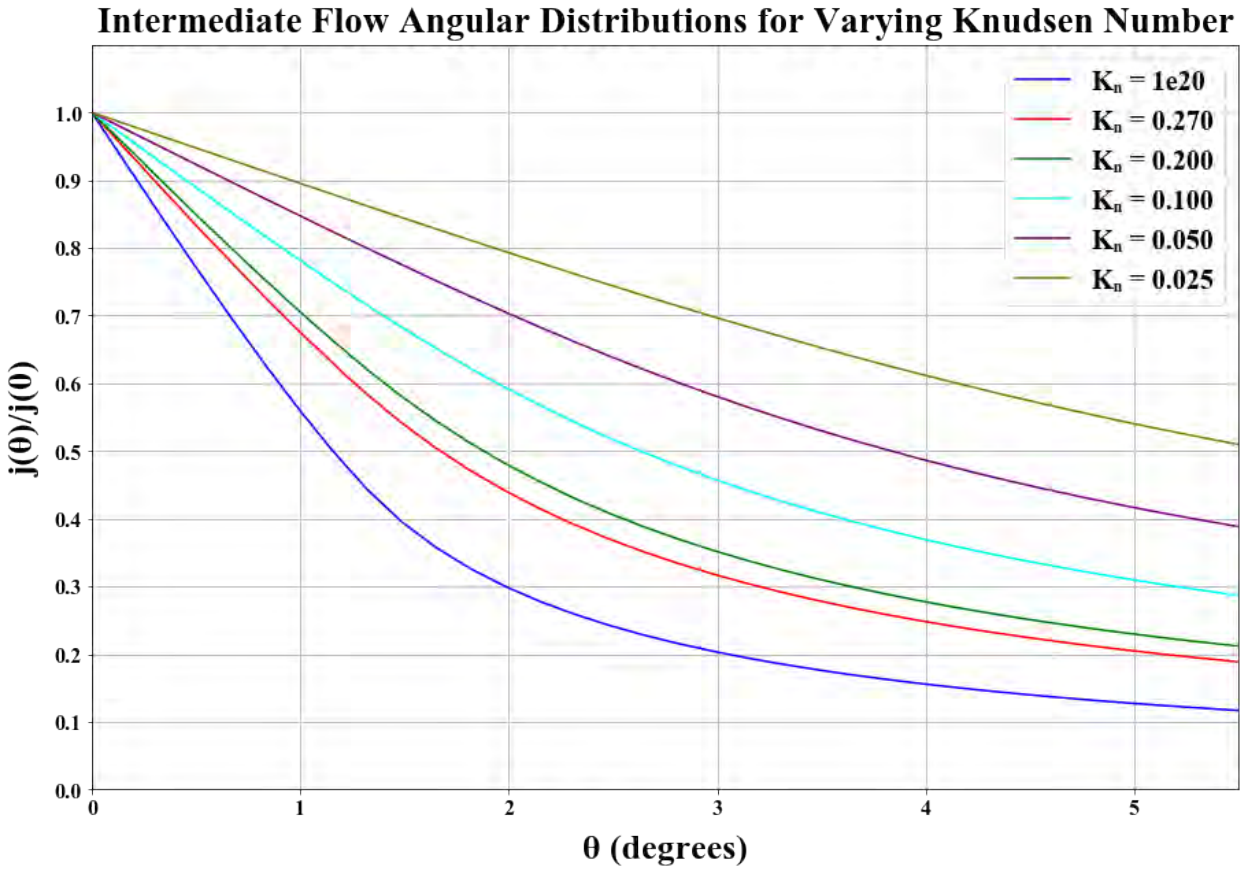

Figure 4.15: As in Figure 4.14,the intermediate flow regime angular distributions at varying Knudsen numbers K_n with an aspect ratio $\gamma = 0.024$ is shown, but this time focusing on small angles which are more pertinent to the experimental set-up. θ is in degrees. Note that each distribution has been normalized to its center-line intensity $j_{\mathcal{I}}(0)$. Also note that K_n = 1e20 has been used to approximate infinity.

the geometry of the experimental setup. In this case, the relevant physical measurements are the size of the film on the substrate, the size of the light-collecting lens, and the distance between the surfaces of the two. Summarily, the solid angle uses the fraction of the space that collects photons—the surface of the lens—over the entirety of the spherical space at that same radial distance—the distance from the film to the surface of the lens—to account for the photons emitted that do not get collected by the lens. When the number of photons recorded is divided by the solid angle factor, the result is the number of photons that are emitted in all directions.

In the FCS equation, the solid angle factor is given as $\int \frac{\hat{n_\ell}\dot{(}\vec{\ell}-\vec{ra})}{4\pi|\vec{\ell}-\vec{ra}|^3} dA_\ell$ and its units cancel out to overall be a unitless factor. In translating this for a computational model, accounting for the geometric factor is done with a summation of calculations method. The goal is to create a two-dimensional array full of solid angle (SA) values that can be used with the CCD image to account for the solid angle factor. Think of the film on the substrate in terms of an array of "bins" and the light-collecting lens in terms of an array of "squares". Approximate that all atoms in each bin are in the center of their bin. For one bin on the film, find the sum of the solid angle for each square on the lens. This means for every bin-square combination, calculate the solid angle between the two in the direction of the lens and the sum of contributions for all squares to one bin gets a factor value in the SA array for the corresponding film bin. Repeat this for each bin on the film. The result should be an array the same size as the film (atomic distribution) array with each array entry containing the value for the solid angle factor over the whole lens for the correlating film bin.

Calculating the solid angle between a single bin on the film and a single square on the lens is done by dividing the small area of the lens that a square represents by the surface area of the sphere that has a radius equal to the distance between the film bin and lens

square. Because the the lens used is flat on the side facing the film, the normal vector that should be included in this expression always points in the same direction along the negative z-axis. As far as the code is concerned, the normal vector will always be one and can therefore be ignored as long as a plano-convex lens is used. Finding the precise distance between a film bin and lens square requires mapping a coordinate system so that even if the number of bins or squares in play changes, the calculated distances will be correct. Changing the number of squares on the lens is done to either increase accuracy of the calculation by increasing the number of squares or to speed up the runtime by decreasing the number of squares. Testing different numbers of squares was done to provide a reasonable runtime without overtly compromising on the accuracy of the calculation. Changing the number of bins on the film would primarily be expected if the CCD was replaced with one that had a different number of pixels, though in theory the number of bins could also be altered for the same reasons as the lens squares. With the coordinate system in place, the locations of the film bin and lens square are used in conjunction with the orthogonal distance between the surfaces of the two to find the precise distance between the centers of bin and square through the (repeated) use of the Pythagorean Theorem.

Performing the calculation in this way assumes that, in addition to isotropic photon emissions, there is point to point imaging [Sin23]. Following this assumption means that from one bin at (x, y) on the film, all emitted photons that hit the lens will be focused onto (x, y) of the CCD camera. Following this, should all atoms in the film be centralized into one bin on the film, then multiplying by the SA array should result in only one non-zero element. In addition to this check, another was done to ensure the SA calculation's accuracy by comparing the SA array value corresponding to the bin at the center of the film to the calculation of the solid angle from the center of the film to the entirety of the lens. These

two values were less than 0.36 % different, proving the summation method accurate.

Conveniently, this SA array can be used with any IMF data collected, so long as the geometry of the setup between the film, lens, and CCD remains the same. Figure 4.16 shows the SA array given the experimental parameters when the IMF signal was recorded.

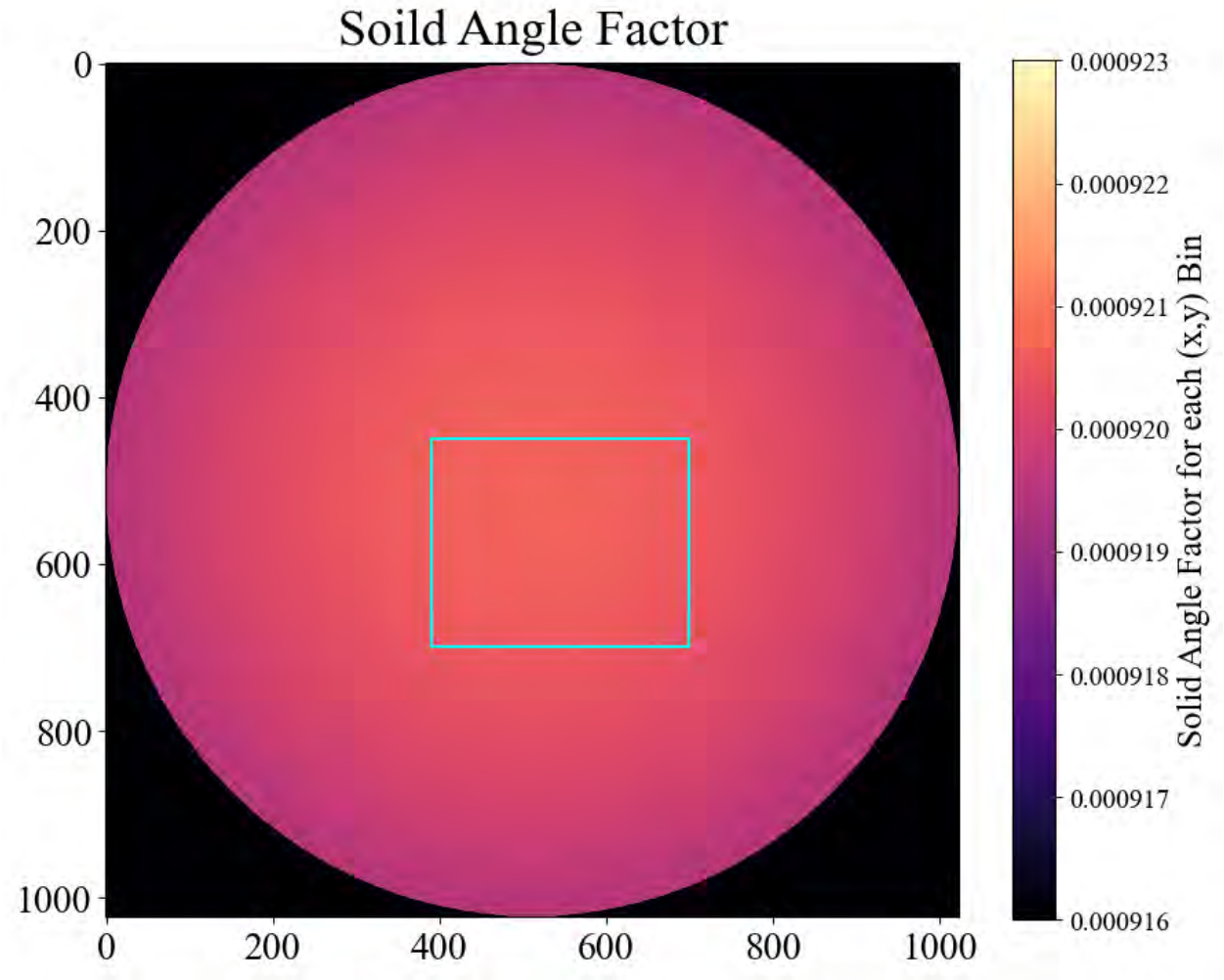

Figure 4.16: This image is the simulated solid angle given experimental setup parameters. The film is approximated to be the same size as the 1" (25.4 mm) substrate. The light-collecting lens is 2" (50.8 mm). The distance between the film and the lens is 0.4178 m. The aqua square outlines the region of interest in the film.

In terms of the simple model of Section **??**, the only thing to note is that to convert from the counts due solely to the N embedded atoms, written as $a(P)Nt$, to photons emitted in all directions, the overall solid angle will need to be used. Within this term, $a(P)$ is

the embedded atom brightness in units of photons/s/atom that the CCD records. It is dependent on the laser wavelength and power, in addition to time. Because this model is used to explain the number of counts that the CCD records, the atom brightness included in this model is only for the portion of fluorescence that the CCD measures. To find the overall atom brightness in terms of total emitted photons/s/atom, $a(P)$ needs to be divided by the solid angle.

4.3 Experimental Overview

4.3.1 Asynchronous Dual Fluorescence Experimental Setup

While the essence of the experiment has remained the same, several modifications were made as stated in Section 4.1.2.3. The physical experimental setup can be seen in Figure 4.10 for the asynchronous dual fluorescence (ADF) measurements. The ADF experiment consists of ABF and IMF measurements and calculations based on the geometry of the setup. This process is only needed for calibration experiments or other testing in which the in-lab pseudo-beamline is used that consists of atoms effusing out of the oven.

Summarized steps of the ADF experiment include three main parts. First, the prep work needs to be done, making sure that all equipment is installed correctly and set to the proper parameters. This means that the ABF and pSAM side of the experiment line are all under high vacuum and isolated from each other by having a pneumatic gate between the two sides closed. A tank of the noble gas of choice should be connected to the gas-handling system (GHS) and the GHS should be pressurized and ready for a film growth. Within pSAM, the substrate should be visually inspected to confirm it is clean and ready

for a film growth. The ABF system should have the sample of atoms for embedding already within the crucible within the oven and the oven should already be heated to the desired oven temperature by adjusting the current through the heating element. The laser should be warmed up and ready for use with the proper setup for the desired wavelength range to be used. Additionally, an ABF test measurement at a minimum should be taken to ensure that atoms are indeed effusing out of the oven. For simplicity, since krypton and rubidium were the respective noble gas and embedding atoms used for the data analyzed in this thesis, they will be the elements referenced throughout the rest of this section as the noble gas and embedding sample of choice.

Second, the doped film growth commences. The intended thickness is 5 μm and the target growth rate is 5 μm/hr. For reasons not yet fully understood, the typical thickness of 100 μm used for the standard noble gas film traps is not compatible with obtaining a signal, nor is a thin film with a faster growth rate. Initially, a layer of krypton only is deposited until a thickness of about one micron is achieved. Then, a layer of krypton and rubidium is deposited until a total thickness of about four microns is reached. Finally, to complete this "oreo method", one last layer of only krypton is deposited until the film reaches a thickness of five microns. The thickness of the film is monitored in real time with the interference pattern from a diode laser that transmits through the film as krypton and rubidium is deposited. The number of peaks correlates to a specific thickness, allowing the user to open and close the pneumatic gate at the appropriate time to attain the desired thicknesses of each layer. After the doped film growth is completed, all systems should be put into maintain or safe modes. This means that pSAM and the ABF side of the experiment line should be kept isolated from each other with the gate between them closed. The GHS should be isolated from pSAM and can undergo the procedure for after film growths in which it is pumped

down to remove the excess krypton and returned to a state of vacuum. The laser diode and photodiodes should be turned off. If a full ABF measurement was not taken, then that data should be collected immediately after the film growth is completed. Then, the current supply can be turned off so that the oven cools down. At this point, the ABF portion of data collection is complete and the focus shifts to the pSAM and IMF side.

Table 4.6: Film Growth Parameters

Stage Duration (min)	**Stage Pressure (Torr)**	**Flow Rate (l/s)**	**Ramp Up Rate (l/s)**
1	5	3.28E-6	2E-3
51.9	16	5.25E-6	2E-3

Table 4.7: The stages for Kr deposition of the film grown on 3/8/2024 that successfully exhibited an IMF signal. The gate valve to allow for Rb to be co-deposited was opened and closed based on the thin film transmission monitoring to ensure Rb was only deposited for the middle 3 of 5 total microns of the film, following the "oreo" method.

Third, and last in the three main portions of this experiment, the IMF data needs to be collected. At this stage, a Rb-doped Kr film has been grown with the proper parameters to allow for a signal to be observed with laser-induced fluorescence. The laser should already be warmed up and prepared from the ABF scan, but the CCD camera needs to be on and cooled down to -55C for a half hour to be stable and ready to take measurements. The micro-ion pressure gauge (MIG) on pSAM needs to be turned off so that the light from it does not over-expose the CCD image. IMF data should be collected via the CCD camera for the entirety of a laser scan, explained further below.

After the experiment is conducted to collect the ABF and IMF data surrounding the Rb-doped Kr film, analysis is performed to extrapolate the brightness of implanted Rb atoms in solid Kr in the form of the fluorescence cross section.

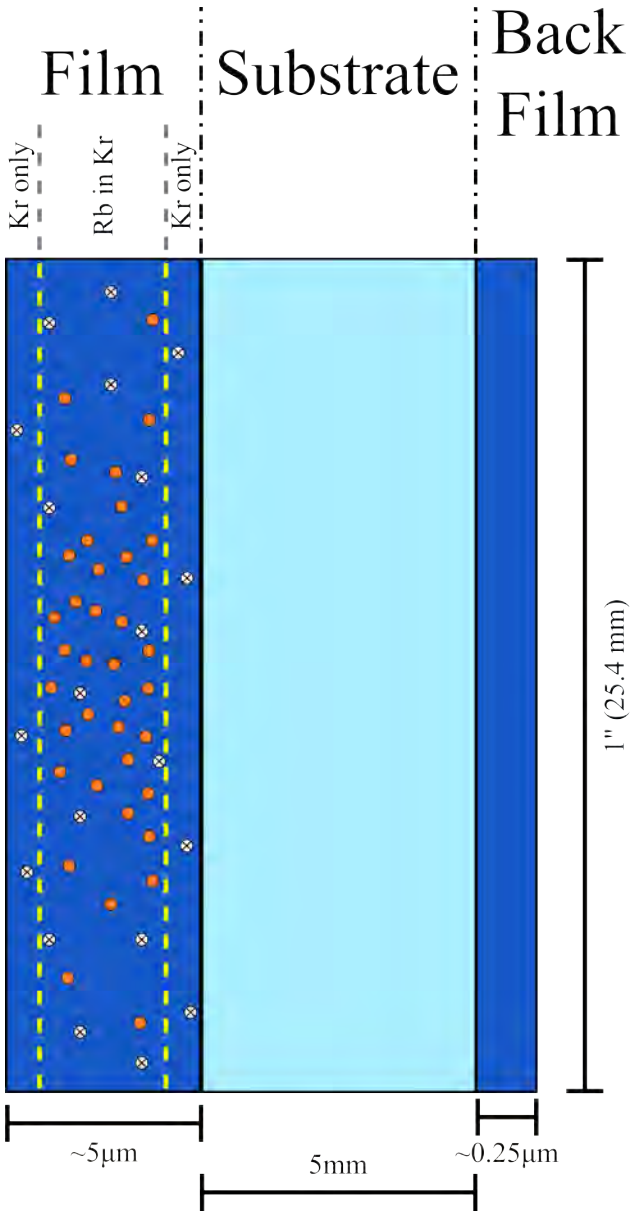

Figure 4.17: This illustrates the product film for calibration studies, grown in the described "oreo" method of depositing layers of Kr only, then Rb and Kr simultaneously, and lastly Kr only again. The light blue rectangle represents the sapphire substrate; the dark blue rectangles depict Kr film; the orange circles are Rb atoms; and the white circles with an "x" inside portray "bubbles" of vacuum pockets within the film. The back film thickness is estimated to be proportional to the back film grown during a standard film growth—a 100 μm film will have a 5 μm thick back film.

4.3.2 ABF Experimental Parameters

ABF data should be collected either directly before or immediately after the film growth. In an ideal case, the data would be collected in both scenarios, compared, and if notably different, extrapolated to mirror what the data would look like during the actual film growth. As long as the oven temperature is stable though, the ABF data should be consistent whether taken before or after the film growth occurs.

For the ABF data collection, the laser is warmed up for at least an hour, as recommended for power and frequency stability. The single photon detector (SPD) is situated orthogonally to the intersection of the atomic beam effusing from the oven nozzle and the laser. A small lens within the high-vacuum system between the atom-laser intersection and the SPD enhances the signal. Various lenses are in place to increase the laser beam profile for effective use of the depolarizer and to then reduce the laser beam profile to approximately 1-2 mm and collimate it before the laser enters the 6-way cross of the ABF system. Two mirrors manipulate the pathway to be spatially efficient as well as offering the capability for total control over the laser beam orientation through the 6-way cross. After passing through the ABF system, the laser hits another mirror which is oriented to reduce any reflections back towards the system and thus reduce any background recorded by the SPD. Finally the laser ends at a power meter which records constantly during the ABF measurement. Parameters for ABF data collection are found in Table 4.8 and the optical equipment is listed in Table 4.9.

Table 4.8: ABF Settings for Full Rb-85 & Rb-87 Spectrum Scan, 780 nm

Oven Settings	
Current Supply Mode	Constant Current (CC)
Resistor Current	3.5 A
Oven Temperature	325.3 C
Laser Scan Parameters	
Scan Start	780.2499 nm
Scan Stop	780.2316 nm
Scan Center	780.2407 nm
Scan Width	9 GHz
Scan Rate	10 MHz/s
Output PD	0.841 V

Table 4.9: ABF Equipment & Optics

Optics (Pathway Order)	
Collimating Lens	LB1901-B, f = 75 mm
Depolarizer	DPP25-B
Mirror	PF10-03-P01
Telescoping Lens	LA1461-B, f = 250 mm
Telescoping Lens	LC1715-B, f = -50 mm
Mirror	PF10-03-P01
Telescoping Lens	LA1509-B, f = 100 mm
Telescoping Lens	LC1715-B, f = -50 mm
Mirror	PF10-03-P01
ABF Equipment	
Single Photon Detector	SPDMA 350–1100 nm 500 μm Active Area
Photodiode Power Sensor	S120VC, 200–1100 nm, 50 nW – 50 mW
Power Meter Display	PM100A

4.3.3 IMF Experimental Parameters

After the film is grown and ABF data has been collected, the IMF data can in theory be collected any time within a reasonable time window. Ideally, laser-induced fluorescence is measured immediately, but since the film can maintain its optical integrity for a few days up to even a few weeks, there is ample time for testing. What is considered a reasonable time window will vary based on the decay of the transmission of the film. When a film has a high transmission ratio, that ratio usually stays within 10% for about three days. After

that point, it may reduce gradually. However, with the much thinner films grown in the IMF preparation phase and for the experiment that yielded the usable data discussed in this thesis, the transmission ratio of the film was lower. It's unclear what caused this, but the film was so thin that it didn't seem to affect the measurements. Also, because the transmission through the film was at a lower rate than was typical for the thicker films, the transmission remained the same much longer.

For IMF data collection, there are two optical pathways to consider. First, there is the laser pathway. Utilizing similar optics from the ABF setup, a collimating lens is placed after the laser exits the fiber coupling. Next, the laser passes through a depolarizer before entering the pSAM growth chamber via the anti-reflection coated viewport, transmitting through the substrate and film, and then exiting the pSAM growth chamber via another anti-relection coated viewport. Finally, the laser hits a focusing lens to reduce the size of the laser beam before it ends its path on a power sensor. The other optical pathway to consider is that of the fluorescence from the embedded rubidium atoms in the krypton film. The fluorescence is theorized to isotropically emit, with the photons of focus being those that are collected by the large lens facing the film and substrate. This light-collecting lens focuses the image of the film onto the CCD camera with an assumed one-to-one imaging from the film to the CCD pixels described previously. Between the lens and the CCD is a filter that blocks that majority of light below 844 nm. Since the peak emission wavelength of embedded rubidium atoms has been measured to be 923 nm [GSM12] with a full-width half-max (FWHM) of 37 nm, this filter prevents the majority of any reflected laser light from hitting the CCD without negatively affecting the signal reading from the fluorescence. Previously, this experiment had been done with a different geometry and the use of a dichroic beamsplitter. With the new geometry employed for this set of data collection, the dichroic beamsplitter seemed to hinder

the signal on the same order as it reduced the laser background, making it purposeless to include.

During the IMF measurements, some data was taken with the laser stationary at a single wavelength and some data was taken with the laser scanning over a full range of wavelengths. Scanning the laser enabled the collection of a data to compile a full fluorescence spectrum based on the excitation wavelength of the laser. Stationary laser scans were used most for laser power scanning. Laser power scans (LPS) were taken with the doped film and with an empty, un-doped, krypton film. Laser and CCD parameters for IMF data collection can be found in Table 4.10; laser and CCD parameters for LPS can be found in Table 4.11; and the optics used for the laser and fluorescence pathways can be found in Table 4.12.

Table 4.10: IMF Settings for Rb-Doped Kr Film on 03/08/2024

CCD Settings	
Exposure Time	0.8 s
Frames/Exposure	1
Laser Scan Parameters	
Scan Start	760.000 nm
Scan Stop	700.000 nm
Scan Rate	20 GHz/s
Output PD	0.779 V

Note that a scan rate within a range of 20–50 GHz/s is sufficient. Additionally, expect a large file output as it may require 2200 frames to complete the scan depending on the scan rate.

4.4 Analysis

4.4.1 Analysis Overview

Determining the number of photons emitted from a single atom embedded in a noble gas film requires an understanding of the number and angular distribution of atoms effusing from

Table 4.11: ABF Settings for Full Rb-85 & Rb-87 Spectrum Scan, 780 nm

Oven Settings	
Current Supply Mode	Constant Current (CC)
Resistor Current	3.5 A
Oven Temperature	325.3 C
Laser Scan Parameters	
Scan Start	780.2499 nm
Scan Stop	780.2316 nm
Scan Center	780.2407 nm
Scan Width	9GHz
Scan Rate	10 MHz/s
Output PD	0.841 V

Table 4.12: IMF Equipment & Optics

Optics (Laser Pathway Order)	
Collimating Lens	LB1901-B, f = 75 mm
Depolarizer	DPP25-B
Focusing Lens	LA1461-B, f = 250 mm
Optics (Fluorescence Pathway Order)	
Light-Collecting Lens	LA1145-B, 2", f = 75 mm
830 nm Long-Pass Edge Filter	BLP01-830R-25
(Optional) Dichroic Beamsplitter	Di02-R830-25x36
ABF Equipment	
Charged-Coupled Device	Teledyne PROHS-1024BX3
Photodiode Power Sensor	S120VC, 200–1100 nm, 50 nW – 50 mW
Power Meter Display	PM100A

Note that the part number for the long-pass edge filter is from when it was bought from the company Semrock. The company is now IDEX, with the filter having a new part number of FL-008550. Similarly, the dichroic beamsplitter now has a part number of FL-007138.

the oven nozzle such that the fraction that gets implanted in the film can be calculated. This requires calibrated measurements of the atomic beam fluorescence (ABF) in vacuum to complement the in-medium fluorescence (IMF) measurements of a doped film. In both cases, the solid angle of the detector from the laser-atom interaction region, laser shape, isotropicity of the fluorescence, and any optical limitations must be taken into account. Additionally, in ABF measurements the atomic beam shape needs to be considered and in IMF measurements

any atom or laser behavioral changes due to the medium should be acknowledged.

Several assumptions are made about both the experimental setup and the physical theory for the calculations of the number of atoms embedded in the film and consequently the fluorescence cross section. Pertaining to both the ABF and IMF setups, it is assumed that the photons from the interaction of the rubidium atoms and the laser emit isotropically. Further, it is assumed that the laser is evenly depolarized before interacting with the rubidium atoms in both the ABF and IMF experiments. The final assumption that applies to both setups, or rather the full length of the experimental pathway from ABF oven to pSAM growth chamber, is that any atoms that collide with the metal confines of the pathway stick to the sides instead of bouncing throughout the apparatus. The only exception to this is when atoms within the nozzle diffusely re-emit, as accounted for in equation 4.10 [OK70].

In the ABF setup, there is a focusing lens between the photon detector and the interaction region of the atomic beam with the laser beam. Because the lens has to be placed on the inside of the setup which is in vacuum, there is no way currently to adjust the lens without dismantling the setup. As such, it is assumed that the lens is accurately placed for each measurement. Additionally, all atoms effusing from the oven are expected to be rubidium only. While various isotopes of rubidium are expected and observed, molecules such as rubidium oxide (RbO) are not considered. However, this expectation is supported by the data, as there are no consistencies that suggest their presence.

In the IMF setup, the atomic distribution of rubidium within the film is presumed to be a centered, smooth, and radial gradient. The laser is estimated with reasonable certainty to cover the entirety of the film and substrate. This means that all embedded atoms should be excited by the laser without any additional laser light reflecting off the interior of pSAM. Photons recorded by the CCD were all assumed to be approximately at the peak emission

wavelength of 923 nm. Lastly, calculations were conducted under the premise that the film clarity being lower than normal would not affect the photon production or counts recorded by the CCD.

A summary of all major and relevant ABF data collected for these calibration studies is in Table 4.13. Note that the laser wavelength used to excite the atoms in vacuum, λ_{las} is typically given as a range. The laser scans from the higher wavelength to the lower one. In the last column of this table, the yes/no indicates if an ABF signal was observed and if a film was grown with some amount of atoms embedded. If there was a film grown, then Table 4.14 should be referenced to see additional information.

Notice that the first entry in Table 4.13 involves ytterbium. While this is not directly relevant to the calibration studies of Rb atoms implanted in Kr films, Yb was the first source material used in fine-tuning the ABF setup. This was done because Yb is much safer and easier to handle than Rb, which can have a volatile reaction with oxygen. The Yb atoms were put into the oven as a solid whereas Rb needed to be loaded in as a liquid. Testing with the Yb also allowed for the ABF optical setup to be prepared and tested. The full spectra of interest of Yb atoms in vacuum was able to be observed during the Yb ABF experiments. While a couple of attempts were made to embed Yb into Kr films, it was learned after these failed attempts that absorption was not observed with thick films (100 μm) grown at the normal deposition temperatures (34 K for Kr films).

Table 4.13: ABF Data Collection Summary

Date	**Time**	**Atoms**	**T_{oven} Current**	λ_{las} (nm)	**Power**	**ABF? Film?**
11/14/2023	14:05	Yb	376.7 °C ** A	866.5146–866.5321 †	4.3 mW	yes no
12/05/2023	17:34	Rb	228.6 °C 2.85 A	780 **	**	yes yes
12/20/2023	19:51	Rb	264.4 °C 3.0 A	780.2378–780.2443	3.3 mW	yes no
	20:42		265.0 °C 3.0 A	794.9743–794.9827	3.5 mW	yes no
12/21/2023	17:47	Rb	264 °C 3.0 A	**	2.2 mW	yes yes
12/22/2023	14:07	Rb	24.8 °C 0 A	794.9743–794.9827	2.6 mW	no no
	14:12		24.8 °C 0 A	780.2380–780.2441	1.7 mW	no no
12/22/2023	16:17	Rb	254.4 °C 2.9 A	**	2.5 mW	yes yes
01/08/2024	17:00	Rb	238.4 °C 2.8 A	780.2380–780.2441	1.25 mW	yes yes

Continued on next page

Table 4.13 — continued from previous page

Date	**Time**	**Atoms**	**T_{oven} Current**	λ_{las} (nm)	**Power**	**ABF? Film?**
	18:02	Rb	239.2 °C 2.8 A	794.9743–794.9827	2.68 mW	yes yes
01/11/2024	N/A	Rb	238.9 °C 2.8 A	Laser Not Working	N/A	N/A yes
01/12/2024	12:18	Rb	239.2 °C 2.8 A	780.2330–780.2470	2.17 mW	yes yes
	12:43		239.2 °C 2.8 A	794.9689–794.9857	1.34 mW	yes yes
	13:11		239.2 °C 2.8 A	780.2316–780.2478	2.25 mW	yes yes
	13:53		239.2 °C 2.8 A	780.2316–780.2499	2.6 mW	yes yes
01/17/2024	11:00	Rb	240.0 °C 2.8 A	780.2417–780.2457	2.5 mW	yes no
	13:49		239.9 °C 2.8 A	780.2316–780.2499	4.14 mW	yes no
	14:29		239.9 °C 2.8 A	794.9678–794.9868	3.1 mW	yes no

Continued on next page

Table 4.13 — continued from previous page

Date	**Time**	**Atoms**	**T_{oven} Current**	λ_{las} (nm)	**Power**	**ABF? Film?**
	16:24		239.9 °C 2.8 A	794.9700–794.9890	3.0 mW	yes no
02/04/2024	17:52	Rb	207.95 °C 2.55 A	780.2448–780.2509	**	yes yes
03/08/2024	10:49	Rb	325.3 °C 3.5 A	780.2439–780.2480	0.98 mW	yes yes
	11:20	Rb	325.0 °C 3.5 A	780.2316–780.2499	0.95 mW	yes yes

† Laser EMM was used, center of scan range was 555.8031 nm.

In the last column, "yes" and "no" indicate if any ABF signal was observed.

In the last column, "yes" and "no" indicate if a film with atoms embedded was grown.

** Data exists but needs analysis run or converted for an exact answer.

Note that all laser wavelength ranges are scans begin at the higher wavelength.

Base folder for ABF data is: spinlab$_{d}ata > ABF_{S}AM > ABFData$.

After preparing the oven with Rb, there was some initial testing, but the Yb ABF experiments had proved beneficial as a signal was observed quickly for the Rb ABF experiments. Throughout the Rb ABF experiments, the full spectra for transitions of Rb-85 and Rb-87 around 780 nm and 795 nm were observed. The list of these transitions can be found at [Spe]. Because of this success, absorption tests were attempted almost immediately. To do these tests, a film needs to be grown with Rb atoms codeposited for at least some portion

of the growth. For initial testing, saturation from a high Rb density was not a concern as the goal was to see any kind of signal. To see the absorption spectra, the WLS data is used and some minor adjustments to the film transmission ratio plots are made. The absorbance of a film, A(λ) should be given by:

$$A(\lambda) = -ln(T(\lambda)) = \sigma_a(\lambda)nl \tag{4.15}$$

where $T(\lambda)$ is the transmission at wavelength λ, σ_a is the absorption cross section, n is the number density of Rb atoms in the film, and l is the path length of light through the film [Los20]. If there are Rb atoms within the Kr film, then they are expected to absorb light at particular wavelengths which would appear as sharp dips in the absorption plot. Several attempts were made growing films with the parameters for films to be used as solid traps. It was learned later that this had not worked previously, and that a different method, growing much thinner films at a much lower temperature was required to see any kind of signal. Unfortunately, even when growing the film at the appropriate thickness of 5 μm with the ideal growth rate of 5 μm/hr at the proper deposition temperature of 8 K, there was still no absorption observed!

Despite a lack of absorption peaks, some IMF attempts were made. The first was made on 2/4/2024 and the first successful IMF measurement was on 3/8/2024. The last entry in Table 4.13 corresponds to the successful IMF measurement. It is the last ABF measurement because unfortunately, this was the last Rb-doped Kr film that was able to be deposited before the laser broke. However, the film with a successful IMF measurement had several tests conducted on it, including more IMF experiments.

In Table 4.14, there are several entries in which ABF data was observed in real time

to verify the presence of Rb atoms exiting the oven, but no analysis of the data was done. For these cases, the data still exists and could be analyzed if desired, but was not necessary for the experiments at the time. Additionally, in the last column, if a measurement was attempted, then there is a yes/no to indicate if a signal was observed for ABF, IMF, and absorption (labeled WLS) experiments. Note that if the ABF signal was observed in real time only, with no plotted analysis afterwards, it is marked accordingly. Further, several tests were run on the same film, which is denoted by a date instead of film type.

For the Rb-doped Kr film from 3/8/2024, there was an IMF signal observed. As such, several tests were subsequently run on this same film. Wider scans to observe additional peaks were conducted. As there are two expected trapping sites for the Rb, when additional peaks to the primary triplet—with peaks at about 721 nm, 730 nm, and 743 nm—were observed, it was presumed they could belong to the other triplet. It was difficult to observe above 800 nm due to the limits of the optical filter in place. Most of the studies were focused on the primary triplet as they had the strongest and cleanest signal.

In addition to wide laser scans, there were laser power scans (LPS) which involved taking data for individual laser wavelength and power combinations. This process is explained further in the next subsection. Also, the IMF signal was observed over time. Here the laser was stable at one wavelength while the IMF signal was measured for hours to see how it changed over time. The IMF signal decreased by about 7% over the course of about 6.5 hours. There was a test done to see how the IMF signal changed over temperature as well. A full IMF scan was taken at the maintenance temperature of 8 K, then the IMF was monitored as the temperature was slowly increased to 28 K at which point another full IMF scan was taken, and the signal was monitored while ramping the temperature back down to 8 K and taking one last full IMF scan. Results of this test can be found later in this chapter.

Table 4.14: Absorption & IMF Data Collection Summary

Date	**Time**	**Type** **T_{dep}**	**Thickness** **Growth Rate**	**T_{oven}** **Current**	λ_{las} (nm) **Power**	**IMF?** **WLS?** **ABF?**
12/05/2023	19:48	Kr w/Rb 34 K	103.8 μm 132.8 μm/hr	230 °C 2.85 A	N/A N/A	N/A no yes*
12/21/2023	17:57	Kr w/Rb 34 K	93.7 μm 122.2 μm/hr	264 °C 3.0 A	N/A N/A	N/A no yes
12/22/2023	16:36	Kr w/Rb 8 K	5.2 μm 6.4 μm/hr	254.4 °C 2.9 A	N/A N/A	N/A no yes
01/08/2024	18:43	Kr w/Rb 8 K	5 μm 4.2 μm/hr	239 °C 2.8 A	N/A N/A	N/A no yes
01/11/2024	11:32	Kr w/Rb 8 K	5.1 μm 9.25 μm/hr	239 °C 2.8 A	N/A N/A	N/A no no
01/12/2024	12:37	Kr w/Rb 20 K	5.1 μm 5.4 μm/hr	239.1 °C 2.8 A	N/A N/A	N/A no yes

Continued on next page

Table 4.14 — continued from previous page

Date	**Time**	**Type** **T_{dep}**	**Thickness** **Growth Rate**	**T_{oven}** **Current**	λ_{las} (nm) **Power**	**IMF?** **WLS?** **ABF?**
01/17/2024	13:12	Kr w/Rb 8 K	5 μm 5.6 μm/hr	239.9 °C 2.8 A	N/A N/A	N/A no yes*
02/04/2024	17:39 21:25!	Kr w/Rb 8 K	5 μm 12.2 μm/hr	207.8 °C 2.55 A	730.0-760.0 **	no no yes
02/29/2024	21:53 23:27!	Kr w/Rb 8 K	5 μm 4 μm/hr	207.2 °C 2.55 A	700.0–760.0 1.03 mW	no no yes
03/08/2024	10:28 12:47!	Kr w/Rb 8 K	5 μm 5.77 μm/hr	325 °C 3.5 A	700.0–760.0 0.6 mW	yes N/A yes
03/15/2024	**! LPS	03/08/2024 Film	5 μm 5.77 μm/hr	239.9 °C 3.5 A	760.0 varies	yes N/A yes
03/21/2024	14:52!	03/08/2024 Film	5 μm 5.77 μm/hr	239.9 °C 3.5 A	700.0–800.0 1.2 mW	yes N/A yes

Continued on next page

Table 4.14 — continued from previous page

Date	**Time**	**Type** **T_{dep}**	**Thickness** **Growth Rate**	**T_{oven}** **Current**	λ_{las} (nm) **Power**	**IMF?** **WLS?** **ABF?**
	16:46!	03/08/2024 Film	5 μm 5.77 μm/hr	239.9 °C 3.5 A	760.0–840.0 3.8 mW	yes N/A yes
03/27/2024	**! LPS	03/08/2024 Film	5 μm 5.77 μm/hr	239.9 °C 3.5 A	varies varies	yes N/A yes
03/28/2024	17:06!	03/08/2024 Film	5 μm 5.77 μm/hr	239.9 °C 3.5 A	700.0–840.0 0.2 mW	yes N/A yes
04/25/2024	05:15! Counts vs Time	03/08/2024 Film	5 μm 5.77 μm/hr	239.9 °C 3.5 A	730.0 0.70 mW	yes N/A yes
05/01/2024	14:28! Temp. 8 K	03/08/2024 Film	5 μm 5.77 μm/hr	239.9 °C 3.5 A	700.0–830.0 1.4 mW	yes N/A yes
	19:50! Temp. 28 K	03/08/2024 Film	5 μm 5.77 μm/hr	239.9 °C 3.5 A	700.0–830.0 1.0 mW	yes N/A yes

Continued on next page

Table 4.14 — continued from previous page

Date	**Time**	**Type** **T_{dep}**	**Thickness** **Growth Rate**	**T_{oven}** **Current**	**λ_{las} (nm)** **Power**	**IMF?** **WLS?** **ABF?**
05/02/2024	00:22! Temp. 8 K	03/08/2024 Film	5 μm 5.77 μm/hr	239.9 °C 3.5 A	700.0–820.0 1.0 mW	yes N/A yes
05/03/2024	13:31!	03/08/2024 Film	5 μm 5.77 μm/hr	239.9 °C 3.5 A	700.0–820.0 1.1 mW	yes N/A yes
	15:52! Post- Laser Blast	03/08/2024 Film	5 μm 5.77 μm/hr	239.9 °C 3.5 A	700.0–820.0 1.0 mW	yes N/A yes
05/15/2024	12:58!	03/08/2024 Film	5 μm 5.77 μm/hr	239.9 °C 3.5 A	700.0–820.0 0.5 mW	yes N/A yes
05/16/2024	13:32	None	N/A N/A	N/A N/A	700.0–820.0 1.0 mW	no N/A yes

Continued on next page

Table 4.14 — continued from previous page

Date	**Time**	**Type** **T_{dep}**	**Thickness** **Growth Rate**	**T_{oven}** **Current**	λ_{las} (nm) **Power**	**IMF?** **WLS?** **ABF?**
	14:57	Kr	5 μm	N/A	700.0–820.0	no
	17:33!	8 K	5.36 μm/hr	N/A	1.5 mW	N/A yes
05/17/2024	13:37!	05/16/2024 Film	5 μm 5.36 μm/hr	N/A N/A	700.0–820.0 1.3 mW	no N/A yes
05/17/2024	**! LPS	05/16/2024 Film	5 μm 5.36 μm/hr	N/A N/A	varies varies	no N/A yes

In the last column, "N/A" means that the measurement was not attempted.

In the last column, "no" and "yes" indicate if a signal was observed.

* ABF data was collected to verify atoms traveling down the system only.

** Data exists but needs analysis run or converted for an exact answer.

! Timestamp for the IMF data. **! Many data files for labeled testing.

Base folder for film growth data is: spinlab$_d$ata $>$ $ThinFilmThickness$.

Base data folder film WLS data is: spinlab$_d$ata $>$ $SADiCS$ $>$ $Oceanview$.

Base data folder for IMF data is: spinlab$_d$ata $>$ $IMFData$.

Finally, there were also some IMF tests done on the substrate alone when there was no film and on empty, un-doped Kr films. This was done to provide a background IMF

measurements to allow for better isolation of the signal.

It is unclear why absorption was never observed, even when the conditions for the growth matched initial testing results from Dr. Loseth's thesis. The only theory at this point in time is that it has to do with the Kr film itself, as the film quality had been lower than usual. More testing should be done and suggestions for future work are included at the end of this chapter.

While the ABF simulation models the flow rate and angular distribution of atoms effusing out of the oven, the nozzle to film to CCD (NFC) simulation models these atoms from the nozzle exit to the film and their fluorescence to the CCD. The NFC estimates the portion of atoms from the oven nozzle that embed into the film, the atomic distribution throughout the film, and the expected fraction of their photon emissions that will be measured by the CCD. With a measured CCD image, measured laser distribution across the film, and the NFC model, their combination allows for the calculation of the fluorescence cross section spatially across a film. The following sections of this chapter were previously described some in Section 4.2, but now a breakdown of the analytical components of the NFC will explain how the experimental data translates to the calculated result.

4.4.2 Laser Power Scan Analysis

Imaging data collected via the CCD camera involves a more complex interpretation than merely converting the counts into photons. Counts measured come from various sources which can be summarized by a simple model equation that allows the tracing of all contributions to the raw counts. Fluorescence from the embedded Rb atoms, laser background, environment background, and intrinsic background are all factors to be considered. These can each be accounted for in the following equation:

$$C = \epsilon a(P)Nt + b(P)t + ct + (d_1 t + d_2) \tag{4.16}$$

where the variables carry the following meanings:

$C \equiv$ total counts recorded by the CCD

$\epsilon \equiv$ wavelength-dependent counts per photon ratio

$a \equiv$ wavelength-dependent, power-dependent embedded atom brightness in photons/(second*atom)

$N \equiv$ number of atoms embedded in a film

$P \equiv$ laser power

$t \equiv$ exposure time of the CCD

$b \equiv$ counts/second due to background laser light

$c \equiv$ counts/second from all non-laser light sources

$d_1 \equiv$ time-dependent bias counts per second of the CCD

$d_2 \equiv$ intrinsic background counts of the CCD, independent of time

Here, the first term represents the counts solely due to the fluorescence of the Rb atoms embedded in the Kr film. Variable a is the atomic brightness of the implanted atoms and is the most important piece of the puzzle, as it is the unknown. It has units of $\frac{photons}{atom*s}$, is wavelength-dependent and laser-power-dependent to some degree, but more data will be needed to map out that dependence. Note that a will need to have an adjustment for the solid angle in order to find the total atomic brightness. As the photons are presumed to emit isotropically, only a fraction of them are being recorded by the CCD. Thus, defining the

total number of photons emitted in time per atom will require this correction. Meanwhile, ϵ can be found from doing the photon to count calibration with the CCD camera, discussed in Section 4.2.2. This value is measurable, but wavelength-dependent. For now, the peak emission wavelength of Rb in Kr is 923nm [GSM12] and so that was used to find ϵ for now. Further, variable N can be determined from the ABF data, and the exposure time is a known number.

The second term corresponds to the counts due to the presence of the laser incident on the film and substrate. Despite the improved geometry of the experiment, optimized within the limits of current spatial availability and optical access to minimize the laser background, there is still a non-zero amount of laser light background from reflections within pSAM that terminate on the CCD sensor. That said, b is expected to have a linear dependence on laser power and also be something that can be well-defined from measurements with empty films and the substrate alone with no film. It is important to keep in mind that the CCD is a sensitive detector, and therefore can become saturated if there is too high a laser power. Further, the atoms can become saturated at too high a laser power too, in which they remain disproportionately in the excited state. Saturation in one or possibly both of these regards was observed in the laser power scans of the Rb-doped Kr film. All data points above the saturation level were ignored for analysis.

The third term of the simple model relates to all background light aside from the laser. This mainly includes contributions from the room and indicator lights. There are efforts made to limit the external light that could be picked up by the CCD, but this background source is not negligible. It should be approximately the same over time though, which is why the term has only a constant variable in counts/second multiplied by time. This can also easily be measured.

Finally, there are two terms associated with the bias of the CCD itself. These terms, $d_1 t$ and d_2, are the time-dependent and time-independent counts intrinsic to the CCD when no light is hitting its sensor, referred to as the bias. These terms are also well-defined through measurement.

The sum of these terms equate to the total counts recorded by the CCD camera. This value is measured, leaving only the first term to be calculated to find the atomic brightness. Note that the second and third terms have a "hidden" ϵ as all light hitting the sensor would be photons that need converting to counts. However, as these terms are calculated or measured in terms of counts, there is not a need to distinguish two variables instead of one for each term.

The simple model defines the counts recorded by the CCD camera and provides insight about how to isolate the counts due solely to the fluorescence from embedded atoms. Direct measurements of the other background terms enable a more precise fluorescence cross section to be obtained via the atomic brightness. Starting with the term that is present in all CCD images, regardless of Rb atom implantation or laser usage, the bias of the CCD can be defined through simple measurements. Testing was done to determine if the bias was time-dependent in some part. As shown in the figure below, it does not have any time-dependent component. Figure 4.18 is the result of taking bias "scans" at different exposure times. For each data point shown, the CCD sensor was covered so that no light could enter and 100 frames were recorded and averaged together. Then the average frame was summed up for a total counts in the frame. In the below figure, the counts within the region of interest (ROI) that is used repeatedly throughout the analysis is shown. These points were divided by the average of all points so that the percent difference between them can be easily seen. With a data point for various exposure times, spanning several orders of magnitude, it is clear that there is no

time-dependence. The error bars shown on Figure 4.18 are the standard deviation of the sum of the frame throughout time for each exposure, adjusted for the percent difference.

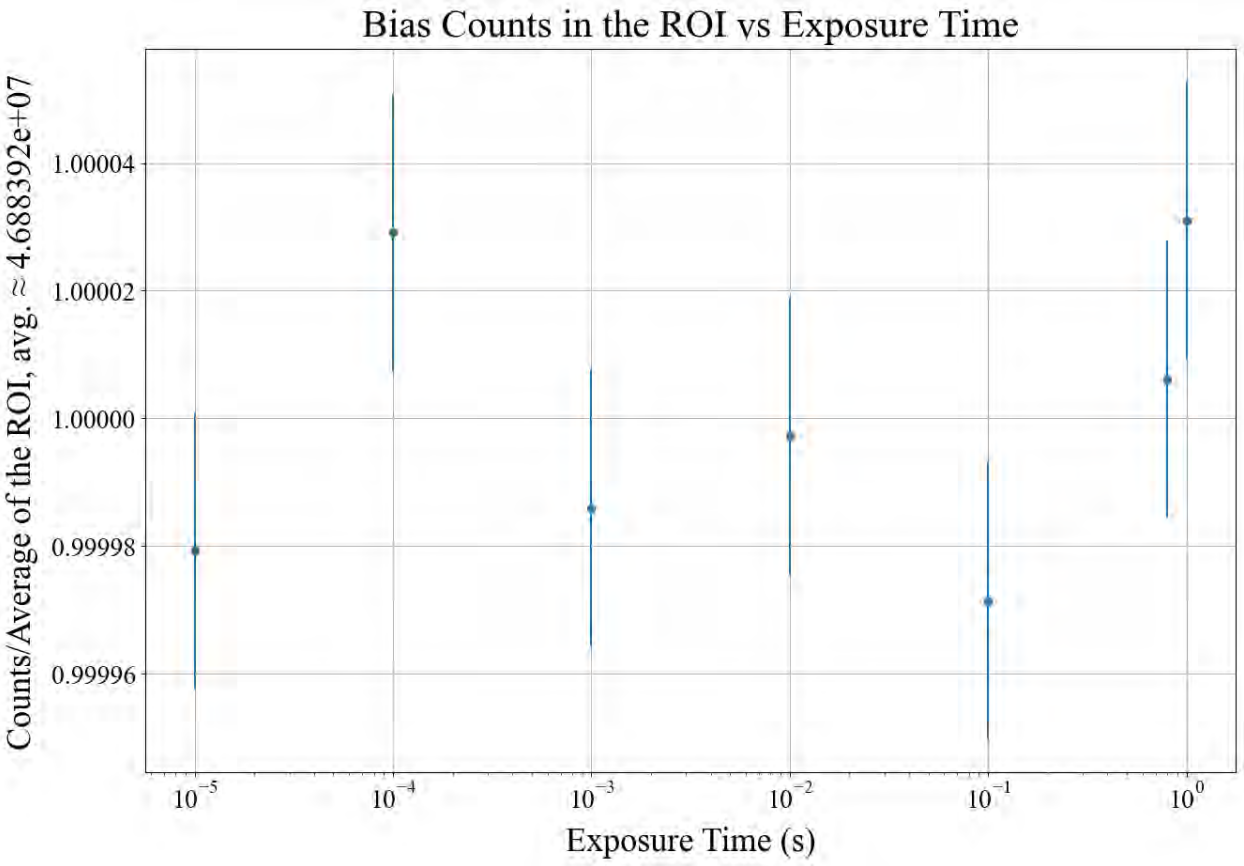

Figure 4.18: This image shows the bias counts of the region of interest (ROI) for varied exposure times in relation to the average. There is no time dependence observed as the measurements vary about the average no matter the exposure time of the scans taken.

Additionally, the standard deviation across the average frame, comparing each pixel to the others, was very low at about 0.22, whether looking at it for the entire frame or only the region of interest (ROI). This shows that there is a low variance pixel to pixel for the bias, yielding a flat image when plotted. This is expected as a bias should be even and random across the frame. There were a few pixels that would have a random higher standard deviation, but these were in fact random as they were not consistently higher for data at different exposure times and it did not repeat at the same pixel location. Further,

the standard deviation was observed for each pixel throughout all frames of a measurement, meaning the variance of the counts in one pixel over time. The values varied randomly in time which is expected of a bias. There did seem to be a small outlier for the data point produced from the measurement with a 10-second exposure time. It was still very close to the other data points, but since all exposure times for the regular collection of data is less than one second, it was thrown out for a tighter average.

Having shown that the bias has no time dependence, the simple model equation can be adjusted to reflect that:

$$C = \epsilon a(P)Nt + b(P)t + ct + d \tag{4.17}$$

where now there is only one term for the bias in which:

$$d \equiv \text{intrinsic background counts of the CCD, independent of time}$$

Based on the bias tests conducted, the full frame average for the bias is 629733467.7614286 counts, rounded to the nearest count of 629733468, or about 6.3E8, counts per frame. The value for the bias counts in the region of interest (ROI) studied throughout this thesis is 46883919.77285714, rounded to 46883920, or about 4.7E7, counts per ROI.

As described, the second and third terms of the simple model represent the counts recorded by the CCD due to the laser background and non-laser, non-bias background respectively. Each term is time dependent and the laser background term is, as expected, dependent on laser power. Both of these terms can be determined through data collected from a series of laser power scans.

Laser power scans (LPS) were collected and analyzed to gain insight about the amount of laser background present at different laser wavelengths and powers and to model the laser intensity distribution across the film. The latter was explained in Section 4.2.2. The LPS scans were conducted on the film grown on 3/8/2024, which showed an IMF signal for a Rb-doped Kr film. Taking this data involved setting the laser to a specific, stable wavelength and set power before gathering 100 frames of data with the CCD. These frames were then averaged into one composite frame and the process was repeated until there was an average frame for each laser wavelength and power combination accessible. There were limitations to what laser power could be reached for each wavelength, but for all data sets, multiple orders of magnitude were included in the range of powers measured. The lowest power used was 0.002 mW for all laser wavelengths and the maximum power varied depending on wavelength between 8-25 mW. The laser wavelengths chosen included three strong peaks at 721 nm, 730 nm, and 743 nm, as well as two troughs in the data at 706 nm and 757 nm. At the time, it was thought that the troughs might be where there is no signal, but it was deduced later that the peaks were very broad so there may still be some counts related to IMF at these wavelengths. For this reason, the process was repeated on an empty, un-doped Kr film grown with the same parameters as the doped film mentioned. With LPS data from doped and empty films, a simple subtraction could show the counts due solely to the signal.

To do a subtraction between the LPS doped and empty film data sets, lines of fit were made using the uncertainty of both the measured power and of the measured counts as inputs. All LPS lines for the doped and empty films can be seen in Figure 4.19. It is clear that counts measured by the CCD camera linearly increase with laser power. It should be noted however, that saturation of the CCD occurred above 3.8E15 counts/s/frame which corresponded to approximately 5 mW for the doped film at signal peak wavelengths. The

saturated points were not included for calculating the lines of fit. While saturation can also occur for the Rb atoms themselves—resulting in a disproportionate amount of time spent in the excited state—it is unclear based on the LPS data if only the camera was saturated, but that is the case assumed. As calibration measurements and future laser-induced fluorescence measurements for this project do not anticipate using a laser power over 1 mW, this saturation will not be a concern moving forward. The LPS data from the empty Kr film showed that laser background is still present and minimization would improve the signal to background ratio. It did show though, that the laser background does not appear to be significantly laser wavelength-dependent.

Residuals from the LPS experiments on both the Rb-doped and empty Kr films are shown in Figures 4.20 and 4.21. The residuals are found by subtracting the line of fit at the same power at which the measured data points were recorded. In other words, the residuals are the data points less the line of fit. Again, data points above saturation level were excluded. For both the Rb-doped and empty Kr films, the residuals do not show any consistent patterns and are scattered about the 0-line. The residuals are further from the 0-line with the LPS data from the doped film. One possible explanation for this is that there are two sources contributing to the increase in counts—the Rb atoms' photon emissions and the laser power itself.

After subtracting the LPS lines of the empty film from the corresponding LPS lines of the Rb-doped Kr film, Figure 4.23 resulted. Note that the lines of fit for 706 nm and 757 nm are overlapping. While they appear to possibly carry some counts due to Rb, they have significantly lower slopes than the other three lines as the other lines are at peak excitation wavelengths of 721 nm, 730 nm, and 757nm.

Another piece of information learned from the LPS studies came from finding the y-

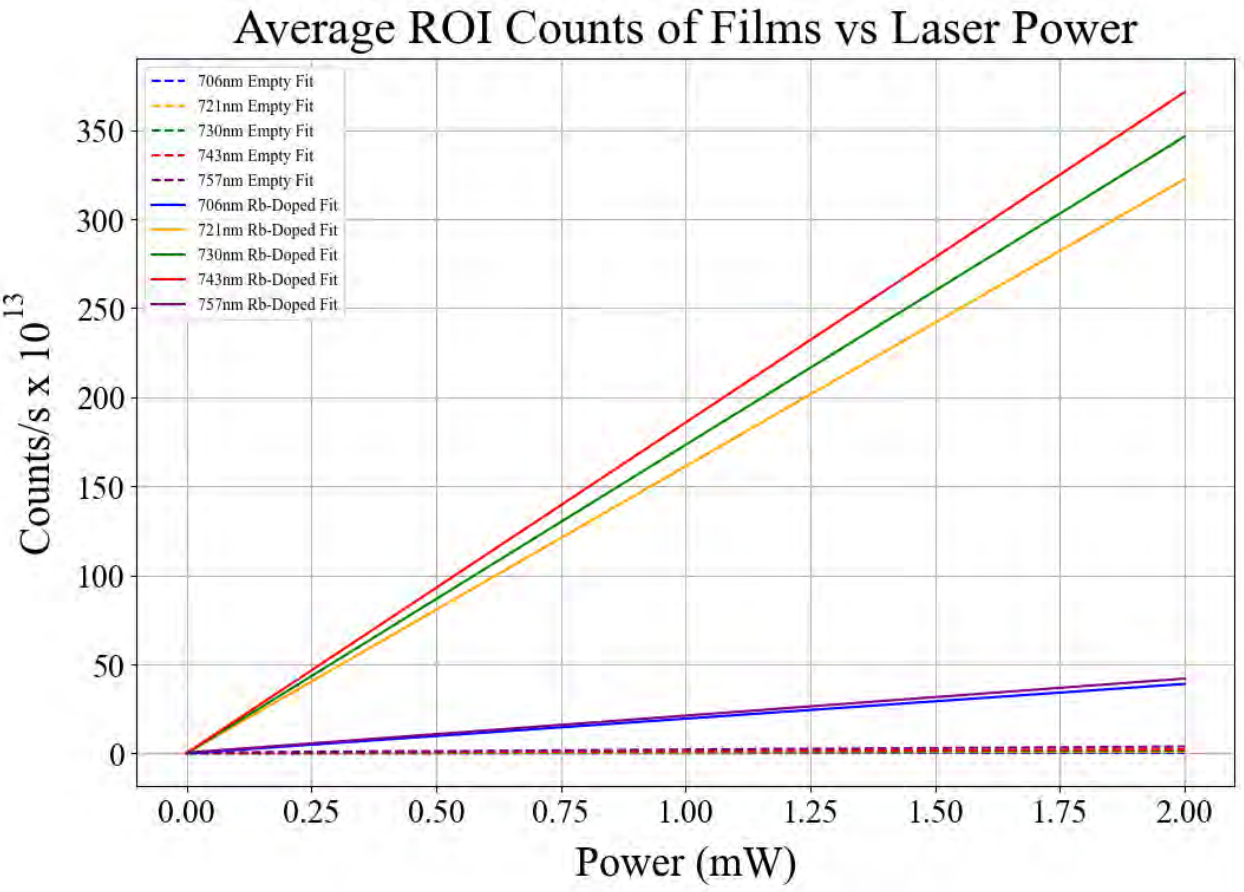

Figure 4.19: This plot shows the best lines of fit for LPS on the Rb-doped Kr film and on an empty Kr film grown with the same parameters. It is clear to see that the counts are proportional to the laser power and that the Rb-doped film has obvious higher counts than the LPS fits for the empty film.

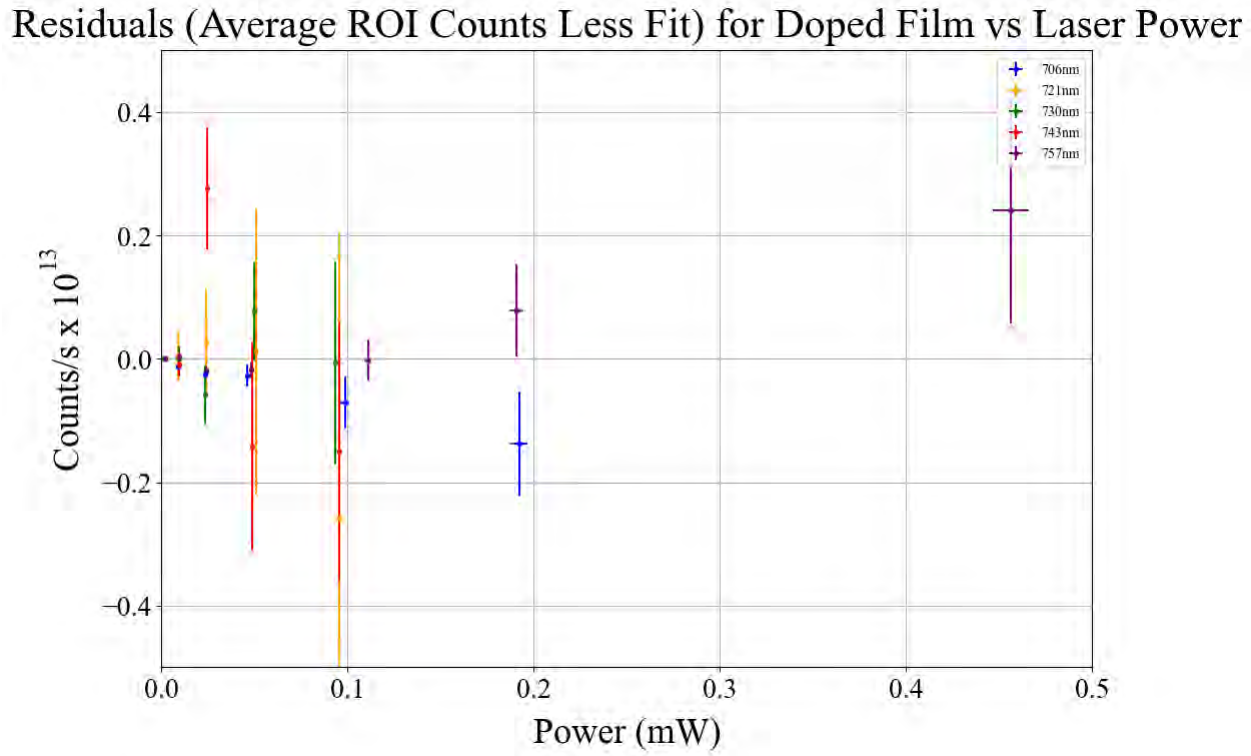

Figure 4.20: This plot shows the residuals for LPS on the Rb-doped Kr film. No clear pattern is observed.

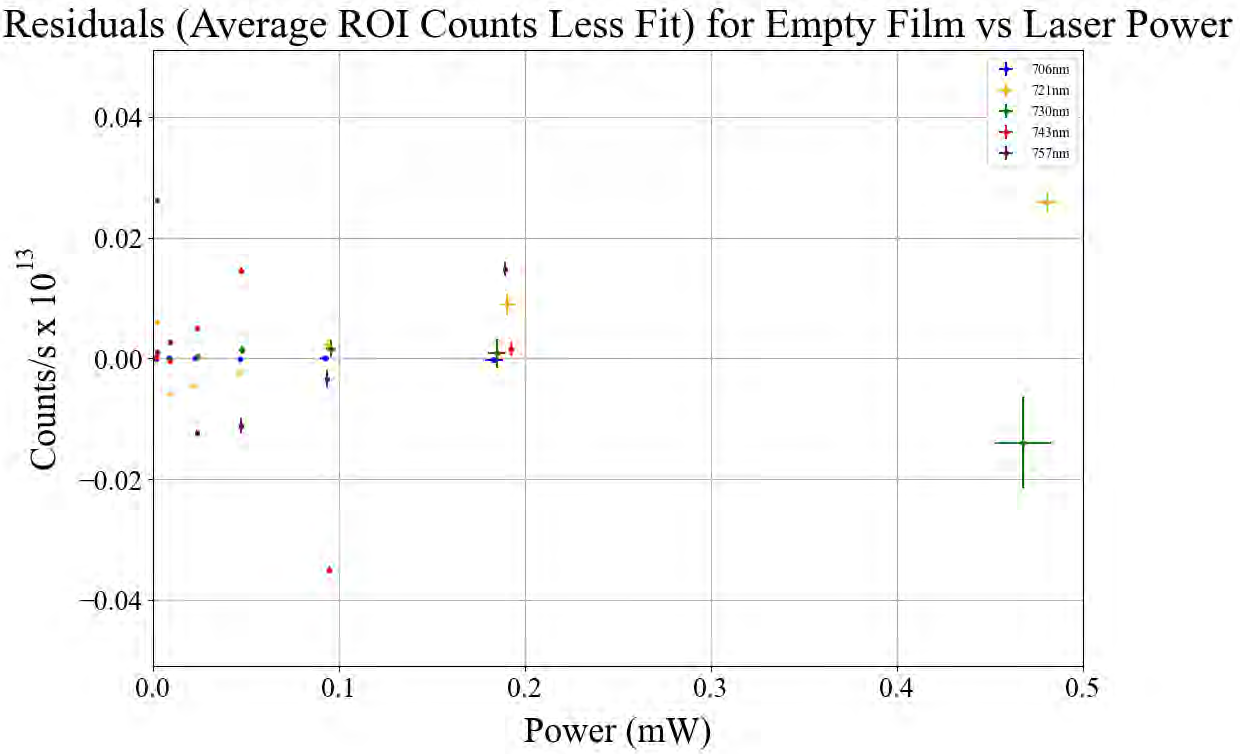

Figure 4.21: This plot shows the residuals for LPS on the empty Kr film. No clear pattern is observed, suggesting a linear model is a good fit to describe the relationship between counts/s and laser power.

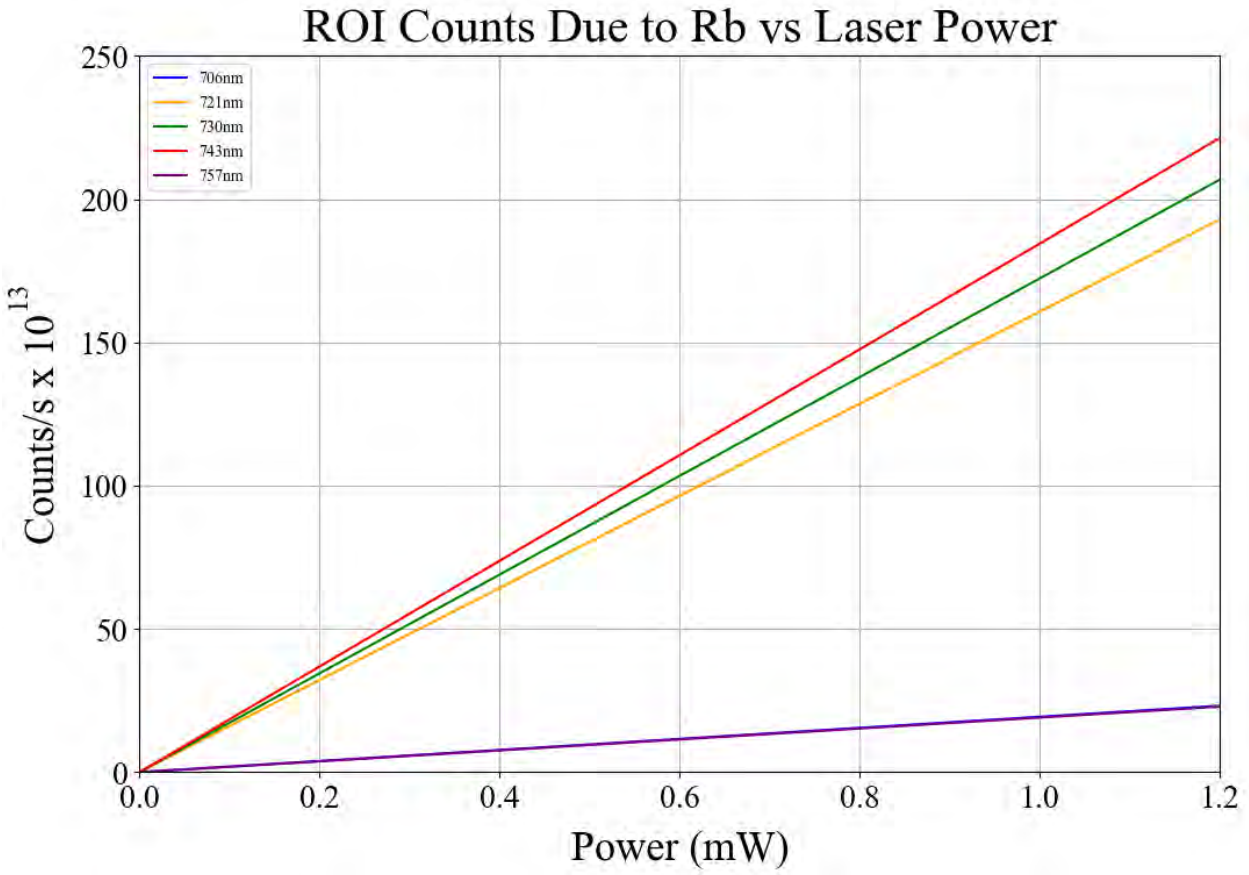

Figure 4.22: This image shows a subtraction between LPS data. The lines of fit for the data collected from scans on an empty Kr film (grown 5/16/2024) were subtracted from the lines of fit for data collected from scans on the Rb-doped Kr film grown on 3/8/2024. The off-peak data for 706 nm and 757 nm laser excitation wavelengths overlap and are much lower than the peak data. For IMF results, a laser excitation of 721 nm, 730 nm, and 743 nm were the three strongest peaks.

intercepts for the empty film measurements. When the LPS measurements were taken for the empty film, some scans with the laser closed—so a laser power of zero—were taken as well. These were used to adjust for the background of the environment. A verifiable offset between the expected y-intercept found through curve fitting and the data points measured with the laser shuttered for zero-power data was observed. The vertical offset should correspond to the environmental background—room and indicator lights mostly—but peculiarly, this background appears to be wavelength dependent. A consistent y-intercept across all laser wavelengths is expected, but this data shows that there is an offset from where the y-intercept should be based on the LPS lines of fit and the measured no-laser background. The source of this offset should be explored so that it can be mitigated or at least accounted for. Possibly, there is a wavelength dependence on the CCD camera or even the power meter that has not yet been taken into account. One way to test this would be by using a different model of power meter/CCD for conducting the same LPS study. Another option is applying better blackout materials to mitigate environmental contributions altogether.

The LPS scans were useful in confirming that the photon counts are in fact linearly related to the laser power. Additionally, the subtraction between the data for the Rb-doped and empty Kr films allowed for a measurement of the counts/s due to only the signal from the embedded Rb atoms. This information was used to calculate the fluorescence cross section and will be discussed in Section 4.5.

4.4.3 ABF Analysis

The atomic beamline fluorescence measurements were described previously. For the analysis, the data collected is plotted as a spectra. Examples of the spectra can be seen in the following figures.

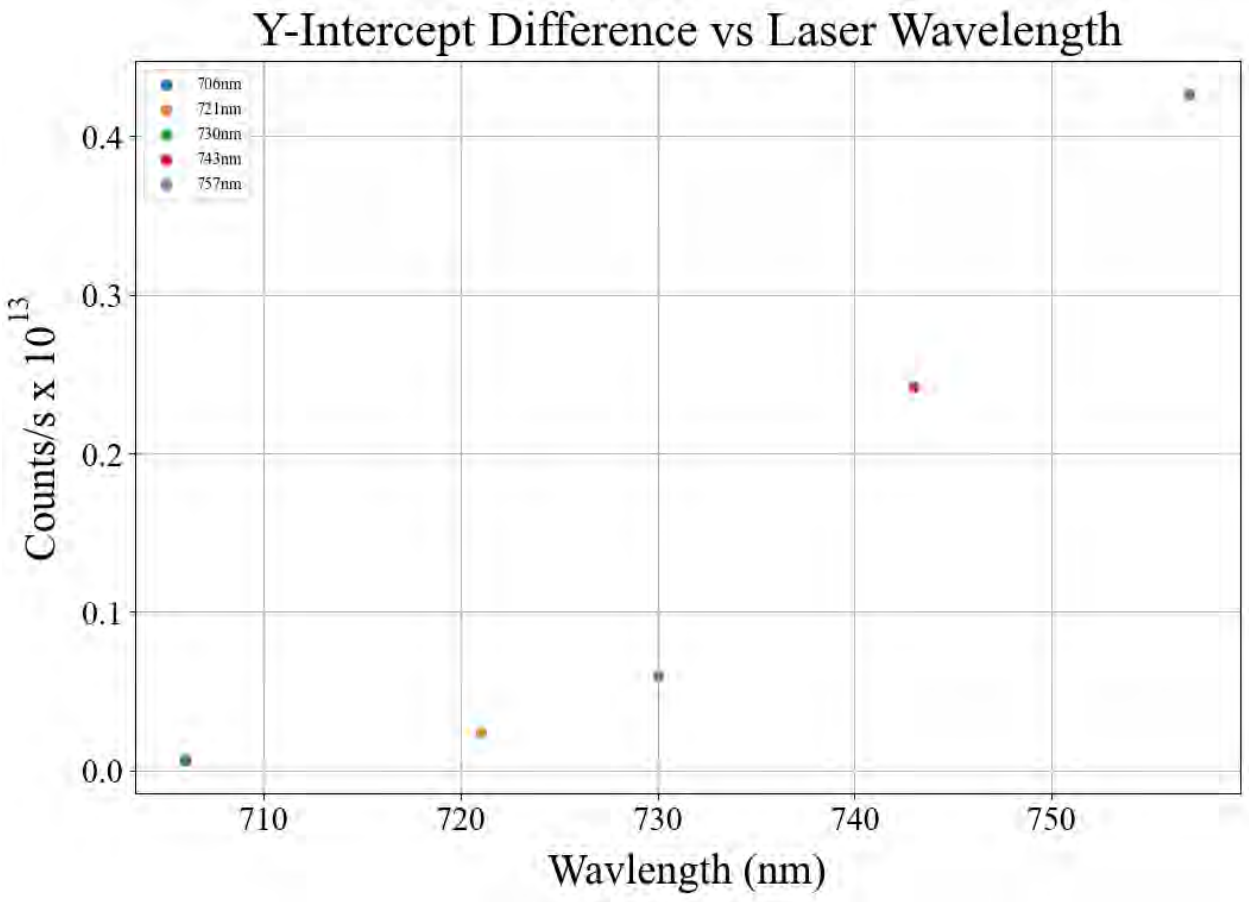

Figure 4.23: This image shows the differences between the line of fit y-intercepts and the zero-power LPS measurements taken on the empty Kr film. Note that there is an upward, non-linear trend. This implies that there is some wavelength dependence, but it is unclear on what the cause could be.

Figure 4.26 shows the same kind of data, still with Rb atoms, but this time the peaks are much broader. This, and potentially the additional peak as well, are consequences of a very high oven temperature. With a higher oven temperature, the angular distribution of atoms exiting the nozzle is broadened and that translates directly to the shape of the peaks. This data was taken around the time of the Rb-doped film growth on 03/08/2024 which showed successful IMF measurements.

Utilizing the information from this ABF spectrum, simulation code previously discussed can determine the angular distribution and flow rate of Rb atoms effusing from the oven

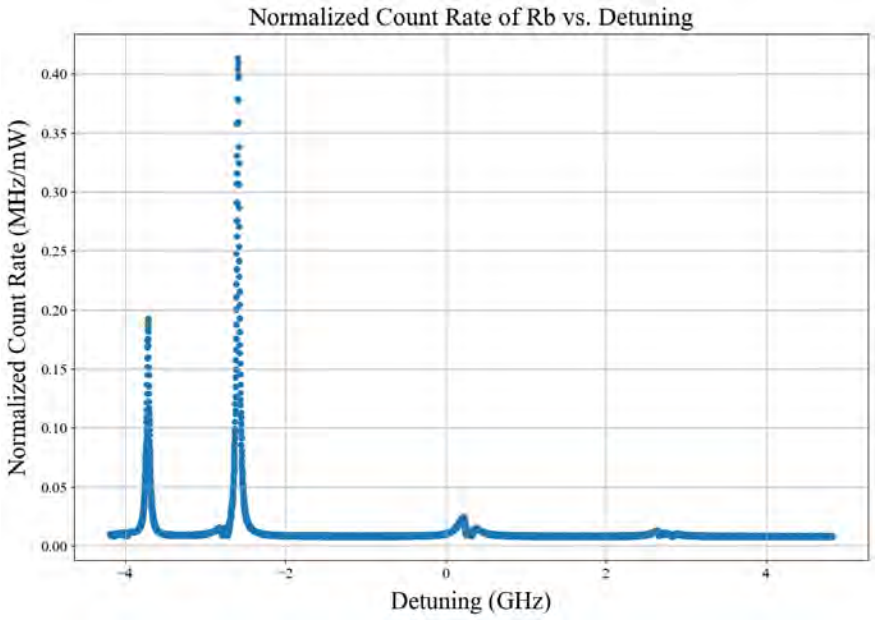

Figure 4.24: This plot shows the ABF spectra for Rb-85 and Rb-87 around 780 nm and are in agreement with the literature [Spe].

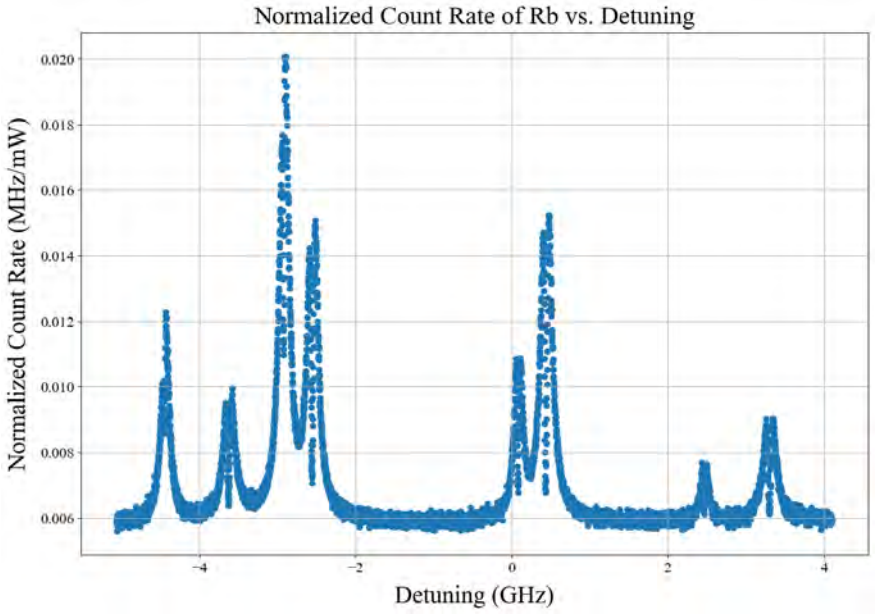

Figure 4.25: This plot shows the ABF spectra for Rb-85 and Rb-87 around 795 nm and are in agreement with the literature [Spe].

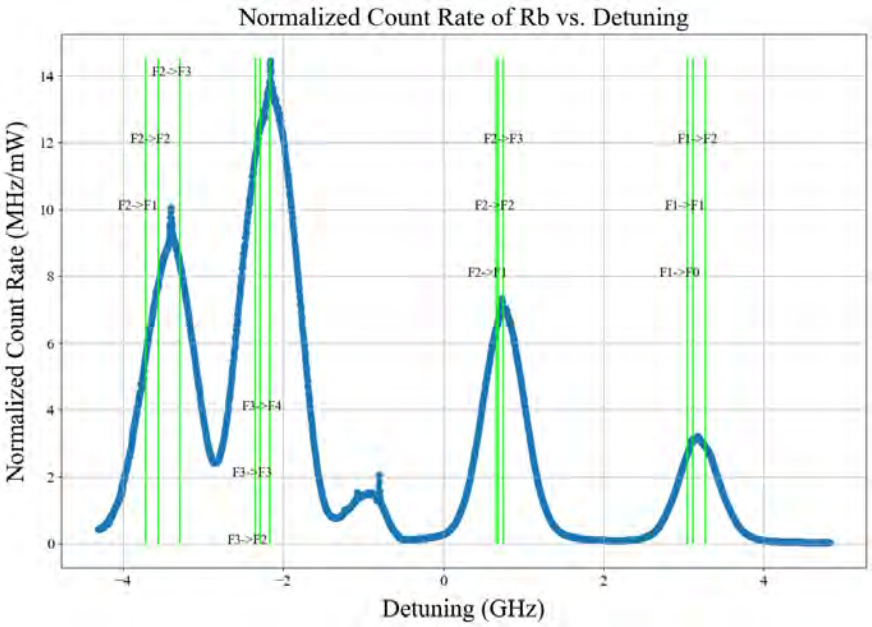

Figure 4.26: This plot shows the ABF spectra for Rb-85 and Rb-87 around 780 nm with the corresponding transitions annotated and are in agreement with the literature [Spe]. Note that these peaks are much broader than in Figure 4.24. This is due to the higher oven temperature broadening the angular distribution of the Rb atoms effusing from the nozzle. The additional peak is expected to be a consequence of the high oven temperature.

nozzle. This flow rate was determined to be approximately 9.29E10 atoms/s. The simulation's spectra which matched computational information and experimental data was shown in Figure 4.13.

This flow rate can then be inserted into the NFC simulation code to determine the atomic distribution of Rb atoms throughout a film. The NFC code currently assumes a gradient distribution, but it can control where the focal deposition point is located. Figure 4.27 shows the results. The rectangle outlines the region of interest (ROI) frequently used in describing results as it avoids the "mystery" spot on the film which may or may not have unknown effects on the fluorescence measurements. Also, there is a green dot at the edge of the substrate and film surface. This was used as a focal deposition point in testing, but ultimately there was not significant impact, so a centered focal deposition point was used

moving forward.

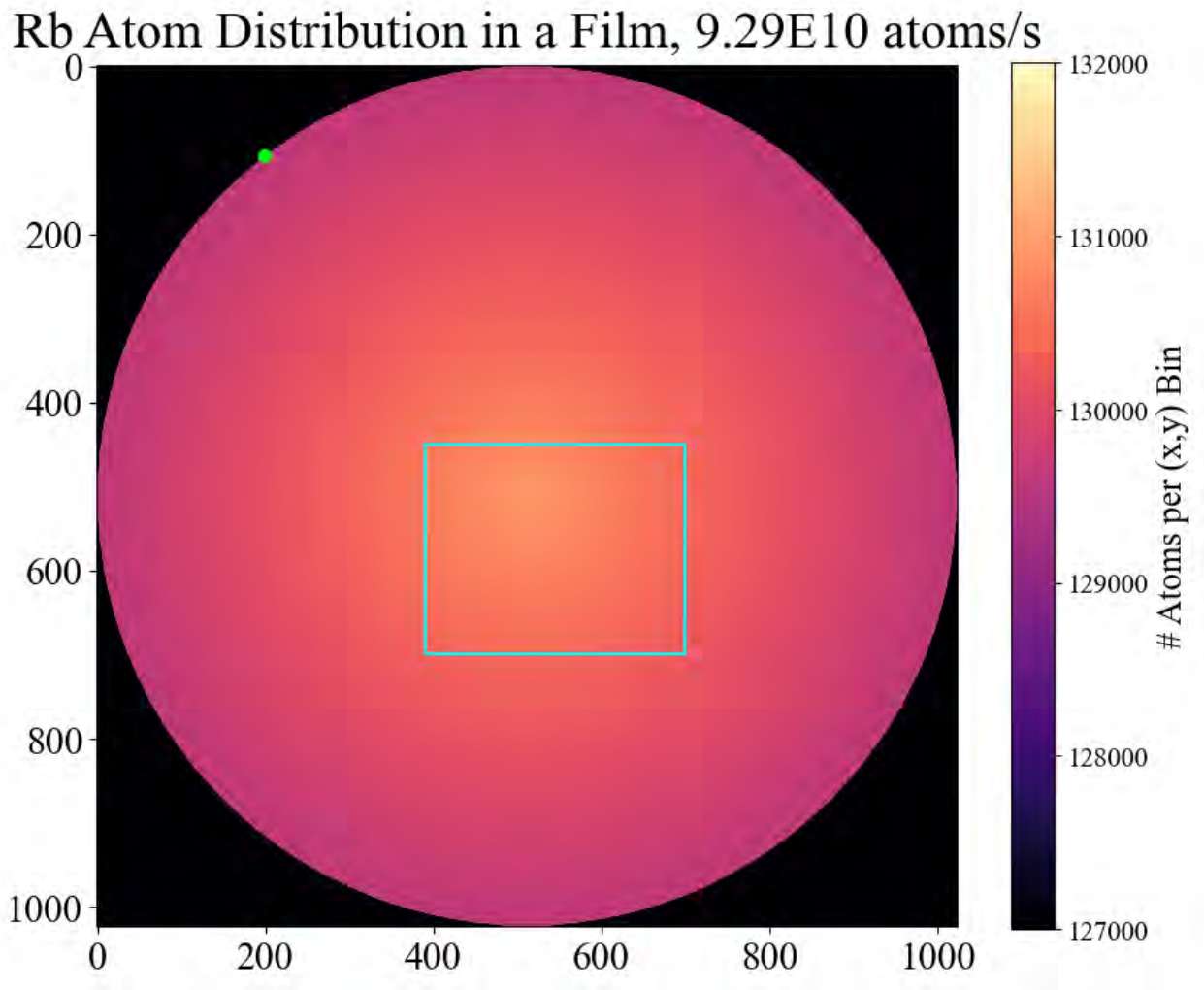

Figure 4.27: This image shows the distribution of Rb atoms throughout a film. The rectangle outlines the ROI. At the edge of the film, a green dot was placed, not only to highlight the edge beyond which all bins were set to contain zero atoms, but also to show an extreme case of where the focal deposition point of atoms may be. With an off-center focal deposition point, however, the total number of atoms given the high flux of them out of the oven nozzle did not have a drastic affect on the simulation. Note that this gradient is rather short in range, and this is due to the broad angular distribution of atoms out of the oven nozzle.

4.4.4 IMF Analysis

The experimental parameters for IMF measurements were explained in Section 4.3.3. Analysis for IMF is similar to ABF in that a spectrum is produced from collecting fluorescence

from excited atoms via a light-collecting lens and a detector. With IMF though, the counts are recorded by a CCD camera instead of an SPD detector, which means there is now spatial information about the fluorescence. Additionally, the same atoms are being analyzed over multiple IMF measurements since they are implanted in a film, rather than in ABF when a stream of atoms are being excited.

Despite the lack of observation of absorbance, the IMF results obtained showed spectra that aligned with the preliminary results from BTL thesis [Los20]. The first set of IMF data from the Rb-doped Kr film grown on 3/8/2024 is shown in Figure 4.28. IMF data collected by the CCD can be analyzed spatially or in the case of the IMF spectra, by averaging over the film and reporting the count rate over laser excitation wavelength. Spatial observations can shed light on irregularities in the film, as was observed with the so-called "mystery spot". It also allows observation of where the Rb atoms are embedded. As calibration studies continue, single atom observations seem promising as the locations of the Rb atoms was observed.

After this signal was observed, the Rb-doped film went a myriad of testing to gather data about the effect of time, temperature, and incident laser exposure on the strength and shape of the peaks. The three strong peaks observed correlate to the blue triplet observed in previous reports [GSM12, BW83] and the half peak observed around 701 nm appears to correspond to a high Rb density [Los20]. Notice that the very edge of another peak begins at the edge of the spectra near 760 nm. This led to wider scans to explore how many peaks could be observed. There are two trapping sites expected for Rb atoms embedded in Kr films, the other of which is a red triplet with peaks at 765 nm, 787 nm, and 813 nm [GSM12, Los20]. The peaks associated with the red triplet were observed in later scans, as shown in Figure 4.32.

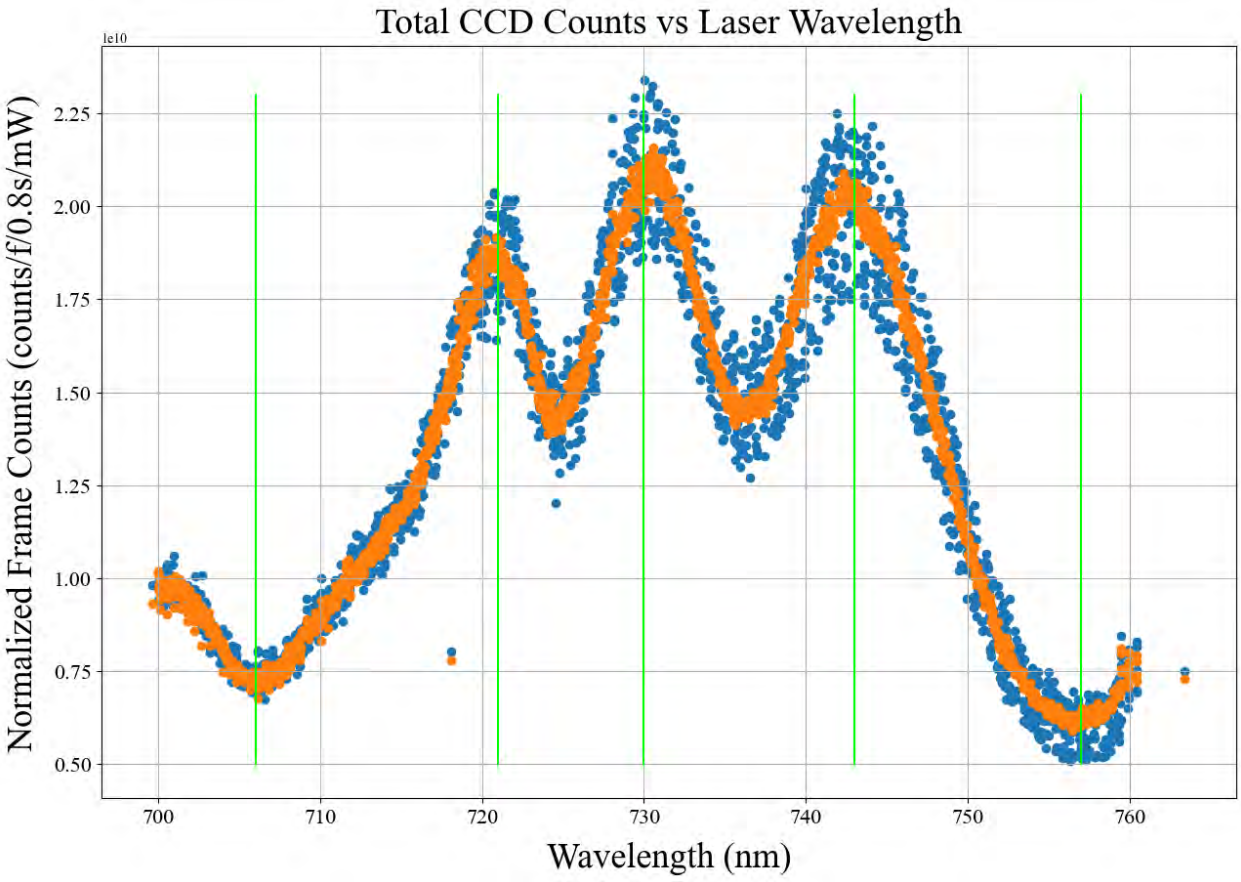

Figure 4.28: The first successful attempt of an IMF measurement with the refined experimental setup and procedure. Peaks at 721 nm, 730 nm, and 743 nm are in agreement with BTL thesis [Los20] and previously reported spectra [GSM12].

IMF data is what is used to find the FCS by converting the counts to number of photons, adjusting for the solid angle of fluorescence collection, and accounting for the laser intensity and number of atoms embedded in the film. Combining the experimental parameters with the measured data enable the discovery of the FCS measurement and is discussed further in Section 4.5.

4.4.5 Solid Angle Factor Analysis

The solid angle factor was calculated based on the geometry of the setup. It was thoroughly discussed in Section 4.2.6. Notably, the solid angle factor currently calculated will remain the same if the same experimental setup is used. A depiction of the solid angle factor can be seen in Figure 4.16. There is a gradient to the factor as, geometrically speaking, more photons from atoms embedded in a film will hit the center of the light-collecting lens. This model assumes point to point imaging, which as aforementioned means that photons from (x, y) bin on the film will translate to hitting a corresponding (x, y) pixel on the CCD camera's detector no matter where on the lens the photons are collected. In Figure 4.16, the colorbar scale shows that the gradient for this too is slight.

4.4.6 Uncertainty Estimates

For the LPS studies, uncertainties for the laser power and CCD counts were propagated through to find the lines of fit. Because each data point came from the average over a composite frame from 100 individual frames, standard deviations began with counts across the film and throughout the time that the frames were collected. These deviations as well as the laser power deviations during the data collection corresponding to each combination of

laser power and laser wavelength were all included when finding a line of fit. Residuals for these lines of fit were shared earlier in this section and showed no trend, supporting that the lines of fit were good models. An orthogonal distance regression (ODR) was the curve-fitting tool used to create this lines of fit, with a basic linear function as the model. The slopes, y-intercepts, variances, and standard deviations are summarized in Table 4.15 for the LPS studies on the Rb-doped and empty Kr film grown under the same conditions.

Table 4.15: ODR Model for LPS Lines of Fit

Rb-Doped Kr Film				
Laser λ	**Fit Slope $\frac{\text{counts}}{\text{s*mW}}$**	**St. Dev. Variance**	**Fit y-int $\frac{\text{counts}}{\text{s}}$**	**St. Dev. Variance**
706 nm	19.49	0.81 6.9E-2	0.076	0.0036 1.4E-6
721 nm	161	0.83 10.8	0.14	0.0017 4.5E-5
730 nm	173	0.89 2.00	0.18	0.0035 3.2E-5
743 nm	186	2.65 4.47	0.29	0.0102 6.7E-5
757 nm	20.80	0.23 3.2E-2	0.47	0.0013 1.1E-6
Empty Kr Film				
Laser λ	**Fit Slope $\frac{\text{counts}}{\text{s*mW}}$**	**St. Dev. Variance**	**Fit y-int $\frac{\text{counts}}{\text{s}}$**	**St. Dev. Variance**
706 nm	0.178	1.28E-3 1.16E-5	0.068	3.09E-5 6.74E-9
721 nm	0.430	0.111 1.50E-5	0.086	0.0025 7.70E-9
730 nm	0.799	0.0180 1.56E-4	0.123	0.0004 7.77E-8
743 nm	0.984	0.1091 4.09E-5	0.306	0.0024 1.98E-8
757 nm	1.708	0.0590 5.47E-5	0.491	0.0018 5.32E-8

Throughout the NFC simulation, standard deviations pixel to pixel across the film were very low, typically less than 1 % of the mean value. Atomic distribution for example had

a standard deviation per mean of 0.11 % across the ROI. Over the solid angle factor in the ROI, there is a standard deviation of 6.71E-08 for a mean of 9.21E-4. This yields a miniscule standard deviation to mean ratio of 7.29E-05, or 7.29E-3 %. And finally, the laser power distribution ratio across the ROI has a standard deviation of 5.31E-09, a mean of 1.25E-06, resulting a standard deviation per mean of 0.00423, or 0.423 %.

Equipment used for taking the ABF and IMF measurements is included in previous sections. Setting the laser wavelength is accurate within ± 0.0001 nm and this remains stable for CCD scanning at static laser wavelengths, such as for the LPS studies. When scanning the laser across a range though, the wavelength may fluctuate a bit more when stitching. The laser power was relatively stable for static laser wavelengths, fluctuating around 0.1 mW. When scanning the laser it may change significantly more, but how it does varies each time. Reviewing the specific data collected will show the range over the scan. For ABF measurements, a current supply is used to heat up the oven. With a constant current, after reaching an equilibrium, the temperature is typically stable within 0.5 °C. For IMF measurements, the film thickness should be relatively accurate as the thickness is measured in real time by monitoring the thin film interference pattern. Therefore, a reasonable estimate is that the films are within 0.1 μm. Lastly, when the photon to count conversion experiment was conducted, the photon to count ratio was measured to be 5.2 photons/count with an estimated uncertainty of 10 % due to the uncollimated laser beam, geometry of the setup, and transmission rates of the filters used.

4.5 Measurement of the Fluorescence Cross Section

After conducting an asynchronous dual fluorescence (ADF) experiment, the collected data needs to be analyzed to extract the fluorescence cross section. It is this value, which is directly related to atomic brightness and thus the IMF measurements, that needs to be investigated to see how it changes with different parameters of the experiment. The future work that should be done to have a comprehensive understanding of this value for atoms implanted in a noble gas solid will be detailed in Chapter 5, but here is where the current analysis and methodology behind the choices made will be explained.

4.5.1 Fluorescence Cross Section Measurements and Conclusions

The final number for the fluorescence cross section (FCS) measured is based on a mean of the FCS calculated spatially across the region of interest (ROI) to avoid any skewing from the "mystery spot" on the film. Said "mystery spot" is an irregularity in the film texture and possibly clarity that had been present for several months. The only factor noted that had changed since before it existed was that the compressor was having more errors with the water temperature being too cold. It is possible there is a different problem, such as a bend or kink in the capillary tubing that the Kr gas travels down, but it should be investigated as the substrate was replaced and the issue was still present. Note that an adjustment to the capillary tubing near the substrate was also tested without any notable change to the film quality. Possibly the capillary tubing higher up within pSAM is getting too cold and causing sputtering of some kind. There were several instances, though inconsistent, of clogging along the gas flow pathway that interrupted Kr film growths. Since the films used for calibration studies are so thin, this was less of an issue outside of depositions for full thickness noble

gas films that emulate the size requirements for use as solid traps.

The FCS was calculated using modeled atomic distribution based on ABF measurements, measured laser power distribution, and the modeled solid angle factor based on setup measurements. These factors make up the majority of the FCS equation, Equation 4.1, and work with the measured data from the CCD camera to find the FCS.

A few methods were explored for calculating the FCS. The first involved subtracting the LPS data of an empty Kr film from that of a Rb-doped Kr film. With this method, the LPS data from the empty Kr film includes an account of all background sources. Scans taken of the empty film, which was grown to the same specifications as the Rb-doped film, would include laser background, environment background, and the intrinsic CCD background. Furthermore, it would include any alterations to the fluorescence measurements caused by the presence of a Kr film, such as light scattering from vacuum-pockets within the films discussed previously with the Bubble Model [Noo21]. Therefore, subtracting the empty film LPS data from the Rb-doped Kr film LPS data would result in a measure of counts due solely to the embedded Rb atoms. The plot of the LPS subtraction was shown in Figure 4.23 and the result was translated to the FCS. The LPS method found an FCS of 1.68e-16 cm^2/atom for a laser wavelength of 730 nm. The FCS measurements via the LPS method for the five laser wavelengths of interest throughout this paper are shown in Figure **??** in the next section. The uncertainty was found by combining effects from uncertainties of the photon to count ratio (10 %), of the solid angle geometric factor (3 %), and the LPS fit's slope uncertainty (0.5 %). This yields an estimated uncertainty of 10.5 %, which seems to be an underestimate potentially as it does not incorporate the variance in counts across the ROI of the individual frames which are averaged in the process of obtaining the LPS data.

Another method more directly uses Equation 4.1 to find the FCS. The results are shown

in Figure 4.30. Here, the individual values for the film growth rate, atomic flux out the oven nozzle, and the size of the CCD pixels are used instead of the atomic distribution model. All counts over the ROI are averaged and the variance between pixels seems to be the dominating source of uncertainty. This factor of uncertainty across the ROI (22.7 %) combined with the uncertainties of the solid angle (3 %) and photons to count conversion ratio (10 %), yields an uncertainty for the FCS calculation of about 25.0 %. This is summarized in Table 4.16. At this point in time, the background counts have not been subtracted from the measurement used in calculating the FCS via this method. This means that the FCS here is an overestimation.

Table 4.16: Fluorescence Cross Section Measurements

Method	λ_{exc}	**Mean FCS** $\frac{\mathbf{cm^2}}{\mathbf{atom}}$	**St. Dev.**	**Uncertainty**
LPS Subtraction	730.000 nm	1.68E-16	1.7E-17	10.5 %
FCS Calculation	730.000 nm	3.79E-15	9.6E-16	25.0 %

The fluorescence cross sections as calculated via various methods. LPS Subtraction utilizes signal data from the LPS scans on a Rb-doped Kr film with the LPS scans from an empty Kr film deposited under the same conditions subtracted. This leaves data counts solely due to the embedded Rb atoms. The FCS calculation uses individual frames from a laser scan to more manually extract the FCS with ABF atomic flux and film growth parameters. The two measurements differ by about 3.77 standard deviations.

In putting all the information together to get this final number, the transmission through all the lens/filters to the CCD, the CCD count to photon ratio, the CCD exposure time, laser wavelength and power, and a couple of constants were needed. The combined transmission through the 2" lens and the filter that attaches directly to the CCD was calculated to be 91 %.

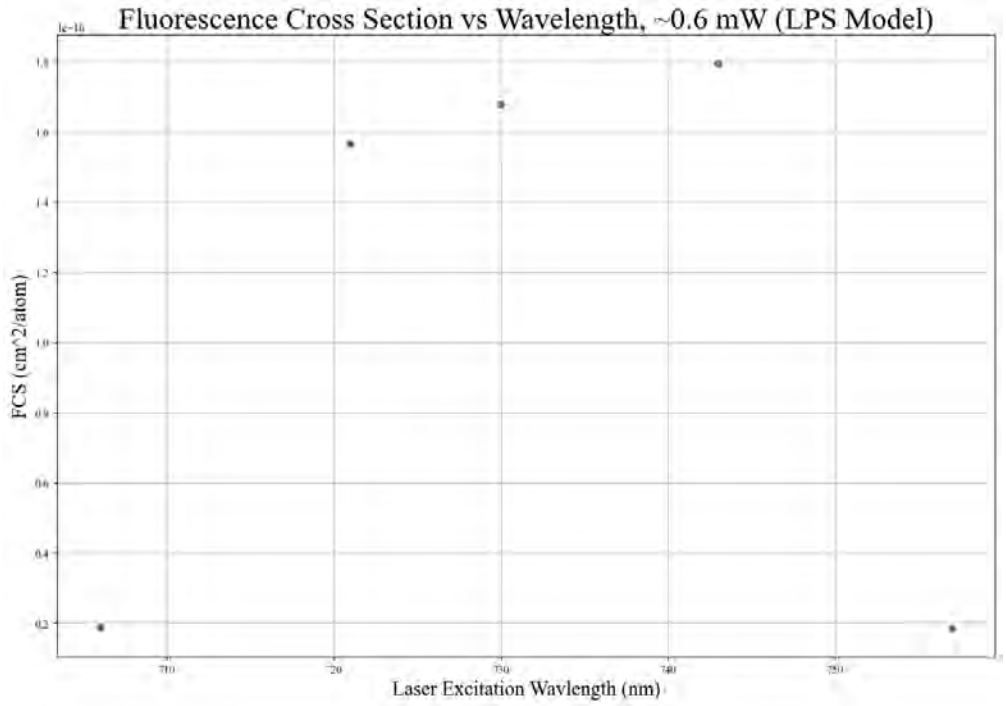

Figure 4.29: This figure shows the results of calculating the FCS using the LPS model. The trend follows the shape of the IMF data as expected.

4.5.2 FCS vs. Wavelength

The FCS should follow the pattern of IMF measurements as they are laser wavelength dependent. This was observed and can be seen in Figures 4.29 and 4.30. Since the LPS method utilized averages over the lines of fit for individual wavelengths there are only five data points. These do appear to match the shape of IMF measurements though. For the FCS calculation method, the data was averaged over the ROI and all data points across the laser wavelength scan were able to be included. However, with this method, background has not been subtracted, which means it is larger than expected. For this reason, the LPS method for determining the FCS value should be regarded as the more accurate reporting.

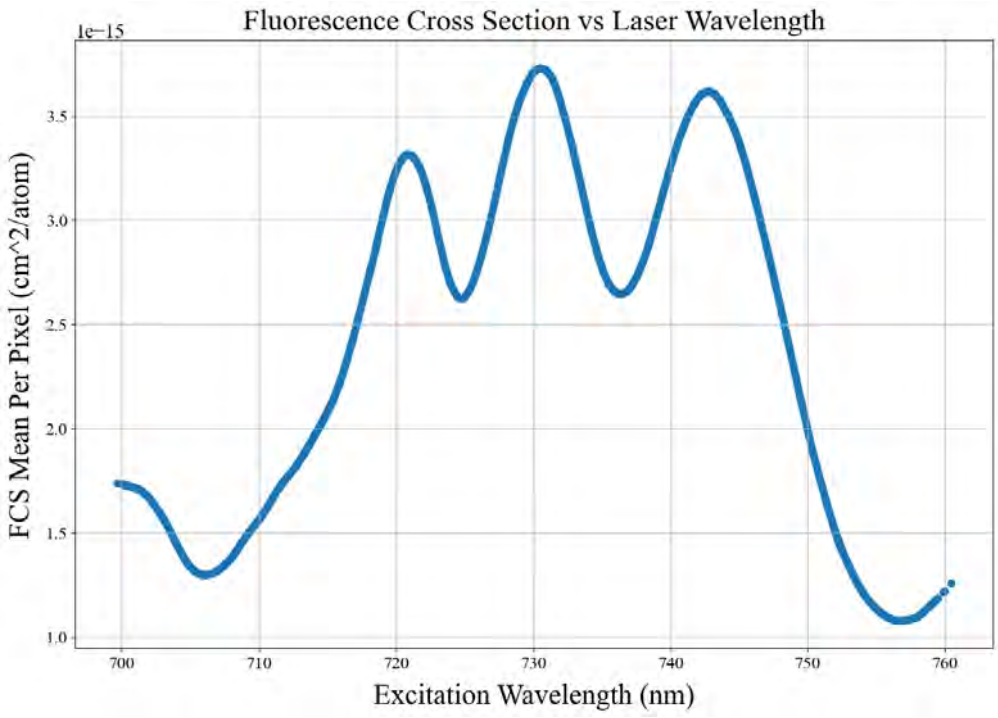

Figure 4.30: This figure shows the results of calculating the FCS using Equation 4.1. The trend follows the shape of the IMF data as expected. Lowess was used to smooth the data. This data does not have background subtracted and is therefore some amount larger.

4.5.3 FCS vs. Temperature

How the IMF counts change over time was investigated. The counts over time test was done to see if the number of counts due to laser induced fluorescence decrease over time during laser exposure. The laser was set to 730 nm at a power of 0.70 mW. The test was lasted about 6.5 hours. The data showed that there is a drop in counts over time of about 7% over about 6.5 hours, which can be seen in Figure 4.31. In the figure, the un-smoothed data points can be seen to show how much they vary.

Film deposition temperature may have an effect on the fluorescence cross section. With only one film to rely on, this parameter will need to be studied in future work.

However, the one film that had successful IMF measurements before the laser broke was studied in a sort of annealing attempt. There is a range of possible deposition temperatures

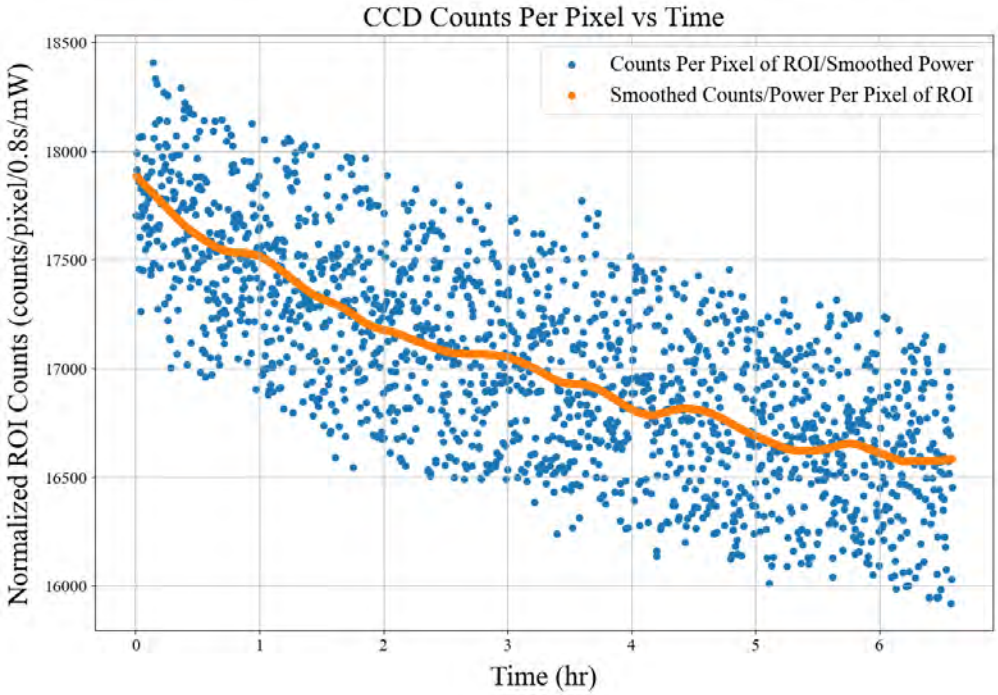

Figure 4.31: Here are the results of monitoring the frame counts over about 6.5 hours. While they do decrease, the decrease is relatively slow with only about 7% decay over this time period.

for film growths, in which there is an ideal temperature for the best film transmission. It follows then that there may be an ideal temperature for the IMF analysis. To see if there was any impact on the IMF measurements as the maintain temperature in pSAM changes, there was an investigation. First, an IMF measurement was taken with the CCD. Then the CCD was used to monitor the counts as the temperature in pSAM was slowly increased. Changing the pSAM temperature must be done slowly so the film is not broken. Figure 4.33 shows that the counts increased very briefly before dropping as the temperature was increased to 28 K. Once at 28 K, another full IMF scan was taken. Then the counts were again monitored as the temperature was slowly ramped back down to 8 K. At that point, one last IMF scan was taken for comparison. All IMF scans at stable temperatures are shown in Figure 4.32.

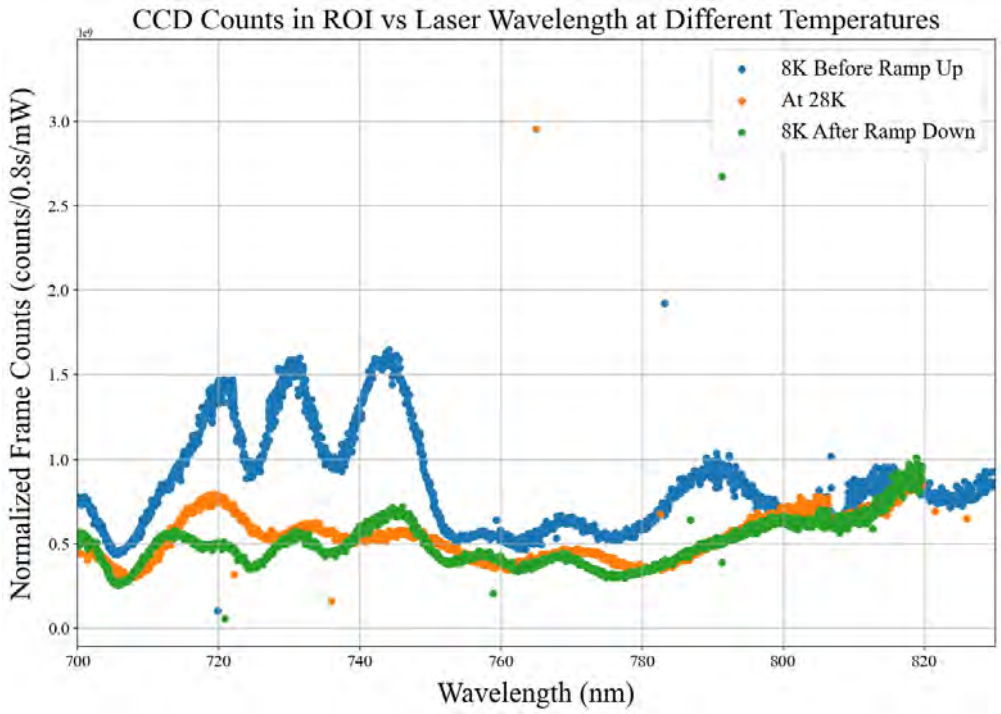

Figure 4.32: This figure shows the IMF scans taken of a Rb-doped Kr film before changing the maintenance temperature in pSAM (8 K), at the height of the temperature increase (28 K), and after returning to the original temperature (8 K) again. These spectra show that the IMF signal deteriorates with increasing the film temperature and does not recover, at least not immediately.

These figures show that the maintenance temperature affects the IMF readings. Increasing the pSAM temperature resulted in a significantly decreased IMF signal. This signal did not return after lowering the temperature back to 8 K. Once again, it seems annealing does not provide promising results here.

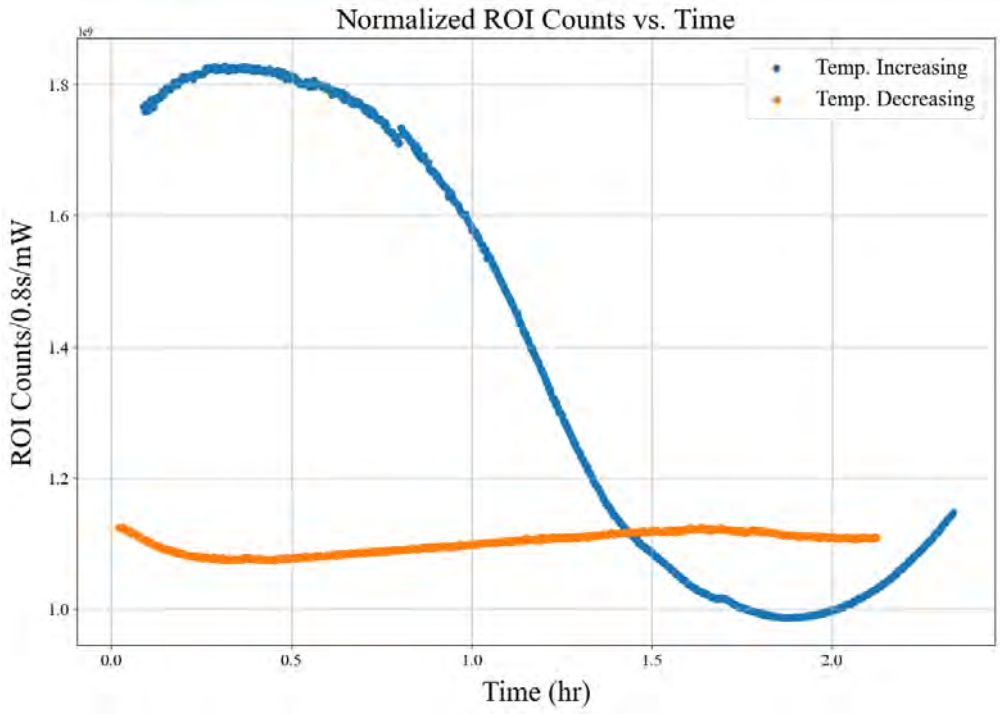

Figure 4.33: This figure shows how the counts from embedded Rb atoms in a Kr film change as the pSAM temperature is altered. As the temperature increases from 8 K to 28 K, the counts mainly decrease. After increasing the temperature, the film was held at 28 K for at least half an hour. Then, the film temperature was slowly decreased and unfortunately, the higher count rate did not return.

4.6 Results & Conclusions

FCS measurements for a Rb-doped Kr film are summarized in Table 4.16. The film was grown on 3/8/2024 and the specifications of it can be found in Table 4.13. Various IMF measurements were taken, summarized in Table 4.14, and they show how the fluorescence of Rb atoms embedded in Kr varies with wavelength, over time, and as film temperature

changes. There were two methods employed to extract the FCS value from the IMF data. The FCS calculated via the LPS method found a value of 1.68E-16 cm^2/atom. This value is in agreement with previously published results [Los20, CWF$^+$19, PDW97]. The uncertainty for this measurement may be an underestimate as it does not incorporate the variance in counts across the ROI of the Rb-doped film. Another method of analysis that more discretely extracts the FCS measurement found a result of 3.79E-15 cm^2/atom. While this uncertainty is more believable, the mean value found is higher than it should be as it did not have the background from laser and environmental contributions subtracted. The count rate of embedded Rb atoms in Kr decays very slowly over time with low power incident laser exposure. Additionally, the count rate decreased dramatically after increasing the temperature of pSAM and the signal was not revived after returning to the lower film temperature.

For a complete understanding of the fluorescence cross section, more data should be collected in which various parameters are adjusted to see how the measurement changes. From current observations, it appears that the fluorescence cross section is mostly uniform across the region of interest. There is a small gradient across the film which appears to be due to either the Kr film itself or due to the real distribution of Rb atoms throughout the film. Based on the spatial CCD images from IMF measurements, the Rb atoms do not appear to have radial symmetry in their distribution as is assumed in the model. With the measured laser distribution fairly even across the substrate, the atomic distribution observed experimentally suggests that their distribution is not centered on the substrate and could be getting blocked by something. Calculations about the geometry of the lens mount posts in the 6-way cross of the ABF setup could determine if the posts are blocking the paths of any atoms to the film. It was shown that these posts did affect the ABF measurement if the nozzle is not perfectly parallel to and centered on the pathway. Investigating this would

help to provide a better model for the atomic distribution and improve accuracy about the number and location of atoms embedded in the film.

Additionally, since only one film was able to successfully have an IMF signal observed before the laser broke, more doped films should be grown to map out the dependencies of the signal on various parameters. These parameters include the film deposition temperature, film growth rate, and film thickness. While it was observed that growing Kr films the standard way, at 34 K until 100 μm thick, do not allow for IMF signal observation, it is unclear what range of thicknesses, deposition temperatures, and growth rates are suitable. This could be important as the films will be used in future work as solid traps to capture reaction products. Most of these product atoms are theorized to stop within the 10 μm of film closest to the substrate, but with only a film of 5 μm thickness being successful for IMF measurements, it is unclear if Rb atoms throughout all of a 10 μm film will emit a readable signal. Furthermore, is the signal affected if there is empty film beyond the initial doped portion should be investigated. Also, is there an ideal temperature for analysis. Increasing the temperature significantly lowered the IMF signal, but decreasing the temperature closer to the base temperature (but still stable) was not tested. It is possible that this could affect the fluorescence of the Rb atoms as well. Different levels of film doping should be explored too. This can be done by adjusting the oven temperature. The temperature used for the doped film deposition that yielded a successful IMF measurement was higher than expected. Therefore, it is unclear if that film growth method would have still yielded positive results if the oven temperature was lower.

There are multiple suggestions that could be implemented that would improve the measurement and analysis of ADF data. The ABF data collection process is well-tuned at this point in time. ABF analysis however, could be improved in terms of accounting for the lens

posts in the 6-way cross as aforementioned. In terms of IMF data collection, the background could be minimized further. Blackout materials similar to the ones employed in ABF could be used in and around pSAM and the CCD camera. Since laser background contributions are still significant, this could potentially and meaningfully improve the signal to background ratio of IMF scans. There are better optical filters that could aid in reducing the background as well. IMF analysis could be improved with better understanding of the photon to count ratio of the CCD camera and a more sophisticated account of the uncertainties. Additionally, more careful considerations for the background could make analysis more efficient. While the model for the solid angle factor is very complete, a more precise measurement between the film and the light-collecting lens could improve its accuracy.

Some suggestions for improvements to the experimental design include adding a blackout material to the interior of pSAM such that there are no notable reflections for which to account and t

Chapter 5. Conclusion & Future Steps

5.1 Personal Contributions to the SAM Project

At the start of my time working with the SAM project, of course I was mainly learning. This was turned into something useful as I was the primary author in a co-write of the film growth procedure. Over time, mentoring other students, I have made many edits in an effort to makes this procedure as mistake-proof as reasonably possible. After assisting with some film growths while learning, I conducted countless film growths on my own and then in a mentor capacity to several undergraduates and junior graduate students. Part of my solo studies consisted of the annealing studies mentioned in the previous chapter. I worked alongside Dr. Loseth to help him with the most recent major modifications to pSAM, as it was developed from version 2.1 to 2.2. This involved operating within the Class-100 cleanroom and using the small crane to open up pSAM for maintenance and alterations to the setup within. Additionally, I supported Dr. Ben Loseth and the SAM project working multiple shifts for the ReA3 experiment in 2019. This involved monitoring and recording data, as well as personally assisting with the data and experiment preparations and the removal of equipment post-experiment.

Once I began my third year as a graduate student, I consistently mentored undergraduates, nearly all of whom presented projects for either the honors college or for the University Undergraduate Research and Arts Forum. I also worked on a comic book with Vivian Breslin that was loosely based on the SAM project and planned for outreach use.

While not currently implemented, I did work to modularize the code for film quality analysis, which if used in the future is more user-friendly as it follows computer science guidelines, is heavily commented, and comes with a tutorial. Furthermore, I developed

multiple LabVIEW VI's to control the setup for both ABF and IMF measurements. These VI's allow for control of all aspects needed for ABF/IMF measurements aside from the laser which must be operated separately. However, these VI's do record measurements of the laser frequency and power.

I wrote code for plotting ABF results, plotting IMF results, calculating the fluorescence cross section, and for modeling the atomic angular distribution out of the nozzle. Due to several typos across the literature, I had to troubleshoot to find the correct equation for the "big, ugly equation" that is the angular distribution of atoms effusing from a nozzle. Additionally I developed this code to be used in the NFC code which determines the number of atoms that will consequently embed in a film and how much of their fluorescence will be measured by the CCD camera given experimental parameters. Part of creating all of these models also required work setting up the software and writing new code for the upgraded CCD camera.

Of course all of this also came with countless hours in the lab, reworking the experimental design for and refining ABF measurements, developing an experimental design for IMF measurements, and myriad experiments made for either setup until total ADF experiments were able to be conducted, at which point, they were. ABF and IMF preparations also included planning for loading the oven. This required extra care for handling Rb as it reacts with oxygen. A procedure was written for this as well. Troubleshooting was also a large part of my graduate career between laser repairs, film growth anomalies, and setting up new equipment.

5.2 Impact of Measured Fluorescence Cross Sections

Both the ABF and IMF measurements show that the peak locations are consistent with published literature [Spe, GSM12]. This gives confidence in the measurements which funnel into the extraction of the FCS. The fluorescence cross section measurements in this thesis can be interpreted by turning to similar experiments to gain context about what might be happening. Given that multiple experiments have detected single atoms/molecules embedded in noble gases with cross sections on the order of 10^{-16} cm^2/atom [CWF$^+$19, PDW97, Los20], the LPS method measurement supports the viability of single atom detection with the SAM technique. The background should be carefully subtracted from the FCS calculation method to determine if its value is in agreement rather than mild tension.

5.3 Future Work

While background for the ABF set of experiments has been greatly minimized, similar efforts could be made for the pSAM/IMF side. Despite a lowered background, undoubtedly in large part due to an improved geometry, there is still room for improvement for reducing the laser light background. While there may be a better filter, it would likely be more impactful to follow an approach similar to adding Aktar black to the interior of the 6-way cross in the ABF setup by adding some to the pSAM instrument. Even a simple black-out box around the optics could help reduce the background.

Without further background minimization, the signal to background ratio currently achieved seems reasonable, at a minimum for the measurement of ^{84}Kr(p, γ)^{85}Rb. Since ^{22}Ne(α, n)^{25}Mg requires greater sensitivity, the signal to background ratio may require fur-

ther maximizing.

Before the SAM project will be ready to take a nuclear cross section measurement, calibration studies will need to be completed. It is recommended to explore how the film growth rate and deposition temperature impact the IMF measurements and subsequent calculation of the FCS. Additionally, investigating if there is an ideal analysis temperature would be beneficial. Calibration of the brightness of atoms embedded in a solid should be repeated for new atomic species/film type combinations. With calibration of embedded atoms better understood, a new analysis to determine the neutralization fraction of ions that are stopped in a noble gas solid trap should be conducted. Once this information is in hand, the SAM project should be prepared to measure a nuclear reaction cross section.

BIBLIOGRAPHY

[BBFH57] E. Margaret Burbidge, G. R. Burbidge, William A. Fowler, and F. Hoyle. Synthesis of the elements in stars. *Rev. Mod. Phys.*, 29:547–650, Oct 1957.

[BCC+22] Caterina Braggio, Roberto Calabrese, Giovanni Carugno, Giuseppe Fiscelli, Marco Guarise, Alen Khanbekyan, Antonio Noto, Roberto Passante, Lucia Rizzuto, Giuseppe Ruoso, and Luca Tomassetti. Spectroscopy of alkali atoms in solid matrices of rare gases: Experimental results and theoretical analysis. *Applied Sciences*, 12(13), 2022.

[BD04] Carlos A. Bertulani and Pawel Danielewicz. *Introduction to Nuclear Reactions*. Graduate Student Series in Physics. Taylor & Francis Group, Boca Raton, FL, 2004.

[BW83] L. C. Balling and J. J. Wright. Laser excitation of excited states of rb and cs atoms in an ar matrix. *The Journal of Chemical Physics*, 78(1):592–593, jan 1983.

[CWF+19] C Chambers, T Walton, D Fairbank, A Craycraft, D R Yahne, J Todd, A Iverson, W Fairbank, A Alamre, J B Albert, G Anton, I J Arnquist, I Badhrees, P S Barbeau, D Beck, V Belov, T Bhatta, F Bourque, J P Brodsky, E Brown, T Brunner, A Burenkov, G F Cao, L Cao, W R Cen, S A Charlebois, M Chiu, B Cleveland, M Coon, M Cote, W Cree, J Dalmasson, T Daniels, L Darroch, S J Daugherty, J Daughhetee, S Delaquis, A Der Mesrobian-Kabakian, R DeVoe, J Dilling, Y Y Ding, M J Dolinski, A Dragone, J Echevers, L Fabris, J Farine, S Feyzbakhsh, R Fontaine, D Fudenberg, G Gallina, G Giacomini, R Gornea, G Gratta, E V Hansen, M Heffner, E W Hoppe, J Hoebl, A House, P Hufschmidt, M Hughes, Y Ito, A Jamil, C Jessiman, M J Jewell, X S Jiang, A Karelin, L J Kaufman, D Kodroff, T Koffas, S Kravitz, R Kruecken, A Kuchenkov, K S Kumar, Y Lan, A Larson, D S Leonard, G Li, S Li, Z Li, C Licciardi, Y H Lin, P Lv, R MacLellan, T Michel, B Mong, D C Moore, K Murray, R J Newby, Z Ning, O Njoya, F Nolet, O Nusair, K Odgers, A Odian, M Oriunno, J L Orrell, G S Ortega, I Ostrovskiy, C T Overman, S Parent, A Piepke, A Pocar, J F Pratte, D Qiu, V Radeka, E Raguzin, T Rao, S Rescia, F Retiere, A Robinson, T Rossignol, P C Rowson, N Roy, R Saldanha, S Sangiorgio, S Schmidt, J Schneider, A Schubert, K Skarpaas, A K Soma, G St-Hilaire, V Stekhanov, T Stiegler, X L Sun, M Tarka, T Tolba, T I Totev, R Tsang, T Tsang, F Vachon, B Veenstra, V Veeraraghavan, G Visser, J L Vuilleumier, M Wagenpfeil, Q Wang, J Watkins, M Weber, W Wei, L J Wen, U Wichoski, G Wrede, S X Wu, W H Wu, Q Xia, L Yang, Y R Yen, O Zeldovich, X Zhang, J Zhao, Y Zhou, T Ziegler, and nEXO Collaboration. Imaging individual barium atoms in solid xenon for barium tagging in nEXO. *Nature*, 569(7755):203 – 207, 2019.

[DDH+91] H. W. Drotleff, A. Denker, J. W. Hammer, H. Knee, S. Küchler, D. Streit, C. Rolfs, and H. P. Trautvetter. New22ne(α,n)25mg-resonances at very low energies relevant for the astrophysical s-process. *Zeitschrift für Physik A Hadrons and Nuclei*, 338(3):367–368, Sep 1991.

[DLW21] Ugne Dargyte, David M. Lancaster, and Jonathan D. Weinstein. Optical and spin-coherence properties of rubidium atoms trapped in solid neon. *Phys. Rev. A*, 104:032611, Sep 2021.

[FW22] Steven Fromm and Erin White. A more comprehensive treatment of the 225ra oven: Modeling the angular distribution from a narrow cylindrical channel in multiple flow regimes. Technical Report Draft v2.0, Facility for Rare Isotope Beams, Michigan State University, East Lansing, MI, April 2022.

[Goo78] Alvin M. Goodman. Optical interference method for the approximate determination of refractive index and thickness of a transparent layer. *Applied Optics*, 17(17):2779–2787, sep 1978.

[GSM12] Ilja Gerhardt, Kyungseob Sin, and Takamasa Momose. Excitation and emission spectra of rubidium in rare-gas thin-films. *The Journal of Chemical Physics*, 137(1):014507 – 7, 07 2012.

[HB73] F. X. Haas and J. K. Bair. Total neutron yield from the (α, n) reaction on ^{21,22}Ne. *Phys. Rev. C*, 7:2432–2436, Jun 1973.

[Ili15] Christian Iliadis. *Nuclear Physics of Stars, Second, Revised and Enlarged Edition*. Wiley-VCH, Weinheim, Germany, 2015.

[JKM+01] M. Jaeger, R. Kunz, A. Mayer, J. W. Hammer, G. Staudt, K. L. Kratz, and B. Pfeiffer. $^{22}ne(\alpha, n)^{25}mg$: The key neutron source in massive stars. *Phys. Rev. Lett.*, 87:202501, Oct 2001.

[JRR18] Jr. John R. Rumble, editor. *CRC Handbook of Chemistry and Physics*. CRC press, Boca Raton, FL, 99th (internet version) edition, 2018.

[LDUW21] David M. Lancaster, Ugne Dargyte, Sunil Upadhyay, and Jonathan D. Weinstein. Radiative properties of rubidium atoms trapped in solid neon and parahydrogen. *Phys. Rev. A*, 103:052614, May 2021.

[LDW24] David M. Lancaster, Ugne Dargyte, and Jonathan D. Weinstein. Optical spin readout of single rubidium atoms trapped in solid neon. *Phys. Rev. Res.*, 6:L012048, Mar 2024.

[LFF+19] B Loseth, R Fang, D Frisbie, K Parzuchowski, C Ugalde, J Wenzl, and J T Singh. Detection of atomic nuclear reaction products via optical imaging. *Phys. Rev. C*, 99(6):065805, 06 2019.

[LGW+21] G. Lotay, S. A. Gillespie, M. Williams, T. Rauscher, M. Alcorta, A. M. Amthor, C. A. Andreoiu, D. Baal, G. C. Ball, S. S. Bhattacharjee, H. Behnamian, V. Bildstein, C. Burbadge, W. N. Catford, D. T. Doherty, N. E. Esker, F. H. Garcia, A. B. Garnsworthy, G. Hackman, S. Hallam, K. A. Hudson, S. Jazrawi, E. Kasanda, A. R. L. Kennington, Y. H. Kim, A. Lennarz, R. S. Lubna, C. R. Natzke, N. Nishimura, B. Olaizola, C. Paxman, A. Psaltis, C. E. Svensson, J. Williams, B. Wallis, D. Yates, D. Walter, and B. Davids. First direct measurement of an astrophysical p-process reaction cross section using a radioactive ion beam. *Phys. Rev. Lett.*, 127:112701, Sep 2021.

[Los20] Benjamin Thomas Loseth. *Development of a Single-Atom Microscope for Optical Detection of Atomic Nuclear Reaction Products*. PhD thesis, Michigan State University, 2020.

[LXP+21] R. Lambo, C.-Y. Xu, S. T. Pratt, H. Xu, J. C. Zappala, K. G. Bailey, Z.-T. Lu, P. Mueller, T. P. O'Connor, B. B. Kamorzin, D. S. Bezrukov, Y.-Q. Xie, A. A. Buchachenko, and J. T. Singh. High-resolution spectroscopy of neutral yb atoms in a solid ne matrix. *Phys. Rev. A*, 104:062809, Dec 2021.

[Noo21] Joseph Noonan. Model for the transmission ratio of krypton films. Technical report, Spinlab Research Group at the National Superconducting Cyclotron Laboratory, 2021. Internal technical note.

[OK70] Donald R. Olander and Valerie Kruger. Molecular beam sources fabricated from multichannel arrays. iii. the exit density problem. *Journal of Applied Physics*, 41(7):2769–2776, 06 1970.

[Pal20] Alicia R. Palmisano. *Constraining the P Process: Cross Section Measurement of $^{Kr}(p,\gamma)^{85}Rb$*. PhD thesis, Michigan State University, 2020.

[PDW97] Taras Plakhotnik, Elizabeth A. Donley, and Urs P. Wild. Single-molecule spectroscopy. *Annual Review of Physical Chemistry*, 48(1):181–212, 1997. PMID: 15012444.

[PKSD+22] A. Palmisano-Kyle, A. Spyrou, P. A. DeYoung, A. Dombos, P. Gastis, O. Olivas-Gomez, C. Harris, S. Liddick, S. M. Lyons, J. Pereira, A. L. Richard, A. Simon, M. K. Smith, A. Tsantiri, and R. Zegers. Constraining the astrophysical p process: Cross section measurement of the $^{84}\mathrm{Kr}(p,\gamma)^{85}\mathrm{Rb}$ reaction in inverse kinematics. *Phys. Rev. C*, 105:065804, Jun 2022.

[Rau] Dr. Thomas Rauscher. Non-smoker, https://nucastro.org/nonsmoker.html. https://nucastro.org/nonsmoker.html.

[RDD+13] T Rauscher, N Dauphas, I Dillmann, C Frhlich, Zs Flp, and Gy Gyrky. Constraining the astrophysical origin of the p-nuclei through nuclear physics and meteoritic data. *Reports on Progress in Physics*, 76(6):066201, may 2013.

[RG] R. Reifarth and K. Göbel. p-process fluxes. https://exp-astro.de/fluxes/.

[RNH+16] T. Rauscher, N. Nishimura, R. Hirschi, G. Cescutti, A. St. J. Murphy, and A. Heger. Uncertainties in the production of p nuclei in massive stars obtained from Monte Carlo variations. *Monthly Notices of the Royal Astronomical Society*, 463(4):4153–4166, 09 2016.

[Sin23] Jaideep Singh. An introduction to absolute measurements of atomic number densities, oscillator strengths, fluorescence yields, and atomic energy levels using light scattering experiments. Technical Report INT-PUB-17-033 Version 2.0, Facility for Rare Isotope Beams, Michigan State University, East Lansing, MI, October 2023.

[SK74] Wilfried Schulze and Dieter M. Kolb. Density and refractive index of solid layers of noble gases and sulphur hexafluoride. *Journal of the Chemical Society, Faraday Transactions 2: Molecular and Chemical Physics*, 70(0):1098–1105, jan 1974.

[SMG+98] Giacinto Scoles, D.R Miller, W. Gentry, H Pauly, Davide Bassi, U. Hefter, K. Bergman, Mario Zen, J. Reuss, C.J.N. Meijdenberg, D. Abuerbach, M. Kappes, Samuel Leutwyler, Ugo Valbusa, U. Buck, Y.T. Lee, Paul Dagdigian, Steven Stolte, R. Dren, and Salvatore Iannotta. *Atomic and Molecular Beam Methods: Vol. 1.* 1998.

[Spe] David Speck. *Rubidium 85 D Line Data & Rubidium 87 D Line Data, available online at http://steck.us/alkalidata.*

[STS+15] Philip A. Schulz, Joseph A. Tan, Peter W. Snyder, Brian M. Wong, and David Patterson. Laser ablation doping of superfluid helium droplets: Enhanced efficiency and characterization via monomer isolation spectroscopy. *The Journal of Chemical Physics*, 143(4):044316, 2015.

[WdG23] M. Wiescher, R. J. deBoer, and J. Grres. The resonances in the ^{22}ne+α fusion reactions. *The European Physical Journal A*, 59(1), Jan 2023.

[WKL12] M. Wiescher, F. Kppeler, and K. Langanke. Critical reactions in contemporary nuclear astrophysics. *Annual Review of Astronomy and Astrophysics*, 50(1):165–210, 2012.

[ZZB10] James F. Ziegler, M. D. Ziegler, and J. P. Biersack. Srim the stopping and range of ions in matter (2010). *Nuclear Instruments and Methods in Physics Research Section B: Beam Interactions with Materials and Atoms*, 268(1112):1818–1823, jun 2010.

APPENDIX A. Appendix Plans

The current list of items planned to add in the appendix section (which will be done between you reading this now and ProQuest submission) include the following:

- A summary table of all samples grown - A list of all codes and their locations - The film growth procedure - The oven loading procedure